

**The Henryk Niewodniczański Institute of Nuclear Physics**

**Polish Academy of Sciences**

**Cyclotron Centre Bronowice**

---

**Doctoral dissertation**

**Optimization of proton pencil beam scanning  
technique for moving targets**

**KATARZYNA CZERSKA**

**SUPERVISOR:**

**ASSOC. PROF. RENATA KOPEĆ, PhD (IFJ PAN)**



---

**Kraków, 2022**



---

**European Union**  
European Social Fund



**European  
Funds**  
Knowledge Education Development

**This PhD thesis has been completed in the framework of the Program POWER,  
project No. POWR.03.02.00-00-I004/16, co-financed by the European Union**

---



## **Podziękowania**

*Chciałabym serdecznie podziękować wszystkim osobom, bez zaangażowania których nie byłoby możliwe przygotowanie oraz ukończenie poniższej rozprawy doktorskiej.*

*Szczególne podziękowania kieruję do:*

*Prof. Renaty Kopeć za pomoc w przygotowaniu tej rozprawy, wsparcie merytoryczne oraz życzliwość,*

*Kierownictwu oraz Koleżankom i Kolegom z Centrum Radioterapii i Usprawniania NU-MED w Elblągu, bez pomocy których duża część tej pracy nie byłaby możliwa do wykonania,*

*Wszystkim pracownikom Centrum Cyklotronowego Bronowice, a przede wszystkim Pracowni Dozymetrii i Kontroli Jakości. Dziękuję Dawidowi Krzempkowi za merytoryczne wsparcie oraz udostępnienie programów AnalyseSpot i AnalyseField, a także Robertowi Kosowi za możliwość wykorzystania programu TPS\_Histogram\_Analyzer,*

*oraz nieustannie wspierającej mnie Rodzinie.*



## **Abstract**

Proton pencil beam scanning radiotherapy, a precise and unique radiotherapy modality, has been dynamically developed worldwide over recent years. It is worth emphasizing that, also in Poland, this sophisticated technology has been evolving since the first treatments of deep situated tumors at Cyclotron Centre Bronowice (CCB) IFJ PAN in 2016. This dissertation is dedicated specifically to the proton radiotherapy of the so-called moving targets, whose position might change over treatment, making it one of the most complex topics in the radiotherapy world. Nevertheless, despite many technical challenges and difficulties, the treatments of indications such as, e.g., breast or lung cancer, have been clinically implemented in many facilities worldwide due to the significant dosimetric gain available to achieve with proton beams. However, the clinical implementation of treatment procedures has to be preceded by a thorough analysis of potential benefits, verification of the system's abilities and suitability to be used in specific cases. Therefore, the work presented in this dissertation might be an initial basis for creating future treatment protocols for moving target treatments at CCB IFJ PAN in Krakow, Poland.

In order to estimate the validity of using proton beams in breast cancer treatments, a comparative and retrospective study with the commonly used photon modality and the effectiveness of using breath hold technique in combination with protons had been conducted. The planning study followed the implementation of a dedicated CT calibration curve at CCB IFJ PAN for the scanner used in data collection. The results showed that proton radiotherapy might enable further and significant reduction of the unwanted dose to critical organs, such as, e.g. heart or left anterior descending artery, thus decreasing the risk of possible late toxicity effects. Moreover, a study optimizing and verifying the significance of beam angle selection in proton radiotherapy of breast cancer was also conducted, to create a basis for future treatment protocols. The study used five beam arrangements, applied in free and breath hold anatomies. It verified their impact and each beam's selection vulnerability on resulting plan quality and robustness. Several activities were undertaken to verify the possibilities of conducting lung cancer treatments with proton beams at CCB IFJ PAN. Available in

the facility, radiotherapy tools, such as, e.g. CIRS Dynamic Thorax Phantom, CIRS Dynamic Platform or VisionRT system, were employed in the study. The presented works were divided into 4D imaging, treatment planning and dosimetry of lung cancer, simulated by a breathing phantom. Two optimization algorithms of the Varian Eclipse Treatment Planning System (TPS) were used to assess each algorithm's dosimetric differences and effectiveness in lung cancer treatment planning (Varian Medical Systems, Palo Alto, California). Moreover, the implementation and validation of the so-called repainting modality, used to minimize the *interplay effect* during scanned beam delivery, was also conducted, and obtained results showed high beam parameters reproducibility. Measurements performed at the gantry room, with a dedicated detector and dynamic platform, enabled to assess the impact of *interplay effect* on a treatment plan quality and verified the ability of repainted delivery on the dose distributions improvement in two selected motion scenarios.

## Streszczenie

Radioterapia protonowa, jedna z najbardziej precyzyjnych i unikatowych form radioterapii, jest jednocześnie jedną z najbardziej dynamicznie rozwijających się technik na przestrzeni ostatnich lat, również w Polsce. Poniższa praca doktorska jest dedykowana wyłącznie radioterapii protonowej tzw. poruszających się narządów, których położenie może się zmieniać w czasie seansu terapeutycznego, co czyni ją jedną z najbardziej złożonych zagadnień w radioterapii w ogólności. Dzięki znacznemu zyskowi terapeutycznemu, obserwowanemu przy wykorzystaniu wiązek protonowych oraz pomimo wielu technicznych wyzwań, leczenie wskazań takich jak, np. rak piersi lub rak płuca, zostało klinicznie zaimplementowane w wielu ośrodkach na całym świecie. Implementację musi jednak poprzedzać szczegółowa i dogłębna analiza zysków, weryfikacja możliwości danego systemu oraz zasadność użycia techniki w konkretnych przypadkach. Zaprezentowane w poniższej rozprawie badania mogą stanowić podstawę dla przyszłych protokołów klinicznych wykorzystywanych w leczeniu poruszających się narządów w Centrum Cyklotronowym Bronowice (CCB) IFJ PAN w Krakowie.

W celu oszacowania zasadności wykorzystania wiązki protonowej w leczeniu raka piersi przeprowadzone zostało retrospektywne porównanie z powszechnie dostępną techniką fotonową, a także efektywność dodatkowego wykorzystania tzw. techniki wstrzymanego oddechu w radioterapii protonowej. Rozpoczęcie tego etapu zostało poprzedzone pomiarem oraz wprowadzeniem w CCB IFJ PAN nowej krzywej kalibracji tomografu komputerowego użytego do zebrania danych obrazowych. Wyniki wskazują, iż radioterapia protonowa umożliwia znaczną minimalizację dawek na narządy krytyczne, w tym serce i lewą tętnicę wieńcową zstępującą, co w przyszłości może się przekładać na mniejsze ryzyko wystąpienia późnych powikłań. Ponadto, wykonana optymalizacja oraz weryfikacja wpływu różnych układów wiązek w radioterapii protonowej raka piersi, zarówno dla tomografii wykonanych na swobodnym, jak i wstrzymanym oddechu, pozwoliła na oszacowanie ich wpływu na jakość planu terapeutycznego. Dostępne w CCB IFJ PAN narzędzia wspomagające, m.in. obrazowanie, czy dozymetrię, tj. fantom oddechowy CIRS Dynamic Thorax Phantom,

platforma oddechowa CIRS Dynamic Platform, czy system bramkowania oddechowego VisionRT, zostały wykorzystane w celu oszacowania możliwości ośrodka CCB IFJ PAN pod kątem leczenia raka płuca. Prezentowane prace obejmowały wykonanie tomografii 4D, planowanie oraz testy dozymetryczne na stanowisku gantry. Dwa algorytmy do optymalizacji dawki, dostępne w systemie planowania leczenia Varian Eclipse, zostały zweryfikowane pod kątem możliwości ich użycia w tym konkretnym przypadku (Varian Medical Systems, Palo Alto, California). Ponadto, wprowadzono i zwalidowano tzw. technikę repaintingu, tj. wielokrotnego przemieszczania warstw energetycznych planu terapii oraz oszacowano wpływ efektu *interplay*, wynikającego z nałożenia się struktur czasowych ruchu guza oraz wiązki protonowej, na zaplanowany rozkład dawki podczas testów dozymetrycznych dla dwóch krzywych oddechowych z wykorzystaniem fantomu oddechowego.

## **Contents**

<b>1. Introduction</b>	<b>15</b>
<b>2. Aim and outline</b>	<b>23</b>
<b>3. Radiation therapy</b>	<b>27</b>
<b>4. The physics of radiation therapy</b>	<b>31</b>
a. Physical interactions of photons with matter	31
b. Physical interactions of protons with matter	33
i. Stopping theory	33
ii. Scattering theory	36
iii. Nuclear interactions	38
<b>5. The clinical aspects of moving targets radiotherapy</b>	<b>39</b>
a. Patient selection	40
b. Motion monitoring and mitigation approaches	42
c. 4D imaging and contouring	45
d. 4D treatment planning	48
i. Significance of beam angles selection	48
ii. Proton pencil beam scanning algorithms	49
iii. 3D and 4D robust optimization	49
e. Clinical challenges of moving target treatments - breast cancer and lung cancer cases	51
<b>6. Study I: The definition and implementation of a new CT calibration curve</b>	<b>57</b>
a. Introduction	57
b. Materials and methods	58
c. Results	61
<b>7. Study II: Proton vs photon radiotherapy of left-sided breast cancer</b>	<b>65</b>
a. Introduction	65
b. Materials and methods	66
c. Results	69
<b>8. Study III: Significance of beam angle selection in proton radiotherapy of left-sided breast cancer</b>	<b>77</b>
a. Introduction	77
b. Materials and methods	80
c. Results	82

<b>9. Study IV: Proton radiotherapy of lung cancer</b>	<b>93</b>
a. Introduction	93
b. 4D imaging, treatment planning and robust 4D optimization	94
i. Materials and methods	94
ii. Results	100
c. Implementation and validation of rescanning modality	104
i. Materials and methods	104
ii. Results	110
d. Equipment and preparations for dosimetry testing	115
i. Materials and methods	115
ii. Results	119
<b>10. Conclusions</b>	<b>129</b>
<b>Bibliography</b>	<b>133</b>
<b>List of Tables</b>	<b>143</b>
<b>List of Figures</b>	<b>145</b>

## List of Abbreviations

3D - three dimensional	LAD - Left Anterior Descending Artery
3D-CRT - 3 Dimensional Conformal Radiation Therapy	LDR - Low-Dose Rate
3DRO - Robust 3D Optimization	MCS - Multiple Coulomb Scattering
4DCT - 4 Dimensional CT	MDR - Medium-dose Rate
4DRO - Robust 4D Optimization	MIP - Maximum Intensity Projection
BJR - The British Journal of Radiology	MidV - Mid-ventilation
BMS - Beam Management System	MU - Monitor Unit
CCB - Cyclotron Centre Bronowice	NHFT - Nasal High Flow Therapy
CCD - Charge-coupled Device	NSCLC - Non-small Cell Lung Cancer
CSDA - Continuous Slowing Down Approximation	NTCP - Normal Tissue Complication Probability
CT - Computed Tomography	NUPO - Nonlinear Universal Proton Optimizer
CTV - Clinical Target Volume	OAR - Organ At Risk
DD - Dose Difference	PBS - Pencil Beam Scanning
DIBH - Deep Inspiration Breath Hold	PCS - Proton Convolution Superposition
DID - Digital Imaging Devices	PET - Positron Emission Tomography
DDC - Dose Deposition Coefficients	PPS - Patient Positioning System
DICOM - Digital Imaging and Communications in Medicine	PPVS - Patient Positioning and Verification System
DTA - Distance To Agreement	PSPT - Passively Scattered Proton Therapy
DVH - Dose-Volume Histogram	PTCOG - Particle Therapy Co-Operative Group
EBCTCG - Early Breast Cancer Trialists' Collaborative Group	QUANTEC - Quantitative Analysis of Normal Tissue Effects in the Clinic
FRS - Fixed Reference System	RBE - Relative Biological Effectiveness
GCO - Global Cancer Observatory	RCT - Randomized Controlled Trials
GCS - Gantry Coordinate System	RS - Range Shifter
GTV - Gross Tumor Volume	RSNPL - Range and Stopping Power for Nuclear Physics Laboratory
HDR - High-Dose Rate	RSP - Relative Stopping Power
HU - Hounsfield Unit	RT - Radiation Therapy
IARC - International Agency for Research on Cancer	RTD - Real Time Delta
ICRU - International Commission on Radiation Units and Measurements	RTOG - Radiation Therapy Oncology Group
ICTV - Internal Clinical Target Volume	SBRT - Stereotactic Body Radiation Therapy
IFJ PAN - Institute of Nuclear Physics Polish Academy of Sciences	SFUD - Single Field Uniform Dose
IGPT - Image Guided Proton Therapy	SMPS - Scanning Magnet Power Supply
IMPT - Intensity Modulated Proton Therapy	TCS - Therapy Control System
IMRT - Intensity Modulated Radiation Therapy	TPS - Treatment Planning System
ITV - Internal Target Volume	VMAT - Volumetric Modulated Arc Therapy
KRN - Krajowy Rejestr Nowotworów	WET - Water Equivalent Thickness
LA-NSCLC - Locally-advanced Non-small Cell Lung Cancer	WHO - World Health Organization



## 1. Introduction

The Cyclotron Centre Bronowice (CCB), a part of the Institute of Nuclear Physics Polish Academy of Sciences (IFJ PAN) in Krakow, Poland, is a unique facility that combines the clinical operation with research tasks. It is the first, and currently the only, proton radiotherapy center in Poland. It has been in clinical operation since 2016, offering both ocular melanoma treatments and proton therapy to other, deep situated tumors located within the whole body. The CCB IFJ PAN is equipped with the IBA therapy system Proteus 235 based on an isochronous cyclotron C-230 (Ion Beam Applications, Belgium) accelerating protons up to 230 MeV energy (Figure 1). The beam is shared by four rooms, i.e. an experimental hall, an eye treatment room and two gantries (Figure 2).

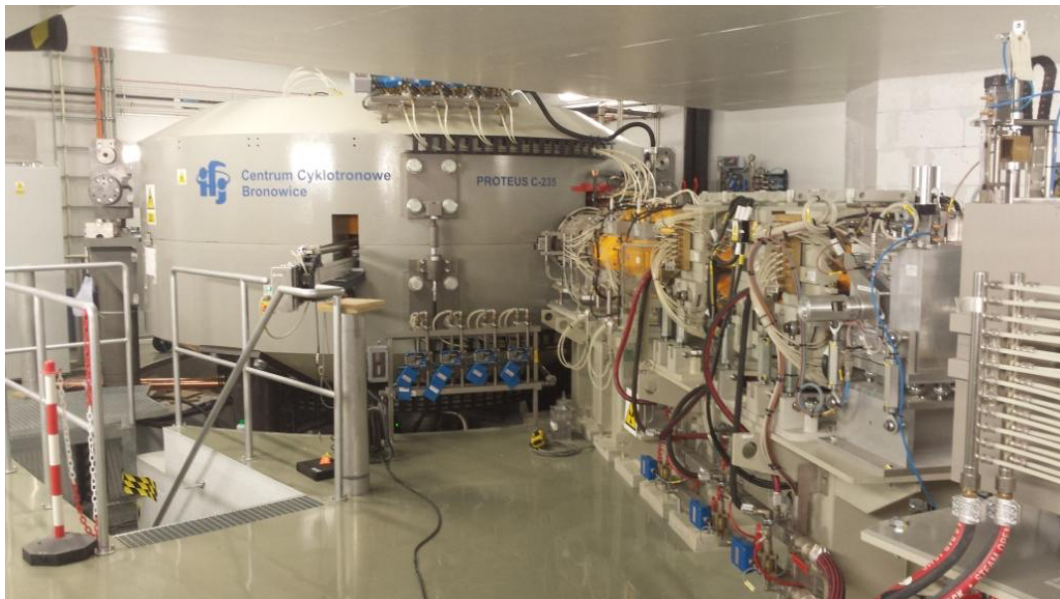


**Figure 1** IBA C-230 cyclotron at CCB (IFJ PAN) in Krakow, Poland  
([https://ccb.ifj.edu.pl/pl.cyklotron\\_proteus\\_c\\_235.html](https://ccb.ifj.edu.pl/pl.cyklotron_proteus_c_235.html))

The gantry treatment rooms are equipped with a dedicated IBA scanning nozzle, enabling a pencil beam scanning (PBS) delivery technique, which is one of the most advanced and precise proton beam delivery technologies. The clinically available

energies vary between 70 MeV and 226 MeV, corresponding to the range in water of 40 mm to 300 mm and beam spot sizes ( $\sigma_{x,y}$ ) between 6.4 mm and 2.3 mm for 70 MeV and 225 MeV, respectively. For tumors, which are placed more superficially, a movable range shifter (drawer) can be inserted in the beam's path for further energy decrease and thus range reduction. In addition, the gantry construction allows for 360° rotation and the maximum scanning area is 30x40 cm<sup>2</sup>. Both features vastly expand the possible geometrical treatment options.

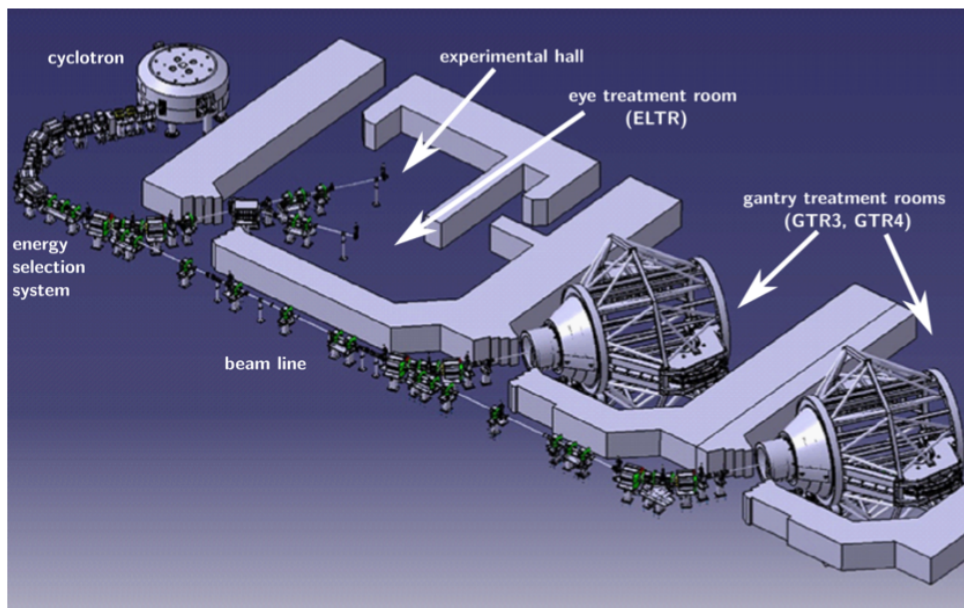


**Figure 2** Schematic outline of the CCB IFJ PAN facility: the IBA Proteus 235 therapy system consisting of a cyclotron with highlighted energy selection system and beam line shared by four rooms: experimental hall, eye treatment room and two gantry rooms with dedicated pencil beam scanning nozzles (reproduced from Kłodowska, 2018)

The active pencil beam scanning system used at CCB is the most advanced proton delivery technology nowadays. The principle of beam scanning uses the main features of protons, i.e. their electrical charge and the possibility of being magnetically deflected. Therefore, proton beams can be used as narrow, monoenergetic pencil beams, scanned spot by spot over the whole 3D target volume (Figure 3). The scanning process starts with the deepest layer of the highest energy. It performs the irradiation of the 2D  $X$ - $Y$  plane, perpendicular to the beam direction, thanks to the two scanning magnets ( $X_g$ ,  $Y_g$ ) located in the nozzle and deflecting the beam to the planned position in the tumor (Figure 4). Subsequently, the energy is reduced and the system moves to paint the next

perpendicular 2D  $X$ - $Y$  plane. This process continues until the whole 3D target volume is covered with proton PBS spots and until the planned dose distribution is delivered (Schlegel et al., 2006).

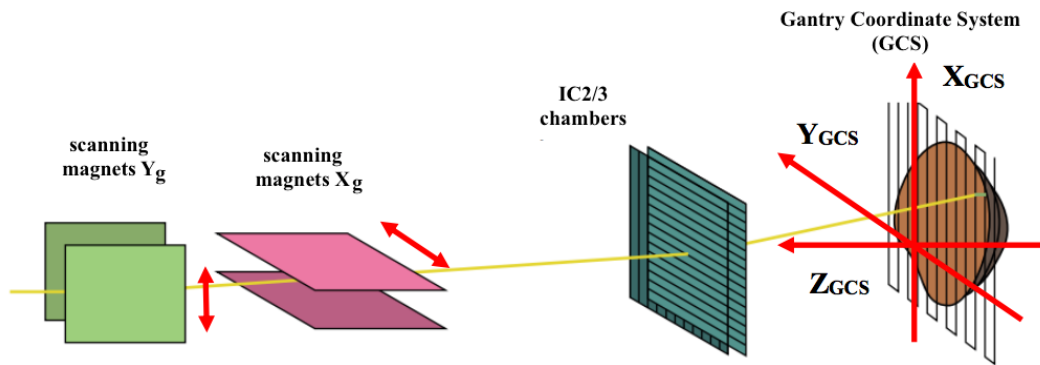


**Figure 3** The principle of PBS technique: two scanning magnets located in the nozzle ( $X_g$  - horizontal and  $Y_g$  - vertical) deflect the narrow proton pencil beam to irradiate the predefined spot positions over the 3D tumor volume (reproduced from Mojżeszek, 2018)

The ability to modulate the beam intensity, together with scanned delivery, is the basis of the intensity modulated proton therapy (IMPT), which can be characterized by the highest target conformity and possible high dose escalation within the tumor region. The IMPT plans contain fields of non-homogeneous dose distribution, which superposition results in homogenous target dose coverage. Nevertheless, the scanning technique also determines many aspects necessary to be controlled and fulfilled longitudinally, transversely and dosimetrically concerning the planned dose distribution, i.e. varying beam energy, lateral spot position by magnetic scanning and the amount of dose. The dose distribution is predefined in the optimization and calculation processes in the Treatment Planning System (TPS). Currently, the Varian Eclipse TPS version 16.1 (Varian Medical Systems, Palo Alto, California) is used at CCB IFJ PAN.

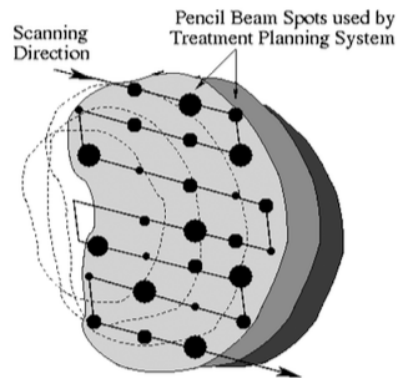


**Figure 4** A schematic drawing of a scanning technique: pencil beam is scanned across the 3D target volume, i.e. layer by layer and spot by spot, starting from the 2D X-Y plane of highest energy. Different spots, represented as black circles, depicts various spots intensity (a principle of intensity modulated proton therapy, IMPT) (Trofimov & Bortfeld, 2003)

Due to the extremely high precision and nature of the proton radiotherapy, the beam delivery process and the immobilization of patients have to be done with submillimeter accuracy. IBA Verisuite software is a patient positioning system that enables calculation, based on the computed tomography datasets and orthogonal X-ray images taken at the gantry room, the alignment corrections to ensure high reproducibility of patients immobilization over the course of treatment (Figure 5). The Therapy Control System (TCS) provides the connection between the Verisuite program and the Patient Positioning System (PPS). The PPS is a robotic arm, commonly called a treatment couch, with six degrees of freedom (three translations, i.e.  $x$ ,  $y$ ,  $x$  and three rotations, i.e. *pitch*, *roll* and couch *rotation*). A whole set of vertical and horizontal lasers is used to initially position the patients on the treatment couch. Then, with regard to patient anatomy and treatment plan, X-ray imaging is conducted to compare the actual position with the anatomy acquired during the CT scan for treatment planning purposes. Both gantry treatment rooms are equipped with X-ray tubes and flat panels, i.e. Digital Imaging Devices (DID), which allow recording of the image.

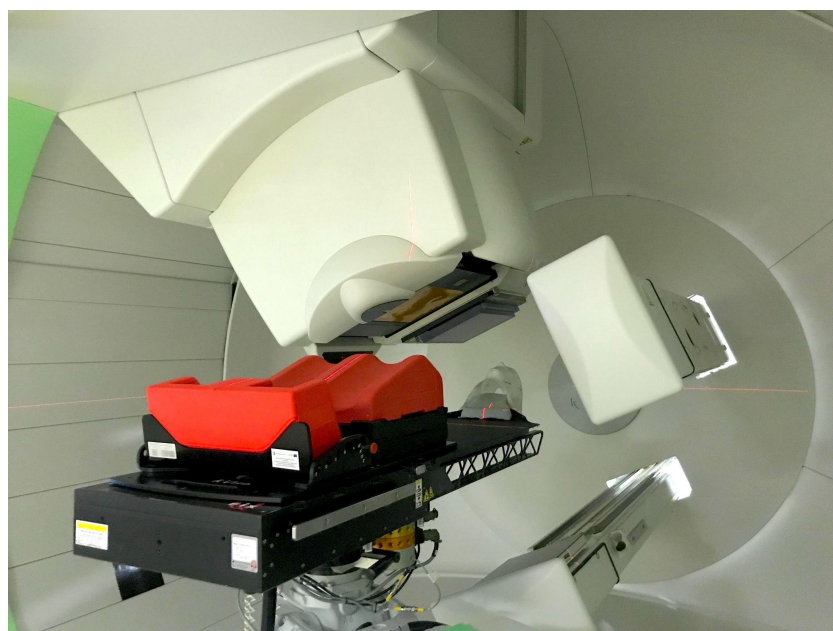


**Figure 5** The Patient Positioning and Verification System (PPVS) at CCB IFJ PAN includes two orthogonal X-ray tubes (one located in the nozzle and one located in the rolling floor) and two flat panels (retracted at the image) to record the X-ray image

An additional system, available at CCB IFJ PAN, which supports the positioning and imaging of patients, is the optical system VisionRT (VisionRT Ltd, United Kingdom). Both gantry treatment rooms and the computed tomography (CT) are equipped with HD camera units, which can derive patients' respiratory signal based on the video of three dimensional (3D) speckle pattern projected onto the patient (Figure 6). The fact that the system is non-invasive and does not use ionizing radiation to perform surface imaging and the online operating mode are the main and significant advantages. There are three VisionRT products installed in CCB, i.e. AlignRT, GateCT or GateRT, using either one or three camera units to track patients' surfaces and movements (VisionRT Product Guide, 2015). The GateCT application uses one, centrally positioned towards the CT, 3D camera and allows the acquisition of gated or non-gated imaging data based on the chosen protocols and thresholds. There are two variables necessary to be defined before imaging, i.e. monitoring and tracking points. The monitoring point should be chosen within an area of relatively stable anatomy and give a signal independent of breathing motion, e.g. shoulder. The tracking point should be placed within an area visibly affected by motion, such as ribs or chest wall (GateCT

User Guide, 2015). At that stage, the reference surface is also captured, a base for further positioning and/or gated treatments at the gantry rooms with either AlignRT or GateRT applications. Subsequently, the GateCT allows for the CT dataset reconstruction to certain breathing phases based on the recorded breathing pattern thus creating, e.g. 4DCT.

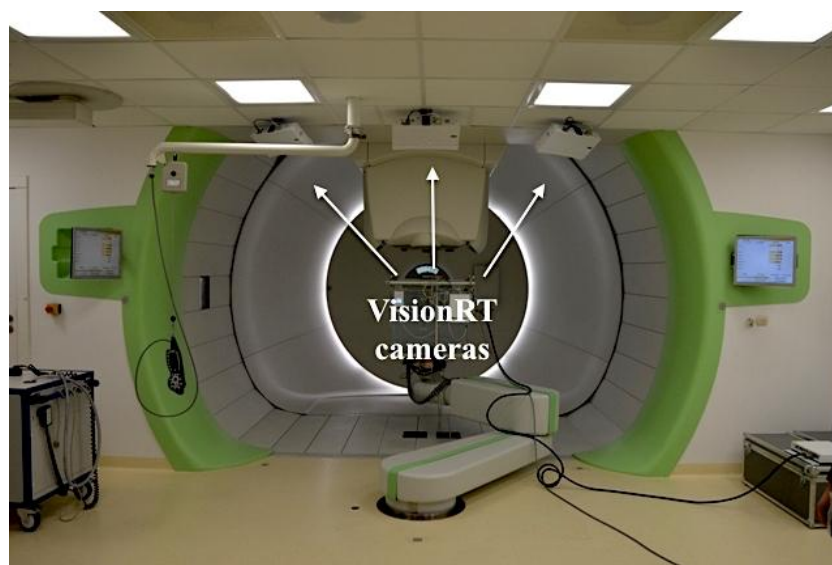


**Figure 6** VisionRT system 3D cameras mounted in the gantry treatment room at CCB IFJ PAN ([https://ccb.ifj.edu.pl/pl.dwa\\_nowoczesne\\_stanowiska\\_gantry.html](https://ccb.ifj.edu.pl/pl.dwa_nowoczesne_stanowiska_gantry.html))

The AlignRT product uses three cameras. Its main aim is to capture the patient's actual surface and compare it with the reference acquired during the prepared for treatment planning CT scan. The online calculations of real-time deltas (RTDs) between reference and actual surface give immediate feedback regarding the patient's position. The system tracks changes in six degrees of freedom, i.e. three translations and three rotations (AlignRT User Guide, 2015). Furthermore, the margins might be set with regard to specific indications and center-specific imaging and treatment protocols. Figure 7 presents an exemplary AlignRT software window with calculated RTDs. The AlignRT allows for patient's breathing monitoring during the treatment or performs treatments in a single breathing phase, e.g. maximum inhale or maximum exhale. Also, gated X-ray imaging might be achieved. In case when a patient overpasses the predefined thresholds regarding RTDs, the beam will be automatically turned off.

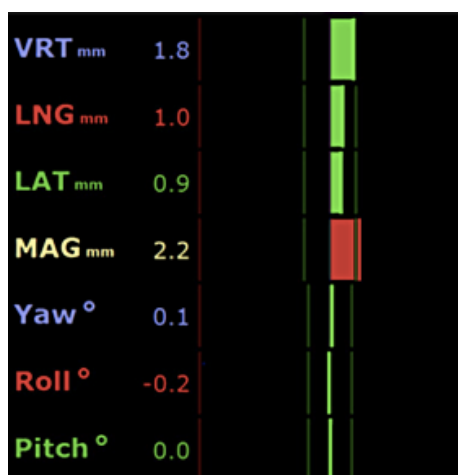


**Figure 7** AlignRT software: an example of real time deltas (RTDs) calculation (reproduced from AlignRT User Guide, 2015)

The GateRT application uses one of the AlignRT's centrally positioned cameras to track respiratory motion online. It enables the amplitude- or phase-gated treatments, i.e. automatic beam-off when the patient is not within the correct treatment or breathing position (GateRT User Guide, 2015). Both AlignRT and GateRT applications are combined with the UBTI (Universal Beam Triggering Interface) unit of the IBA system, thanks to which the gated treatments and gated X-ray imaging are possible.

The systems presented above, e.g. proton pencil beam scanning delivery technology, proton treatment planning and optical surface imaging systems, were used to achieve the main goals of this dissertation, outlined in Chapter 2.



## 2. Aim and outline

Preparation of treatment planning and quality assurance procedures is always a complex issue in radiotherapy. Clinical implementation is mainly based on a thorough analysis of the worldwide-known and published guidelines and the experience of other radiotherapy facilities. Cyclotron Centre Bronowice, as part of the Institute of Nuclear Physics Polish Academy of Sciences, is a perfect place for developing and working on new solutions due to the accessibility to the excellent academic and scientific staff and unique accessories, including the IBA Proteus C-230 cyclotron for proton radiotherapy purposes.

The motivation of this work was to develop the methodology and validate available radiotherapy tools at Cyclotron Centre Bronowice (CCB) IFJ PAN, which could enable and support the treatments of moving targets in the future. According to the Regulation of Ministry of Health of 6 July 2016 (Journal of Laws, item 855) (acronym *from Polish* “Rozporządzenie Ministra Zdrowia z 6 czerwca 2016 r. zmieniające rozporządzenie w sprawie świadczeń gwarantowanych z zakresu leczenia szpitalnego”, 2016), proton radiotherapy can be used, and funded by the government, only to treat a few types of cancer, i.e. base of the skull tumors, perinasal sinuses tumors or low grade gliomas. Therefore, the tumors which are under the subject of motion, e.g. breast cancer or lung cancer, are not included in the list. However, as these indications, based on available clinical and research explorations, are predisposed to be treated with proton radiotherapy with a successful and meaningful dosimetric advantage, they are the main focus of the study below.

To justify the use of proton beams in breast and lung cancer treatments, and verify their clinical implementation possibility, based on the available at CCB IFJ PAN accessories and radiotherapy equipment, a series of studies were conducted to verify these assumptions. The cooperation with radiation oncologists and medical physicists from Radiotherapy Center NU-MED, Elbląg, Poland was of significant importance. It

enabled me to perform a big part of the work regarding the breast cancer proton treatments included in this dissertation. The NU-MED Radiotherapy Center shared the anonymized imaging data of breast cancer cases to perform the retrospective study comparing photon and proton treatments and the optimization of the proton treatment planning for breast cancer. Furthermore, to execute the dosimetric comparison and prepare a basis for future protocol, which could be used at CCB IFJ PAN for breast cancer treatment planning with proton beams, the following steps were taken to assess these goals:

- (1) the retrospective comparison between photon and proton treatment planning verifying the legitimacy of using proton therapy, which is not as affordable and accessible as photon radiotherapy in Poland, and evaluating the possible dosimetric advantage, its scale and significance, which could be projected into the therapeutic effect;
- (2) evaluation of the significance of proper beam angles selection and optimization with regard to the breast cancer proton PBS treatment planning; based on the literature studies and no existing, consistent guidelines for the beam selection, the study includes a comparison of five beam arrangements regarding the dose to critical organs, as well as the robustness results and possible motion impact on each planning scenario quality.

Moreover, to conduct the studies for lung cancer, which the CIRS Dynamic Thorax Motion Phantom mimicked, several activities were undertaken to evaluate the possibility of using CCB IFJ PAN infrastructure for such treatments in the future, while taking into account the necessity of monitoring and minimizing the motion impact on the planned dose distribution:

- (1) performance and evaluation of the time-resolved computed tomography with the use of CIRS Dynamic Thorax Motion Phantom and GateCT application, used for motion monitoring, recording of breathing patterns

and subsequent use of these data for 4DCT reconstruction into the individual breathing phases;

- (2) the 4DCT preparation for treatment planning purposes with the use of various optimization algorithms to assess the dosimetric differences and promptness of using specific optimization procedures in the lung cancer treatment planning; moreover, the functionality of robust 3D optimization, performed with the NUPO (Nonlinear Universal Proton Optimizer) algorithm, was validated and compared against the PCS (Proton Convolution Superposition) optimization, regarding the robustness results and each algorithm sensitivity to the possible, at the stage of treatment delivery, perturbations;
- (3) the validation of possible use and implementation of *rescanning* modality at CCB IFJ PAN, verified with the measurements of single spots, monoenergetic layers (15x15 cm<sup>2</sup> fields), as well as the treatment plans prepared in step (2), with various detectors, thus evaluating the impact of the *rescanning* application on the minimization of the *interplay effect*, resulting from the overlapping of the time structure of the target and beam dynamics.

The dissertation is organized in the following order:

- Chapter 3 presents an introduction to radiation therapy and reviews previously and currently used radiotherapy techniques in cancer treatments;
- Chapter 4 is focused on the physics behind the radiation therapy phenomena and the major differences between commonly used photon radiotherapy, and less accessible proton beams, to which technique this thesis is dedicated;
- Chapter 5 introduces the meaning of *moving targets* and presents the clinical significance of motion consideration during imaging, treatment planning and dosimetry, as well as provides the clinical aspects and challenges in breast and lung cancer treatments;

- Chapter 6 presents the definition and implementation of a dedicated CT scanner calibration curve;
- Chapter 7 and Chapter 8 are dedicated to the comparative study of photon and proton plans' dosimetric outcome in breast cancer, and the optimization of beam arrangement to create the most robust and motion-resistant plans;
- Chapter 9 is the introduction to lung cancer treatments implementation at CCB IFJ PAN, which includes 4D imaging, treatment planning with or without robust 3D optimization, validation of *rescanning* modality and dosimetric testing;
- Chapter 10 gives an outlook and concludes the most important results.

The dissertation presented below was conducted at CCB IFJ PAN, partially in cooperation with Radiotherapy Center NU-MED (Elbląg, Poland), and supervised by assoc. Prof. Renata Kopeć, Head of the CCB IFJ PAN facility. The results, apart from the photon treatment planning presented in Chapter 7, prepared for the therapy purposes by the specialists at NU-MED Radiotherapy Center, were personally conducted by the author. The measurements executed in the gantry room were supported by employees of the Dosimetry and Quality Control Laboratory at CCB IFJ PAN, for which the author is most grateful.

### **3. Radiation therapy**

According to the World Health Organization statistics, cancer is currently the leading cause of death worldwide. In 2018, the new cancer incidents surpassed 18 million new cases and nearly 10 million deaths. According to the WHO Report on Cancer (WHO, 2020), these numbers could nearly double in the next twenty years, especially in Low-to-Middle-Income Countries. The most frequently appearing indications are breast, lung, colorectal and prostate cancer. It is also important to underline that, in recent years, the incidence level of female breast cancer has significantly risen, being the most commonly diagnosed type of cancer worldwide (Sung et al., 2021). These numbers and evidence are indisputable arguments for increasing society's awareness of the huge importance of undergoing cancer screenings and paying attention to early diagnostics.

For many years now, radiation therapy has been considered one of the standardly used treatments to cure cancer. The clinical rationale for exploiting radiation to destroy cancer cells lies in the physical properties of used beams and their interactions with matter. Thanks to many developments and new technologies that have been clinically implemented in recent years, radiotherapy has become a type of treatment, in which many interdisciplinary fields can be combined to offer the best possible, nearly personalized treatment. The background and beginnings of radiation therapy can be traced back to the very important events at the turn of the 20th century in physics. Many great scientists have to be mentioned because of the significant influence of their work on the early days of medical physics. From the X-rays discovery in 1895 by Wilhelm Roentgen, through the introduction of radioactivity in 1896 by Henri Becquerel, to the 1898 year, when polon and radium elements were discovered by Marie Skłodowska-Curie and Pierre Curie. These groundbreaking findings became the solid foundations of what we nowadays call radiation therapy (RT) (Bortfeld & Jeraj, 2011).

Radiotherapy, together with surgery and chemotherapy, is one of the major and important cancer treatments. The ionizing radiation (e.g. high-energy X-rays, electrons, gamma rays, protons) is used to kill cancer cells thus reducing and destroying malignant tissues. Cancer cells, in which the DNA repair mechanisms are defective, cannot proceed with the reconstruction and as a result, the damaged cells die (Biau et al., 2019). Normal cells, which might be irradiated due to the proximity to the target, can repair radiation-induced damage to some extent. However, if the radiation damages the normal cells up to a point, where they would no longer be able to perform repair processes, the late side effects and the probability of secondary cancer induction might play a huge role in the following years after radiotherapy.

The radiation treatment can be given with four intents: radical (curative), palliative, adjuvant or neoadjuvant. The curative treatment aims to cure cancer completely and often may be combined with chemotherapy, which is widely used in head and neck cancer cases. The main intent of palliative treatment is to increase the symptoms control in patients who have incurable cancer and to provide pain relief. Adjuvant and neoadjuvant therapies relate to radiotherapy after or before the definitive procedure, respectively. Adjuvant irradiation may be added as prevention to curable surgery to minimize the probability of local recurrence, e.g. in the case of breast cancer. The neoadjuvant treatment is often used in patients before the surgery, mainly to provide tumor shrinkage, which will allow the surgeons to perform the procedure with increased chances and control of that specific cancer. The neoadjuvant treatment is often used in rectal cancer (Murray & Lilley, 2020).

Two main types of radiotherapy can be differentiated, i.e. teleradiotherapy with external beam radiation therapy and brachytherapy, a form of internal, local treatment, where the radiation source is placed within or nearby the tumor. Radioactive sources such as, e.g. Iridium-192, Iodine-125 or Palladium-103 are used and with regard to their activity (dose rate) and time of implant application, the brachytherapy could be differentiated to low-dose rate (LDR), medium-dose rate (MDR), high-dose rate (HDR) or ultra LDR (Skowronek, 2017).

External RT (teletherapy) is a non-invasive method in which the radiation is delivered from the outside of the body. Nowadays, mainly high energy photon beams produced in medical linear accelerators are used, and to a lesser degree, also electron and proton beams. The chosen technique mostly depends on the indication, technique features, proximity to normal tissues, and certain methods availability. The modern external RT techniques have significantly improved over the last years. Also the accessibility to the newest and the most technologically advanced methods has risen. The gravitation towards improved target conformality and minimization of the radiation burden to the surrounding, healthy tissues can be distinguished as the main direction of the new developments. In the photon radiotherapy timeline, the crucial moment was the appearance of multileaf collimators in clinical practice (Jordan & Williams, 1994) and the introduction of intensity modulated techniques such as, e.g. Intensity Modulated Radiation Therapy (Brahme et al., 1982; Bortfeld, 2006). Based on these two cornerstone developments, the following methods, enabling to perform more advanced treatments than 3D conformal radiation therapy (3D-CRT), were proposed, i.e. tomotherapy (Mackie, 2006) and volumetric arc therapy (Otto, 2007). The important fact to add is that besides the advancements in the photon beam delivery methods, the imaging techniques were also improved, which allowed for more accurate treatment delivery. To summarize, the current possibilities of photon beam treatments are vast and impressive.

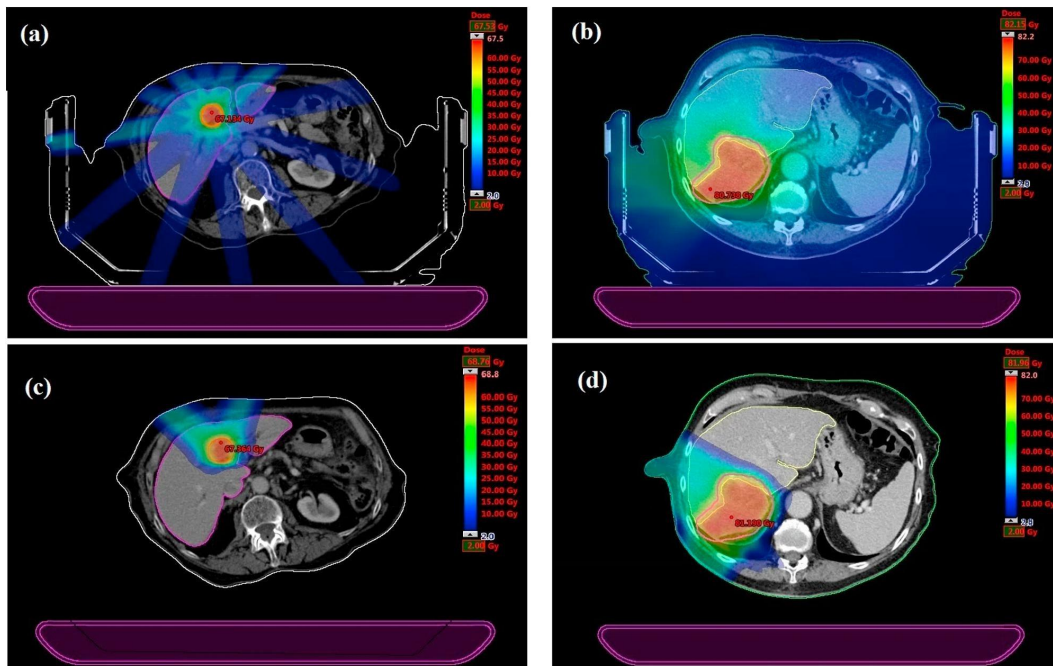


**Figure 8** Comparison of photon (top) and proton (bottom) dose distributions in two patients with liver cancer: a) 3D-CRT, b) VMAT, c) and d) intensity modulated proton therapy (IMPT) (Mondlane et al., 2017)

The increasing attention and importance is also paid to radiotherapy using particle beams, mainly protons, which treatments are offered by more and more facilities worldwide (Czerska et al., 2021). The main advantage of proton therapy over other conventional approaches is directly linked to the physical properties of particles and their interactions with matter. The maximum dose deposition of a proton beam occurs near the end of the beam range, and the rapid loss of energy creates the so-called Bragg peak, with a relatively small entrance dose and almost no exit dose behind the Bragg peak region (Newhauser & Zhang, 2015). This feature of protons enables the significant reduction of radiation exposure to normal tissues (Figure 8), the integral dose to the body and, in consequence, leads to improved local control and overall survival rate (Lin et al., 2015; EBCTCG, 2011). The first therapeutic use of proton beams was proposed by Robert R. Wilson (Wilson, 1946). His groundbreaking work, entitled “Radiological Use of Fast Protons”, was published in *Radiology* in 1946. Since then, much work has been done to explore proton beam properties in a clinical setting and use them in cancer treatments.

## 4. The physics of radiation therapy

While passing through the matter, photons and protons undergo different interactions determining their characteristics and unique features. These processes result from the absence or presence of the electrical charge which implies a specific type of medium ionization. The works presented in this thesis mainly concern proton radiotherapy, however, to present an insight into photon interactions with matter, as well as to understand the major differences between proton and photon modalities, a short introduction to the photons physics is also presented in the section below.

### a. Physical interactions of photons with matter

High energy X-rays do not carry an electrical charge, meaning they indirectly ionize matter. For clinically used photons energy, the highest importance have mainly three processes, i.e. photoelectric effect, Compton (incoherent) scattering and pair production (Figure 9) (Podgorsak, 2005).

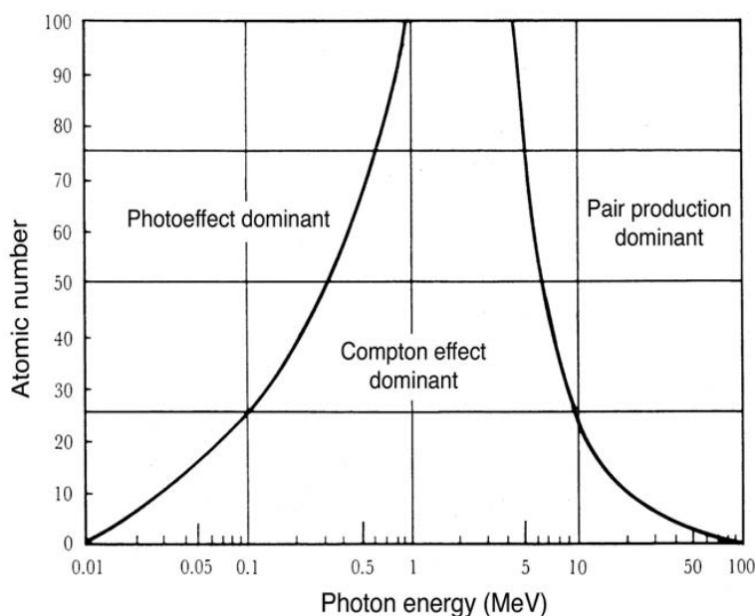


**Figure 9** Predominant interactions of photons with matter as a function of the atomic number and photon energy (Podgorsak, 2005)

The photoelectric effect (also: photoeffect) refers to the photon interaction with tightly bound electron and has the highest probability for low energy spectrum. As a result, an electron is ejected from the atom, thanks to the photon's energy transfer. Compton (incoherent) scattering occurs when the photon interacts with free orbital electron. Due to that electron's relatively small binding energy, the photon loses only a small part of its energy, and as a result of that interaction, scatters. The pair production occurs when the photon interacts with the electrostatic field of a nucleus, resulting in the proton's complete disappearance in exchange for a pair of electron-positron. It appears only for high energy photon beams. Based on mentioned processes, the typical depth dose distribution of a photon beam, after entering the medium, initially rises to create a so-called build-up region, and then decreases almost exponentially with the exit dose resulting from Coulomb interactions (Figure 10). The location of a build-up maximum mainly depends on the beam energy (Podgorsak, 2005).

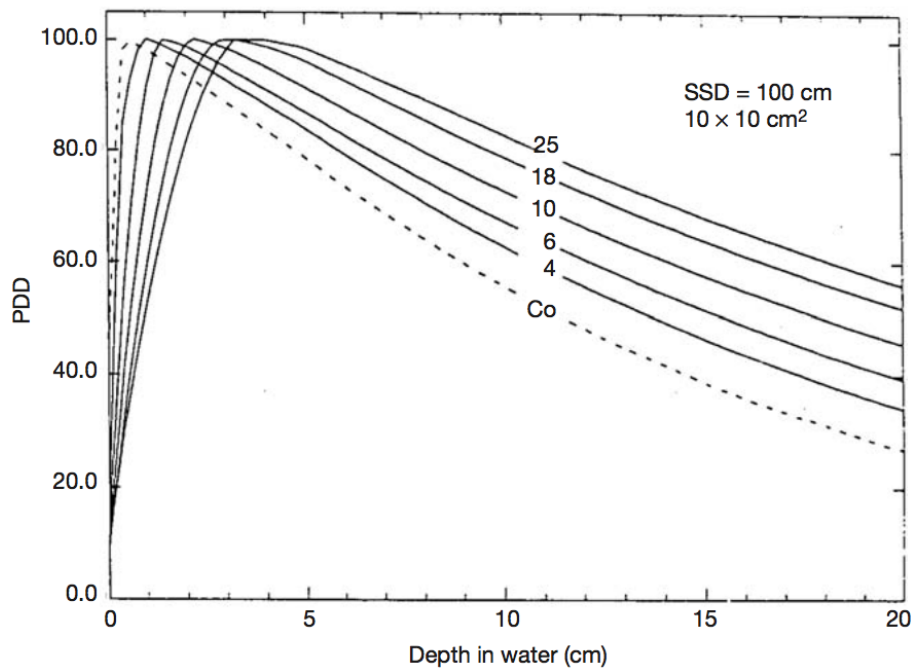


**Figure 10** Percentage depth dose distributions for photon beams of energies ranging from 4 to 25 MV (solid lines) and Co-60  $\gamma$  rays (dotted line) (Podgorsak, 2005)

## **b. Physical interactions of protons with matter**

Protons, as particles endowed with an electrical charge, cause direct ionization of the medium. They interact with matter via electromagnetic (EM) interactions with atomic electrons (stopping) or atomic nuclei (scattering), and might as well undergo nuclear interactions i.e., hard scatters, in collisions with nuclei themselves or their components. The fourth possible interaction is Bremsstrahlung (Paganetti, 2012; Paganetti, 2018), but due to the proton beams energy spectrum clinically used in radiotherapy, this process is negligible and will not be presented.

### **i. Stopping theory**

As they pass through matter, protons lose their energy in the electromagnetic interactions with atomic electrons. The rate of the energy lost ( $E$ ) per unit length ( $x$ ) is described as the stopping power ( $S$ ) and increases with the penetration depth, creating the so-called Bragg peak, thus determining the proton beam range (Figure 11). The dose after reaching this specific point, which depends on the beam's initial energy and the mass density of the absorbent material ( $\rho$ ), is almost negligible (Paganetti 2012). Therefore, the mass stopping power is defined as:

$$\frac{S}{\rho} = - \frac{dE}{\rho dx} \quad (1)$$

The phenomena of a Bragg peak is used in radiotherapy and constitute the most significant advantages of a proton beam over conventional approaches, i.e. finite range, which enables the creation of high dose distribution precisely within the target area and low entrance dose (*plateau*).

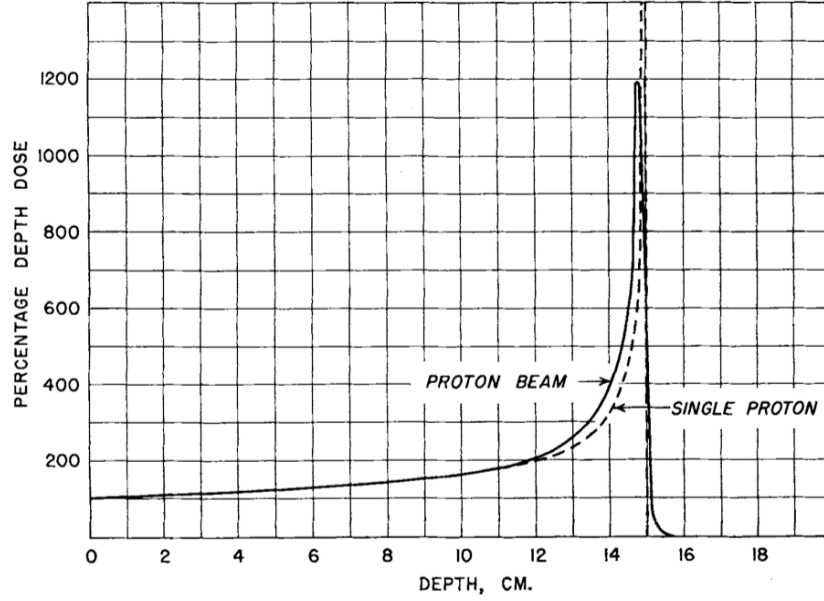


**Figure 11** Percentage depth dose distribution for a proton beam of 140 MeV energy (dotted - single proton beam, full curve - qualitative estimation of a monoenergetic beam of that energy) (Wilson, 1946)

To profoundly and quantitatively explain the stopping theory and the shape of proton beam depth dose distribution, including the quantum mechanics effects, the Bethe-Bloch formula should be presented (Newhauser & Zhang, 2015):

$$\frac{S}{\rho} = -\frac{dE}{dx} = 4\pi N_A r_e^2 m_e c^2 \frac{Z}{A} \frac{z^2}{\beta^2} \left[ \ln \frac{2m_e c^2 \gamma^2 \beta^2}{I} - \beta^2 - \frac{\delta}{2} - \frac{C}{Z} \right] \quad (2)$$

where,  $N_A$  is the Avogadro's number,  $r_e$  is the classical electron radius,  $m_e$  is electron mass,  $Z$  and  $A$  are the atomic number and the mass number of the absorbing material,  $z$  and  $v$  are the charge and velocity of the projectile,  $c$  is speed of light,  $\beta$  is the particle velocity in the speed of light units,  $\gamma = (1 - \beta^2)^{-1/2}$ ,  $I$  is the mean excitation potential,  $\delta$  and  $C$  represent density and shell corrections. Taking into account the protons energy spectrum, which is clinically used in radiotherapy ( $\sim 3$ -300 MeV), the Bethe-Bloch formula describing the mass stopping power can be simplified and presented as:

$$\frac{S}{\rho} = 0.3072 \frac{Z}{A} \frac{1}{\beta^2} \left[ \ln \frac{W_m}{I} - \beta^2 \right] \left[ \frac{\text{MeV}}{\text{g/cm}^2} \right] \quad (3)$$

where  $W_m$  represents the highest possible energy loss in a single interaction with a free electron and is described as follows:

$$W_m = \frac{2m_e c^2 \beta^2}{1-\beta^2} \quad (4)$$

In the individual ionizing interactions of protons with atomic electrons of the absorbent material, only a small amount of their initial kinetic energy ( $E_{i,k}$ ) is lost (Grassberger, 2014). This process, of a particle gradually slowing down as passing through the matter, is called *continuous slowing down approximation* (CSDA) (Figure 12), and the  $R_{CSDA}$  range can be presented as a function of the mass stopping power and energy:

$$R_{CSDA} = \int_0^{E_{i,k}} \frac{dE \cdot \rho}{S(E)} \quad \left[ \frac{g}{cm^2} \right] \quad (5)$$

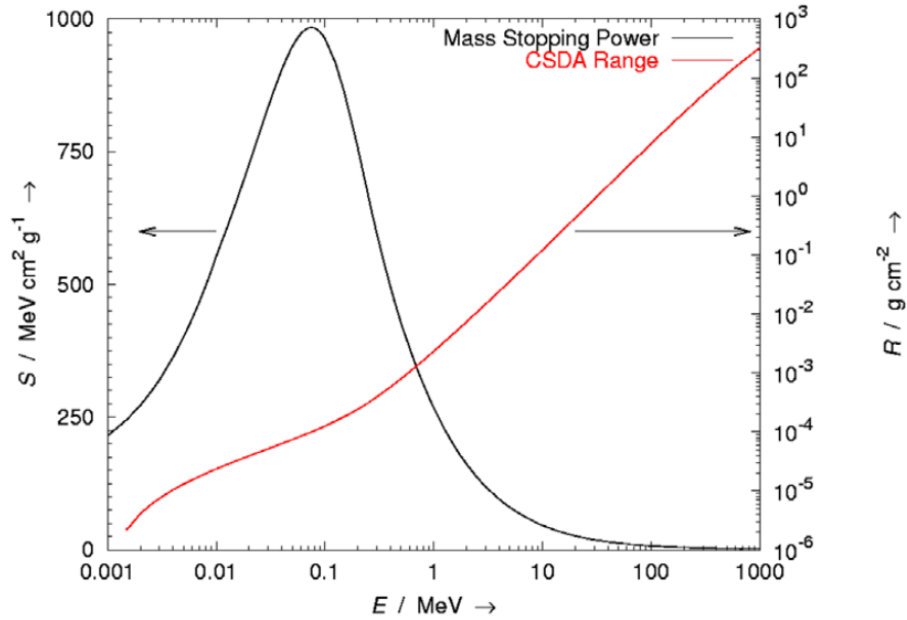


**Figure 12** The proton mass stopping power  $S/\rho$  and the corresponding  $R_{CSDA}$  range as a function of energy in water (Newhauser & Zhang, 2015)

The stochastic nature of protons' energy loss in matter also causes a phenomenon, which is called *energy straggling*. It is observed due to the fluctuations in particle interactions, even in a monoenergetic beam. The energy straggling can be approximated by a Gaussian distribution and thus described by the standard deviation  $\sigma_{rs}$ , determining the width of the Bragg peak, which mainly depends on a proton initial energy (Bortfeld, 1997; Paganetti, 2012; Paganetti, 2018).

## ii. Scattering theory

As they travel in medium, protons do not only stop, but also scatter mainly due to the interactions with atomic nuclei. The rate of a single deflection is very small and almost negligible, however, traveling protons are subject to multiple deflections of this kind in the nuclei's electric field. That process is called *Multiple Coulomb Scattering* (MCS) (Figure 13) and has a significant impact on the angular spread, i.e. determination of the lateral shape of the proton beam (Figure 14). The quantity of scattering power, representing the amount of deflected beam in an absorber of the thickness  $x$ , can be presented as:

$$T = \frac{d\langle\theta^2\rangle}{dx} \quad (6)$$

where  $\langle\theta^2\rangle$  is the mean squared scattering angle.

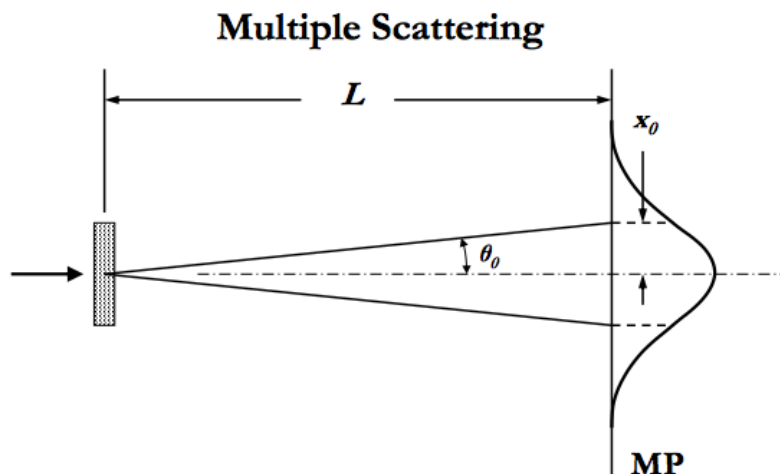


**Figure 13** Multiple Coulomb Scattering through a thin slab material.  $\theta_0$ - characteristic angle, a width of the angular spread,  $x_0$ - displacement,  $L$  - distance to the scattering material (Paganetti, 2018)

The angular distribution resulting from the MCS interactions can be sufficiently approximated by the Gaussian, while taking into account only proton energies used for radiotherapy purposes (Paganetti, 2018). Therefore, according to the Central Limit Theorem, the angular spread distribution can be described as:

$$f(\theta) d\theta = \frac{1}{\sqrt{2\pi}\theta_0} e^{-\frac{1}{2}\left(\frac{\theta}{\theta_0}\right)^2} d\theta \quad (7)$$

where  $\theta_0$  is the characteristic angle, a width of the angular spread. However, it is important to underline that the full angular distribution, in specific situations, i.e. Rutherford scattering of protons by nucleus, is not Gaussian exactly (Gottschalk, 2004; Paganetti, 2012).

The thorough foundation of scattering theory was developed by Molière (Molière, 1947; Molière, 1948), in which he described the characteristic multiple scattering angle  $\theta_M$ , introducing not one as in Gaussian approximation, but two quantities describing the scattering angle:

$$\theta_M = \frac{1}{\sqrt{2}} \left( \chi_c \sqrt{B} \right) \quad (8)$$

where  $\chi_c$  is the characteristic single scattering angle and  $B$  is the reduced target thickness (Gottschalk, 2004). That theory was later improved by the Fano correction, which includes the scattering by atomic electrons (Fano, 1954).

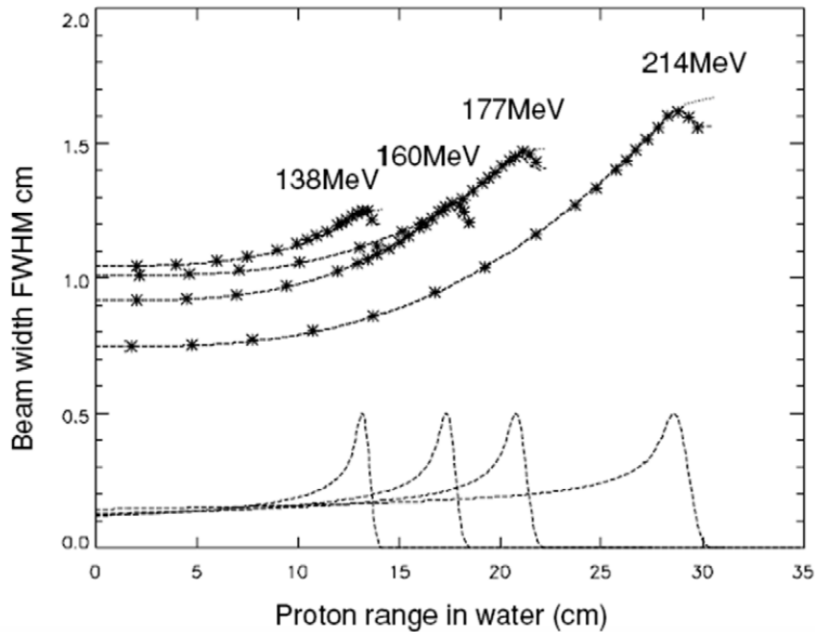


**Figure 14** Beam width broadening in water due to the Multiple Coulomb Scattering as a function of proton range (Pedroni et al., 2005)

### iii. Nuclear interactions

Additionally to the above mentioned electromagnetic interactions of protons, i.e. stopping and multiple scattering, around 20% of protons of energies used clinically might undergo the nuclear interactions via collisions with the atomic nuclei. These interactions can be divided into two groups with regard to the interaction target, i.e. *coherent* (nucleus) and *incoherent* (nucleus components) (Paganetti, 2018). Moreover, *elastic* (kinetic energy conserved, no excitation), *inelastic* (kinetic energy not conserved, target remains the same) or *non-elastic* (kinetic energy not conserved, target disintegrates, and new particles are produced, e.g. secondary protons, neutrons, deuterons, tritons,  $^3\text{He}$ ,  $^4\text{He}$ ) collisions can be differentiated (ICRU 63, 2001). As a result of the nuclear interactions, a part of the dose is removed by secondary products from the primary beam and placed outside of the irradiated volume, creating the so-called *halo effect*. Local dose coming from a single pencil beam could be negligible, however, its contribution from a whole set of proton beams, could significantly change its absolute value (Pedroni et al., 2005).

## **5. The clinical aspects of moving targets radiotherapy**

The definition of moving targets includes all the tumors whose position changes over the course of treatment, either in between fractions or within one fraction. It mainly concerns the tumors located in the thorax or abdomen due to the significant influence of, e.g. breathing, cardiac or peristalsis activity (De Ruysscher et al., 2015). The spatial, but also temporal changes in the target and organs location, may significantly influence the predefined, at the stage of treatment planning, dose distribution (Kardar et al., 2014; Li et al., 2014; Zhang et al., 2016; Liu et al., 2015). In recent years, stereotactic body radiation therapy (SBRT) and passively scattered proton therapy (PSPT) have been used to treat indications such as, e.g. liver or lung (Knopf et al., 2016). However, with the intensive evolution of PBS proton therapy, offering highly conformal dose distribution and even better OARs (organs at risk) sparing, the so far used treatment approaches had to be revised due to several uncertainties affecting pencil beams. The clinical implementation of 4D treatments is a very complex subject, which encompasses the revisions of all steps of the “static” radiotherapy path, starting from patient selection based on several metrics, through time-resolved imaging data, choice of adequate motion monitoring solution and mitigation approaches, treatment planning, dosimetry and dose evaluation (Czerska et al., 2021). Nevertheless, despite all these difficulties, many centers worldwide have decided to take up the challenge and include 4D treatments in their clinical practice (Chang et al., 2014; Meijers et al., 2019; Meijers et al., 2020).

There are three main timelines, on which we consider the motion from a clinical perspective (Figure 15). First is the whole course of treatment, which usually lasts five to seven weeks and mainly concerns the changes in the density distribution within the patient's body, e.g. tumor growth/shrinkage or patient weight gain/loss. The second, interfractional variations are considered on a fraction to fraction basis. These include changes related to, e.g. bladder, bowel or rectum filling, position and rotation of the

femoral heads during abdomen treatments or changes in the mean target position over the breathing cycle. Finally, the third group, intrafractional variations, includes the most dynamic changes within a single treatment fraction, closely related to breathing motion or cardiac activity (Paganetti, 2012).

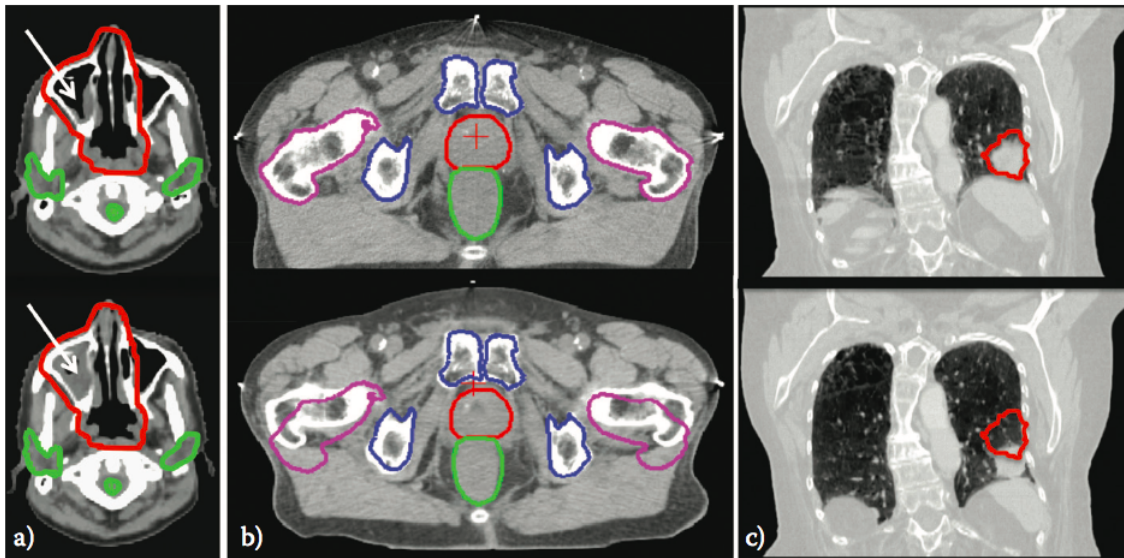


**Figure 15** The motion aspect as a function of time: a) the density changes in the head & case occurring during the whole course of treatment, b) the interfractional changes in the femoral heads position in the prostate case, c) the intrafractional changes in the lung tumor position (Paganetti, 2012)

#### a. Patient selection

Patient assignment to a concrete treatment procedure is always a difficult choice. As presented above, there are several advanced radiotherapy techniques that might be chosen in specific cases. The selection procedure is based on, e.g. the indication, anatomy, health condition, thorough motion analysis and amplitude evaluation. Firstly, the choice between photon or particle radiotherapy has to be always preceded by a profound analysis of the risks and benefits of far-reaching treatment goals, including physical properties of beams and biological effects (Durante et al., 2017). However, with the higher overall costs of the proton radiotherapy and the limited accessibility to this type of treatment, the resulting decision is always based on the profound investigation of each patient case individually by a group of experts, both physicians and physicists. Due to the various aspects, from purely clinical to economic ones, such as cost-effectiveness of the treatment and insurance coverage, the approach of patient

selection to photon and proton radiotherapy is always a vividly discussed topic during dedicated conferences and congresses. In recent years, there are countries that have developed the system of patient selection to certain radiotherapy approaches, e.g. the Netherlands (Langendijk et al., 2013; Grau, 2013). At present, in Poland, the patient selection is based on the Regulation of the Minister of Health dated 6 July 2016 (Journal of Laws, item 855) (acronym *from Polish* “Rozporządzenie Ministra Zdrowia z 6 czerwca 2016 r. zmieniające rozporządzenie w sprawie świadczeń gwarantowanych z zakresu leczenia szpitalnego”, 2016). Refunded by the Polish government, types of cancer are, e.g. low grade gliomas or base of the skull tumors.

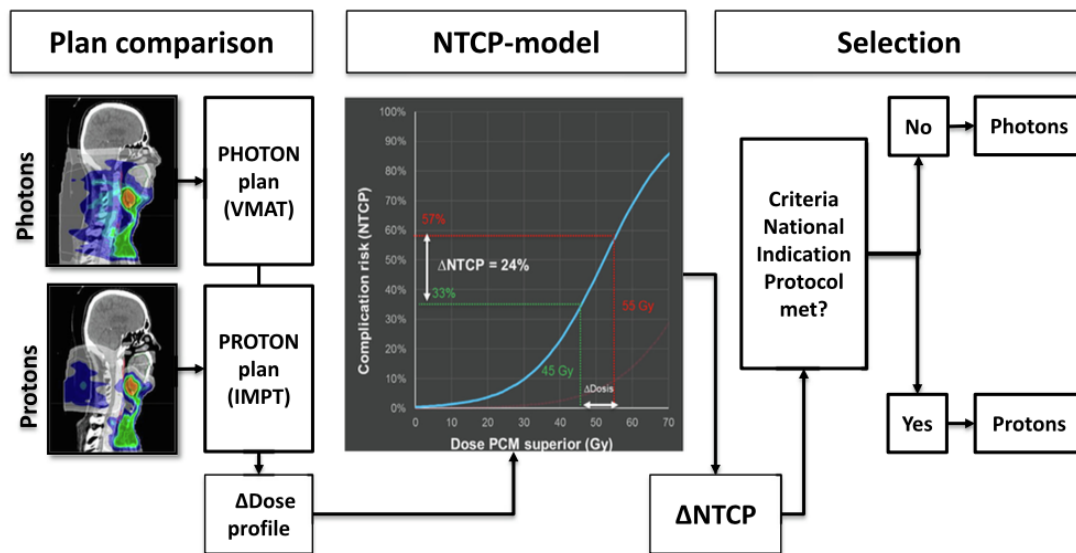


**Figure 16** An example of Dutch model-based for head and neck cases. Based on the photon and proton plans comparison, the dosimetric differences result in the delta NTCP, which plays the key role in the further patient assignment to the selected type of treatment (Tambas et al., 2020)

The main base, which constitutes that a certain type of treatment has advantages and brings many benefits over the others, is the introduction of randomized controlled trials (RCT). Although the first premises of using proton beams in cancer treatments appeared in the 50s last century, the PBS therapy, which has been rapidly evolving over the last ten years, is still relatively young compared to conventional radiotherapy techniques. Moreover, the RCTs, which prove and underline the clinical benefits of specific techniques, require long time periods to present the long-term follow-up

regarding the side effects and tumor progression. That is the main reason limiting RCT's use as the patient selection indicator in the rapidly developing 4D PBS treatments (Widder et al., 2016). For this reason, the Dutch patient's selection approach, a so-called model-based approach, is based on the comparative studies between photon and proton treatment plans related to the normal tissue complication probability (NTCP). First, the treatment plans are calculated and the doses to OARs are assessed. Then, these results are transferred to the corresponding NTCP values, which results in the NTCP delta. Subsequently, based on the NTCP delta, the estimated clinical gain is achieved. Together with the thorough analysis of the case severity, the certain case is assigned either to photon or proton radiotherapy (Figure 16). The procedure is based on the nationally accepted consensus guidelines and acceptance levels.

Within the 4D cases themselves, the procedure is mainly based on the 4DCT imaging modality and thorough motion analysis. The investigation should include, e.g. the type of tumor, its size, anatomical location and the maximal motion extent. At this stage, a significant fact is to estimate possible internal-external motion correlations, because these are not always straightforward, and the surrogate's external signal, e.g. from the chest wall, may not necessarily reflect the internal motion of the tumor (Knopf et al., 2016; Liu et al., 2007; Bertholet et al., 2019). According to the PTCOG Thoracic and Lymphoma Subcommittee consensus guidelines, the acceptance criteria for 4D treatment based on the tumor motion threshold should be carefully analyzed and established for each institution independently (Chang et al., 2017).

#### **b. Motion monitoring and mitigation approaches**

Proper selection of motion monitoring and mitigation methods is crucial in 4D treatments. The main aim of determining the necessity of their application is to include the inter- and/or intrafractional anatomical changes in the 4D imaging, 4D treatment planning and 4D evaluation processes to possibly minimize the deteriorating influence of motion on the dose distribution. Currently, there are several methods for both, motion monitoring and mitigation approaches, and center-specific protocols are often prepared based on the available 4D tools and software solutions.

There are two main groups of motion mitigation approaches that may be used to minimize the deteriorating effect of motion, i.e. passive and active techniques, together with additional accessories and immobilization techniques, which aim to reduce motion amplitude and support the positioning process (Czerska et al., 2021). The decision of whether the application of a motion mitigation approach is needed is often based on the tumor amplitude and center-specific predefined threshold (Knopf et al., 2016). When the tumor amplitude does not exceed the specific threshold, a passive motion mitigation approach, in the form of target margins or rescanning (also: repainting) technique, might be applied (Ehrbar et al., 2017; Bert et al., 2014). The first solution refers to the application of margins, which will encompass all tumor positions over the whole breathing cycle, and the second, *rescanning* refers to the delivery of the calculated spots in many iterations to smooth out the dose distribution and prevent the so-called *interplay effect* (Chang et al., 2017). The *interplay effect* results from possibly overlapping time structures of the tumor and scanning beam itself, which might cause severe under- or overdosages of the tumor volume, affecting the homogeneity of the planned dose distribution (Figure 17).

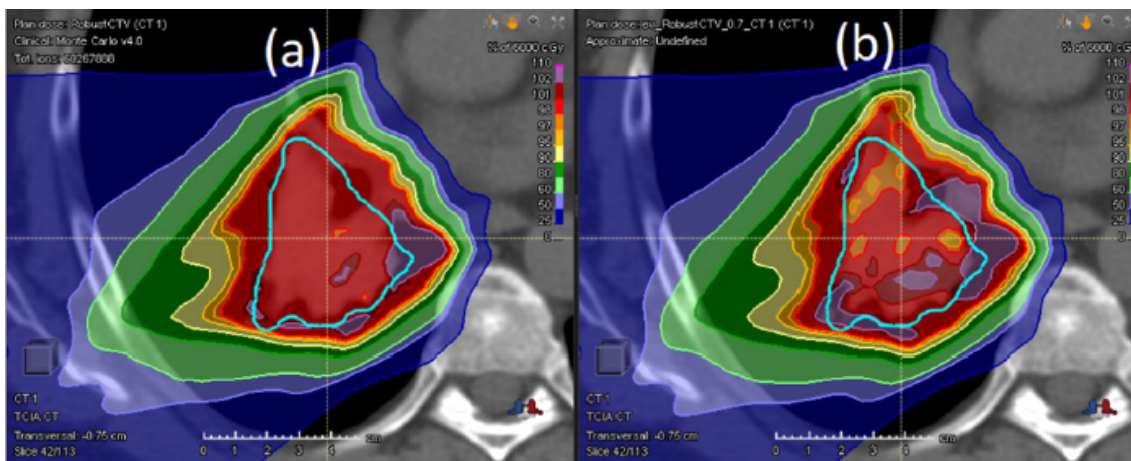


**Figure 17** Presentation of an interplay effect for a lung cancer case: a) reference (nominal) plan and b) perturbed dose distribution (reproduced from Engwall et al., 2018)

There are two main *rescanning* strategies, i.e. volumetric and layered, commonly used to minimize the dose distortions occurring by the similar time scales of motion and beam dynamics. In the volumetric, the whole 3D target is repainted several

times and in the layered, on the other hand, each layer is rescanned in several iterations (Engwall et al., 2018). The principle of layered rescanning is presented in Figure 18.

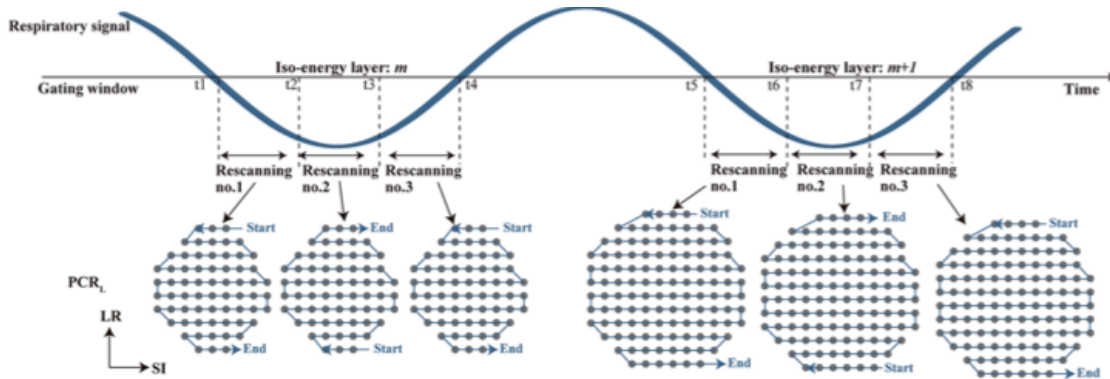


**Figure 18** The idea of layer repainting: each layer is delivered several times (here: three) to smooth out the deterioration of dose distribution resulting from the interplay effect (Mori et al., 2018)

If the tumor motion exceeds the predefined motion amplitude threshold, an application of the active motion mitigation approach, requiring the additional use of motion monitoring, might be vital. These include, e.g. optical surface imaging methods supporting breath hold and gating treatments, fluoroscopy imaging, the application of fiducial markers, etc. The optical methods are based on the external surrogate signal, e.g. chest wall, and use that signal to control the motion. These methods have many advantages, i.e. are non-invasive and do not require additional radiation to track a patient's anatomy (Fattori et al., 2017). The significant drawback, which was also mentioned earlier, is that they might not exactly reflect the internal target motion, and that careful attention should be paid to the motion models describing correlations between internal and external signals (Bertholet et al., 2019). Fluoroscopy-based imaging has found the application in real-time treatments and is a base of real-time image-guided proton therapy (IGPT) at Hokkaido University (Matsuura et al., 2013; Shimizu et al., 2014). That solution is widely used there in the thorax and abdominal treatments of lung, pancreas, liver and prostate cases.

The breath hold and gating techniques refer to the tumor irradiation in selected breathing phases. Breath hold has been widely used for many years in photon radiotherapy of breast cancer, because it increases the gap between the tumor and

critical organs such as the heart, ipsilateral lung and cardiac substructures, i.e. left anterior descending artery (LAD) (Smyth et al., 2015). The irradiation is enabled only when the patient is in the correct position and coached to take a breath in or breath out. Optical systems, e.g. VisionRT, used to track the anatomy in these kinds of treatments, have defined thresholds, which automatically stop the irradiation when the patient exits the intended position. Another group of motion monitoring methods are systems based on spirometry. They allow to obtain a more reproducible and stable signal, which significantly impacts the 4D dose delivery. As examples of active breathing control, providing regular and even distributed breathing, the Nasal High Flow Therapy (NHFT) (ARIVO©) and the SDX System® can be distinguished. From the 4D planning point of view, there are two more approaches that might support the minimization of the negative influence of breathing on the dose distribution, i.e. enlargement of the spot size, which reduces deteriorating effects of motion, and choosing the optimal scanning direction, as a solution to minimize the possible consequences of *interplay effect* (Li et al., 2015).

To summarize, the choice of the best motion mitigation and monitoring approach is often dictated by available at specific center 4D tools supporting imaging, treatment planning and delivery processes. Moreover, the mitigation and monitoring solutions are often combined in order to achieve the best possible treatment workflow for a specific case, based on the center's capabilities.

### **c. 4D imaging and contouring**

The possible redistribution of density within the patient's body over the course of treatment and the inter- and intrafractional changes, might cause significant deterioration of a planned dose distribution. It is due to the high sensitivity of proton beams to the treatment uncertainties. However, even though the PBS technique is highly technologically demanding itself, as it is in the treatment of moving targets, many clinical and research studies have proved that the promising outcome is worth further investigation and work.

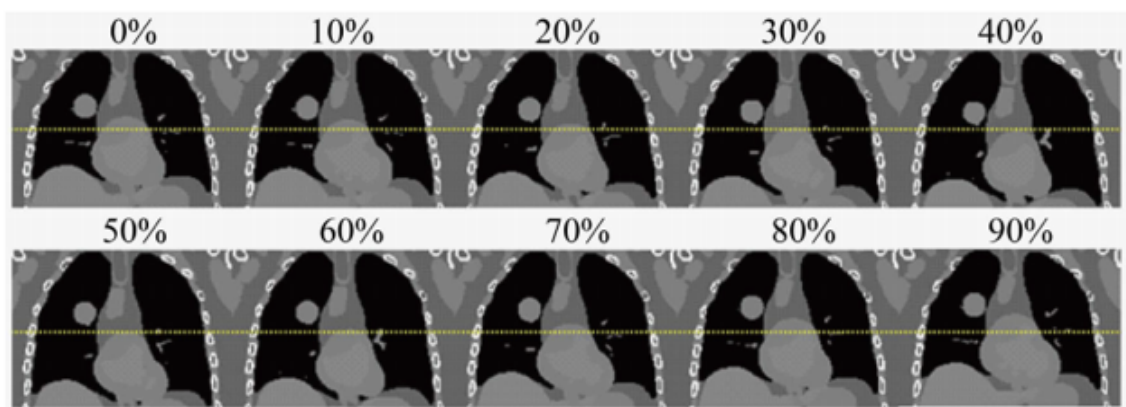


**Figure 19** The 4DCT of a breathing phantom 4D XCAT with inserted lung tumor, reconstructed to ten breathing phases and presenting the changes in tumor position over the whole breathing cycle (Cai et al., 2014)

The accurate delineation of the target volume and all OARs, especially in the close surroundings to the tumor, are the base of radiotherapy. The increased complexity of four-dimensional (4D) imaging results from additional information that has to be included at the contouring stage, i.e. the motion aspect. Universally used 4D imaging modality in many centers worldwide is the time-resolved CT, so-called 4DCT. The 4DCT is acquired with the inclusion of breathing information during the CT scan. Subsequently, based on, e.g. imaging protocol, breathing pattern, indication, imaging and respiration data, the CT might be reconstructed into certain breathing phases. Depending on the chosen number of time-percentage bins, it might be, e.g. ten breathing phases, in which case the 0% phase reflects the maximum inhale and the 50%, the maximum exhale breathing phase (Khamfongkhrua et al., 2017) (Figure 19).

Moreover, having the 4D image and breathing pattern information, other 3D imaging might be reconstructed, e.g. average, maximum intensity projection (MIP) or mid-ventilation (MidV) CT scans (Kang et al., 2007; Wolthaus et al., 2006). Recently, the emerging interest has also been focused on the 4D magnetic resonance imaging (4D-MRI), which allows for better soft-tissue representation and might support the processes of delineation and treatment planning (Krieger et al., 2020). This also applies to positron emission tomography (PET) and the contrast-enhanced CT, especially in liver cases (Bradley et al., 2012; Jensen et al., 2014).

To encompass the tumor positions over the breathing cycle, usually, a structure called an internal target volume (ITV) is created (Knopf et al., 2010; De Ruyscher et al., 2015; Muirhead, 2008). It is a commonly used margin approach employed in the delineation process of moving targets. However, to explain the basis of the ITV, an introduction of all stages of target delineation is necessary. Important to underline is that the approach of target definition in radiotherapy has been changing over the last years, which is presented in Figure 20. Nowadays, the gross tumor volume (GTV) is created as a tumor *base*, and according to the ICRU78, it contains “*gross palpable, visible, or clinically-demonstrable disease*” (ICRU 78, 2007). Subsequently, with additional margins including the subclinical changes around the GTV, the clinical target volume (CTV) is defined. Then, to include tumor motion extent due to breathing, the ITV is created, either as a sum of all tumor positions in the reconstructed breathing phases of 4DCT or a union of extreme phases, i.e. maximum exhale and maximum inhale.

Moreover, not only the 4DCT itself is used in the contouring process, but also mentioned above MidV or MIP images. The MIP images might be instrumental in delineating lung cancer surrounded by low-density soft tissue (Timmerman & Xing, 2010). The choice of exact contouring approach depends on the center-specific imaging protocol. Once the ITV is created, the next step of 4D contouring is to include the possible occurrence of statistical and random uncertainties, which might be present during the delivery process. The idea is to account for these perturbations at the contouring and treatment planning stage, and often, the well-known van Herk formula is employed (van Herk et al., 2000). Apart from additional safety margins, also density override, to the target volume or specific OAR is used in certain planning cases.

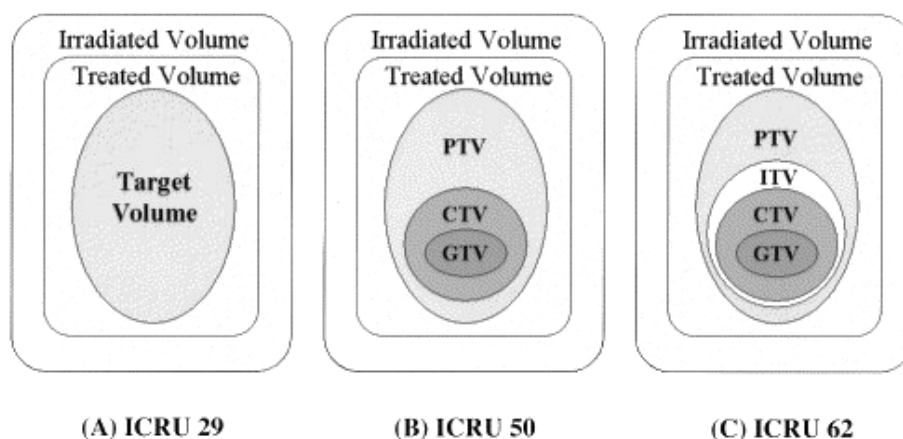


**Figure 20** The idea and evolution of the target definitions according to the a) ICRU 29, b) ICRU 50 and c) ICRU 50 reports (ICRU 29, 1978; ICRU 50, 1993; ICRU 62, 1999); reproduced from (Purdy, 2004)

#### **d. 4D treatment planning**

##### **i. Significance of beam angles selection**

In accordance with the PTCOG Thoracic and Lymphoma Subcommittee consensus guidelines, the general recommendation regarding the angles selection, a first step in the treatment planning process, is to choose as parallel beam direction to the major motion direction as possible (Chang et al., 2017). The basis of this theory is the physical characteristics of protons and the ability to create sharp and steep fall off behind the Bragg peak region, which is highly sensitive to any density variations at the beam path. As a result of such variations, a severe over- or underdosage might affect the planned dose distribution and have a huge influence on the dose to surrounding OARs. The additional aspect, for which the general rule of avoiding the beams stopping near critical organs is vital, are the possible variations in the relative biological effectiveness (RBE) of protons (Lühr et al., 2018). Proton centers, usually in their clinical practice use their own center-specific guidelines to plan exact indications and there are certain trends that might be mentioned. As an example, for lung cancer, usually two or three irradiation fields allow to create conformal dose distribution and, e.g. for tumors placed in the lower lobe of the lung, posterior and posterior-oblique beam directions might be used. In the case of breast cancer, a commonly used approach is to apply one en-face

beam, whose direction coincides with the main motion direction. However, there are also many other planning techniques for breast cancer presented in the literature, e.g. the use of two or three beams. Nevertheless, despite differences among centers, the general PTCOG guidelines have been widely considered and clinically implemented (Chang et al., 2017).

## **ii. Proton pencil beam scanning algorithms**

There are two proton PBS algorithms in the Varian Eclipse Treatment Planning System (versions 13.6, 16.1), i.e. the Proton Convolution Superposition (PCS) and the Nonlinear Universal Proton Optimizer (NUPO), which differ significantly in terms of the optimization capabilities (Varian Medical Systems, 2013). The main difference between algorithms is the definition and representation of volumes, which have a significant impact on the subsequent selection of spot positions and starting weights. Despite the fact that the NUPO algorithm requires a separate calculation model for optimization purposes, the beamline and resulting dose calculation is based on PCS. However, the added value of choosing NUPO during plan creation is the ability of robust 3D optimization performance with regard to the selected perturbations and chosen volumes. This functionality is not available in the PCS optimizer (Varian Medical Systems, 2013).

## **iii. 3D and 4D robust optimization**

As presented in the proton interactions with matter section, the proton beams might be severely affected by any density changes along the beam path due to the creation of sharp and steep fall off behind the Bragg peak region. Therefore, the inclusion of possible uncertainties at the treatment planning stage is vital. In protons, unlike in photons, the differences between planned and actually delivered dose distribution might vary between 0% and 100% in case of perturbations along the path (Paganetti, 2012). The robust optimization, either 3D or 4D, has to be applied to account for the uncertainties during the treatment plan calculation. The main issues, which might affect the dose distribution, are: patient setup uncertainty, curve calibration error, interplay effect, fractionation scheme, beam delivery or the anatomical changes.

Previously mentioned passive techniques of motion management might not be sufficient to overcome the deteriorating impact of uncertainties, therefore, the motion management methods are usually combined to obtain the best possible and uncertainty-resistant treatment plan (Knopf et al., 2016). For the PBS technique, the robust optimization has significant meaning in the IMPT planning, because of the highly non-homogeneous dose distribution within a single field, unlike in the SFUD (Single Field Uniform Dose) technique, where the application of, e.g. additional range-adapted margins might be sufficient. Two robust optimization methods might be differentiated, i.e. the robust 3D (3DRO) and robust 4D optimization (4DRO). The 3DRO considers two main perturbations affecting the plan quality, the uncertainty of patient setup and the curve calibration error. The 4DRO, apart from the mentioned aspects, also takes into account the motion pattern, because the plan is optimized regarding selected breathing phases of the 4DCT, which allows for advanced motion consideration at the treatment planning stage (Figure 21). So far, only a few clinical studies investigating the clinical significance and necessity of 4DRO application have been published (Knopf, **Czerska** et al. 2022).

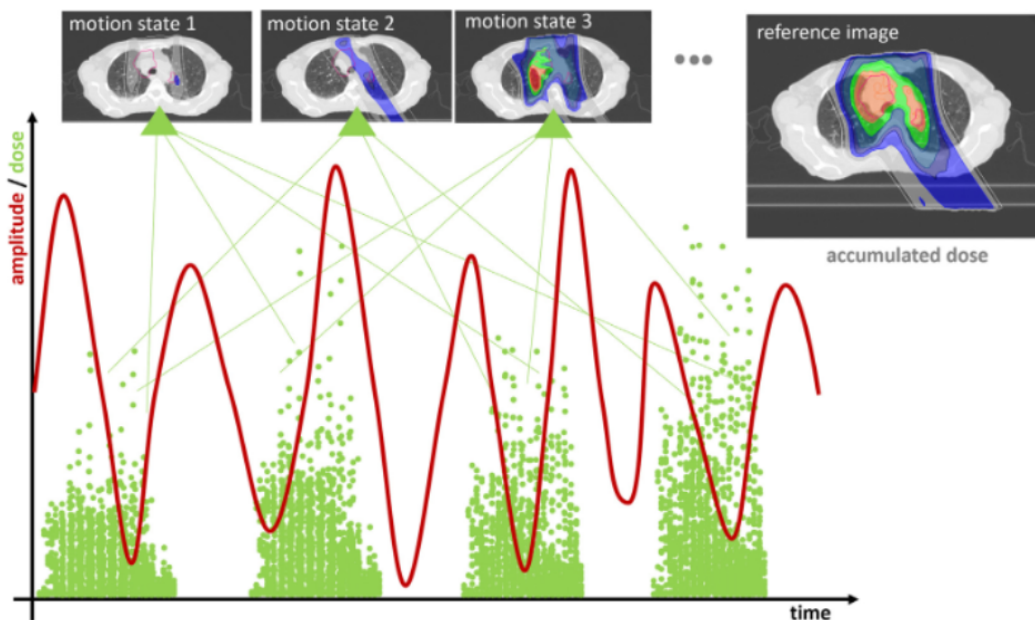


**Figure 21** The principle of 4DRO including the beam delivery and motion aspect in the optimization process (Knopf, **Czerska** et al., 2022)

**e. Clinical challenges of moving target treatments - breast cancer and lung cancer cases**

According to GLOBOCAN 2020 (International Agency for Research on Cancer, Global Cancer Observatory) estimates of incidence and mortality of cancer, female breast cancer has the highest incidence rate in both sexes and overpassed lung cancer, which has been so far the most commonly diagnosed malignancy. Moreover, it is currently the first leading cause of cancer death in females and has reached the level of 15.5% (Sung et al., 2021).

For many years now, radiotherapy has been widely used as a breast conserving therapy, following, e.g. lumpectomy, in order to decrease the risk of possible recurrence and also to improve the overall breast cancer survival rate. However, the main concern of using any kind of external radiation therapy is associated with possible late effects following the treatment. In the case of breast cancer, due to its anatomical placement, i.e. proximity to the heart, cardiac substructures and lung, an increased cardiac toxicity, radiation-induced pneumonitis, arm and shoulder function restraint or secondary malignancies development might be included (Mutter et al., 2021). Therefore, the minimization of unwanted dose to surrounding healthy tissues is vital, when any radiation treatment is considered. Thanks to the new developments and improvements in the radiotherapy field, the influence of late toxicity effects can be minimized, improving thus the quality of life of patients undergoing breast cancer treatment (Corbin & Mutter, 2018).

In recent years, various photon techniques have been proposed to treat cancer. Advanced modalities such as intensity modulated radiation therapy (IMRT), volumetric modulated arc therapy (VMAT) or stereotactic body radiation therapy (SBRT) are techniques which aim to create a homogenous high dose region within the target structure, while minimizing the amount of unwanted dose to critical organs (Hug, 2018). However, the use of multiple beams to create conformal and high dose regions also increases the integral dose to the whole body (Taylor & Kirby, 2015). According to Mutter et al. (2021) it may be closely connected to higher secondary cancer risk

development. Since the proton pencil beam scanning (PBS) technique has become more accessible and affordable in many centers worldwide, various clinical and research studies have been conducted to evaluate its potential suitability for breast cancer treatments (Ares et al., 2010; Depauw et al., 2015; Corbin & Mutter, 2018).

Regardless of the radiotherapy technique, the radiation dose to the heart, cardiac substructures and ipsilateral lung is of major concern in breast cancer treatments. Apart from anatomical challenges, there are additional patient-specific factors having an impact on the mathematical models of normal tissue complication probability (NTCP), which predict the radiation-induced morbidities, e.g. existing comorbidities, genetic predispositions, age, smoking history or pre-existing heart disease. Patients whose medical records include these factors are in the group of higher risk of ischemic heart disease, serious cardiac morbidity or cardiopulmonary events following the course of breast radiotherapy (Mutter et al., 2021). According to Darby et al. (2013) there is a certain relation between dose to the heart and cardiac substructures, and ischemic heart disease. For each 1 Gy increase in the mean heart dose, there is a relative 7.4% probability of increased major coronary events (MCE), with no evident threshold below which there is no risk for the heart disease occurrence. There is also evidence suggesting that dose to the left anterior descending artery (LAD) might play a huge role in the atherosclerosis development (van den Bogaard et al., 2021). Other events, which may appear after the breast radiotherapy include, e.g. valvular dysfunction, coronary revascularization or radiation-induced pneumonitis, which might be linked to the low dose parameters for ipsilateral lung, i.e. V5 or V10 (Fagundes et al., 2015; Käsman et al., 2020).

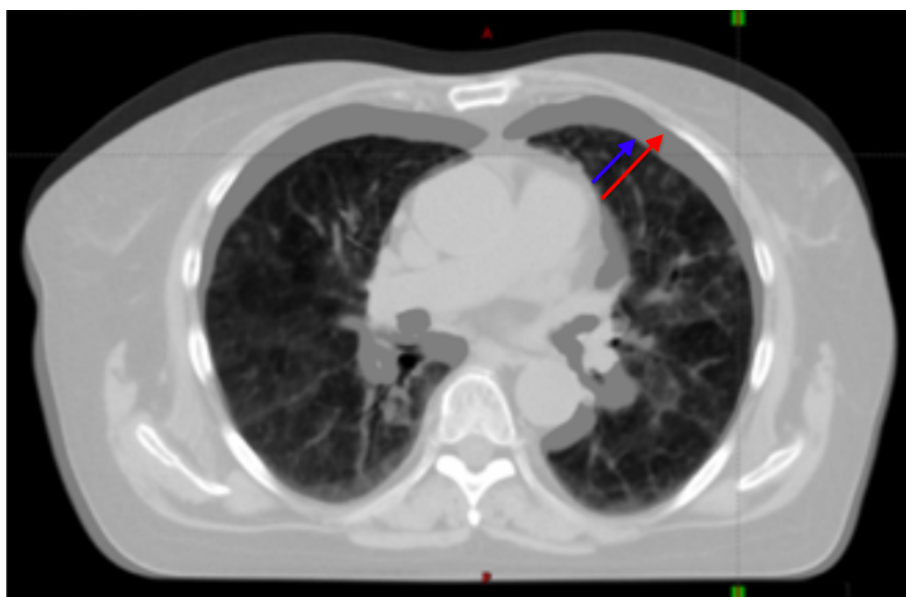


**Figure 22** The difference between free and breath hold anatomy presenting the increased gap between target and cardiac structures; blue arrow marks the distance in FB anatomy and red in BH

According to above mentioned cardiac and lung exposure events, the maximal possible reduction of the dose to normal tissues is of the highest importance in breast cancer radiotherapy. Due to that fact, to obtain best possible dosimetric results, additional techniques have also been introduced to support the processes of treatment planning and delivery. Although breast cancer is not considered a classical 4D indication, it remains under the influence of breathing and requires additional preparations before radiation therapy. To support treatment planning procedures, various motion management modalities can be applied during the course of imaging and treatment to minimize the deteriorating effect of breathing on dose distribution (Knopf et al., 2016; Trnkova et al., 2018; Czerska et al., 2021). Gating or deep inspiration breath hold (DIBH) are techniques which have been widely and successfully used in photon radiotherapy in recent years (Rochet et al., 2015). Both approaches refer to tumor irradiation only during exact motion states, e.g. the maximum breath hold (DIBH), which enables to maximally separate heart and the irradiated breast tissue (Figure 22). This results from the fact that during the breath intake, the heart is pulled posteriorly and inferiorly by the diaphragm, which increases the gap between the target and heart (Taylor & Kirby, 2015). The external, optical devices commonly used for

breath monitoring are, e.g. real time position management (RPM, Varian Medical Systems, Palo Alto, California) or VisionRT systems. Many comparison studies of breast cancer treatments either with or without the DIBH technique, specifically for proton PBS therapy, can be found in the literature (Mast et al., 2014; Patel et al., 2017; Ödén et al., 2017; De Rose et al., 2020).

The influence of breathing and target anatomical placement makes the process of breast cancer treatment planning a complex issue. Usually, for photon radiotherapy two tangential fields are used, with additional supporting fields which can help to increase the dose homogeneity and target coverage (Zhang et al., 2020). With such beam arrangements, the use of DIBH technique allows for further and significant dose reduction to the heart and LAD structure (Bergom et al., 2018). However, when PBS technique is applied, additional factors have to be taken into account due to beam properties and the planning approach has to be reconsidered. It results in different beam arrangement when compared to photons. According to the PTCOG Thoracic Subcommittee consensus guidelines for implementing PBS therapy for thoracic malignancies, the chosen beam direction should be as parallel to the main target motion as possible (Chang et al., 2017). Examples in literature shows the choice of beam angles for PBS breast cancer planning between one beam only (so-called an *en face* beam, as perpendicular as possible to the breast curvature, i.e. main motion direction) (Cunningham et al., 2021; Lin et al., 2015; Chang et al., 2017) and three oblique beams (Mast et al., 2014; Flejmer et al., 2015; Flejmer et al., 2016; Oden et al., 2017). The differences result from the fact that, in case of breast cancer, for certain cases and especially with lymph nodes involvement, the use of one *en face* beam only may not be sufficient to obtain satisfying target coverage due to anatomical challenges. However, as with other radiation modalities, the increase in number of applied beams may lead to higher integral doses to the whole body and the motivation for using more beams should always be clinically justified. The aspect of proper beam angle selection in treatments of moving targets is significant and was one of the topics during the 11<sup>th</sup> 4D Workshop which was held in Krakow, in 2019 and is included in the workshop's review article (Czerska et al., 2021).

Another demanding cancer site, a classical 4D indication, is lung cancer. Various national and international statistics, e.g. International Agency for Research on Cancer (IARC), The Global Cancer Observatory (GCO) and KRN (acronym *from Polish* “Krajowy Rejestr Nowotworów”), present that lung cancer undoubtedly remains the leading cause of cancer death worldwide (18.0% of all cancer deaths) (Sung et al., 2021). Despite the tremendous advances over the last years, not only in radiotherapy but also in surgical procedures, the median survival rate remains very low and according to the American Cancer Society, the 5-year survival rate does not exceed the level of 19% in the United States. Even nowadays, in the era of rapid and efficient development of new treatment modalities, radiotherapy of early stage and locally-advanced non-small cell lung cancer (NSCLC and LA-NSCLC, respectively) has been a challenge, bounded by a high probability of radiation-induced toxicities. These might include, e.g. acute radiation pneumonitis, esophagitis, pulmonary fibrosis or late cardiac toxicities, which significantly affect patients quality of life (Simone, 2017). For inoperable lung cancer cases, radiotherapy or radiotherapy with concurrent chemotherapy have been commonly chosen treatment scenarios, with the advanced photon stereotactic body radiation therapy (SBRT) being a radiotherapy equivalent of surgery. However, in specific cases, when the tumor size and location are very unfavorable and, also with regard to a possible higher risk of failure, alternative radiotherapy options have been taken into account to decrease the possible radiation-associated toxicities. Speaking of proton PBS therapy, which allows for further reduction of radiation doses to critical organs, many research studies have recently evaluated the advantages of the proton technique over photon commonly used SBRT treatment (Register et al., 2011). Remarkable characteristics of protons allow for creating highly conformal dose distribution with safer dose-escalation options, especially when the hypofractionation scheme is taken into account. Protons have shown to be a promising technique in treating NSCLC, LA-NSCLC and other thoracic-located tumors such as, thymic or mesothelioma (Lazarev et al., 2021).

As always, in proton therapy, the key element is the correct patient selection and assignment to the PBS treatment. The literature review shows that up to a certain

motion amplitude and threshold, which needs to be established on a specific center basis (Chang et al., 2017), the NSCLC can be treated with scanned beams with margin and rescanning approaches as motion mitigation solutions. However, to avoid any dose heterogeneities and in the more difficult motion scenarios, additional techniques or their combination might be needed (den Otter et al., 2020).

## **6. Study I: The definition and implementation of a new CT calibration curve**

### **a. Introduction**

The computed tomography (CT) imaging data is predominantly used as a base for radiotherapy contouring and treatment planning purposes. The CT provides necessary information about the anatomy itself and the mass density of tissues, which can be related to the CT numbers expressed in Hounsfield Units (HU) (Malicki & Ślosarek, 2018). The CT calibration curve, a correlation between tissue electron density or relative stopping power (RSP) and HU in photon or proton radiotherapy, is the main CT scanner input data. Based on that conjunction, the information implemented into the TPS provides the corrections for tissues inhomogeneities and determines the dose calculation accuracy. Therefore, the significance of proper scanner-dependent CT curve definition is of the highest importance and might have a huge impact on the treatment planning quality. Important to realize is the fact that a few sources of uncertainties affect the CT curve definition. First are the scanner dependent and specific scanning parameters, including the diameter and photon energy determining the linear attenuation coefficient or the matrix size (Schneider et al., 1996). Secondly, the procedure of curve determination is based on phantoms containing the substitutes for real tissues and especially in the most problematic and challenging areas, e.g. significant inhomogeneities or at the borders of organs of various mass densities, the proper assignment of physical properties is very important. The significance is even higher in proton radiotherapy, where the RSP correlation in tissues with certain HU values might influence the beam range calculations. Together with the proton beam characteristics, the density changes along the beam path might cause the dose differences between 0% and 100%, unlike in photon radiotherapy, where the depth dose distribution decreases almost exponentially. Therefore, the uncertainty of CT calibration curve determination itself is considered at the proton treatment planning stage (the so-called curve calibration error).

Due to the fact that retrospective studies, described in Study II and Study III of this thesis, are based on the imaging data collected with other, than available at CCB IFJ PAN, CT scanner, a dedicated CT curve was prepared and implemented in the Varian Eclipse TPS.

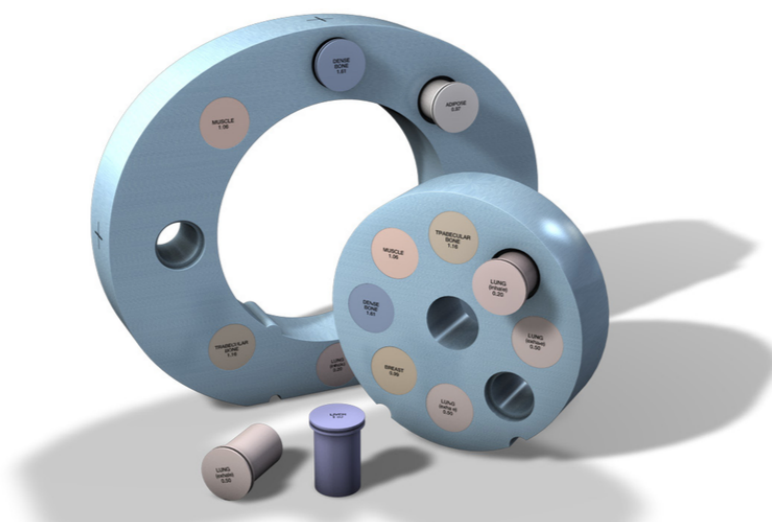


**Figure 23** The CIRS Electron Density Phantom Model 062M (CIRS Electron Density Phantom: Data Sheet)

### **b. Materials and methods**

The first step in establishing the relationship between RSP and CT numbers, expressed in HU, is the CT scan of a dedicated imaging phantom containing various inserts reflecting different human tissues. The CIRS Electron Density Phantom Model 062M, presented in Figure 23, was used in the study for the CT calibration curve definition. The phantom is composed of two so-called nested disks, i.e. head and body, made from the CIRS manufactured *Plastic Water*<sup>®</sup>-LR, specifically dedicated to CT dose verification measurements in the range of 15 keV - 8 MeV. The disks contain 17 holes, which can be replaced with nine different tissue equivalent plugs  $\varnothing 30 \times 50$  mm ( $\varnothing \times L$ ). Additionally, a water-fillable vial is included in the imaging set. The summary of used tissue equivalent plugs is collected in Table 1.

The phantom was scanned with the Thorax 3.0 B31f protocol, 120 kV X-ray tube voltage, 500 mm data collection diameter and 3 mm slice thickness. Subsequently,

based on the acquired CT image (Figure 24), the HU and standard deviation (std) values were derived for all inserted materials and prepared as input data to the *CT\_Calibrate* program (“Program CT\_CALIBRATE. CT calibration curves for proton radiotherapy planning” by Evan A de Kock) (de Kock, 2003). To create the CT curve, the stoichiometric calibration, widely implemented in the proton radiotherapy facilities, which according to the literature, more accurately predicts the HU for human tissues, was executed (Schneider et al., 1996). Performed calculations included informations about the physical density and HU values of the phantom and the densities, and chemical composition of both CIRS manufactured materials and real tissues, based on the literature data and official reports, e.g. ICRU 49, BJR 59 (ICRU 49, 1994; Woodard & White, 1986).

**Table 1** The summary of used tissue equivalent plugs and water-fillable vial for the CT calibration curve, their physical densities and measured both, HU and std values

No.	CIRS Part no.	CIRS material	physical density [g/cc]	HU	std
1	062A-15	Solid Dense Bone (800 mg/cc HA) Equivalent Electron Density Plug	1.530	844.54	20.42
2	062A-04	Lung (Inhale) Equivalent Electron Density Plug	0.205	-769.08	16.19
3	062A-06	Breast (50% Glad / 50% Adipose) Equivalent Electron Density Plug	0.990	-37.76	15.80
4	062A-09	Liver Equivalent Electron Density Plug	1.070	53.10	16.62
5	062A-08	Solid Trabecular Bone (200 mg/cc HA) Equivalent Electron Density Plug	1.160	218.25	17.88
6	062A-05	Lung (Exhale) Equivalent Electron Density Plug	0.507	-490.38	15.16
7	062A-11	Adipose Equivalent Electron Density Plug	0.960	-67.23	16.48
8	062A-10	Muscle Equivalent Electron Density Plug	1.060	46.85	16.20
9	062MA-39	Water-fillable Electron Density Plug	1.000	-3.67	20.78

According to Scheider et al. (1996), to perform the stopping power and radiation length calculations, multiple formulas are used, i.e. the Bragg's additivity rule and Bethe's formula to express the proton stopping power, shell corrections and Rutherford's parametrization to compute the mass attenuation coefficient, including three main interactions of photons with matter, i.e. photoelectric effect, Compton and coherent scattering. Based on these calculations and retrieved data, the Hounsfield Unit value, assigned to a certain CT number and the corresponding material, is defined as:

$$HU = 1000 \left( \frac{\mu_M - \mu_W}{\mu_W} \right) \quad (9)$$

where,  $\mu_M$  - linear attenuation of X-rays in material  $M$ ,  $\mu_W$  - linear attenuation of X-rays in water  $W$  (Malicki & Ślosarek, 2018). Subsequently, the stoichiometric CT curve calibration was based on these informations:

- 1) CT scanner description, proton calibration energy, scanning protocol parameters, reconstruction diameter;
- 2) informations about the densities and chemical composition of both, used tissue equivalent plugs and real human tissues;
- 3) a file containing scanning protocol description with the HU data derived from the acquired CT image for all inserts implemented in the phantom (Table 1).

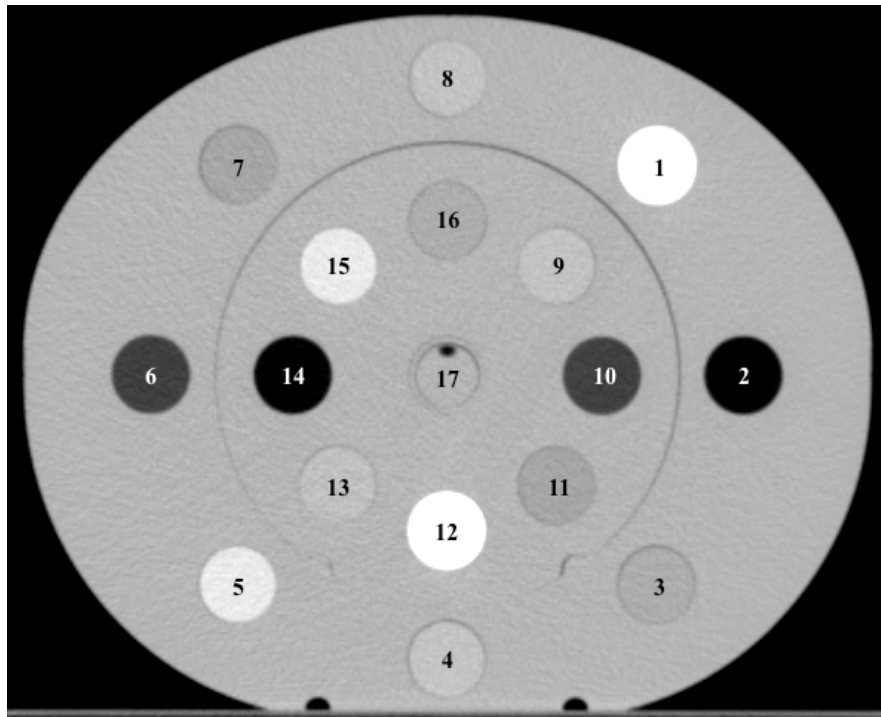


**Figure 24** The CT image of the CIRS Electron Density Phantom Model 062M with 16 tissue equivalent plugs and water-fillable vial; annotations: 1 & 12 - Solid Dense Bone (800 mg/cc HA), 2 & 14 - Lung (Inhale), 3 & 16 - Breast (50% Gland / 50% Adipose), 4 & 9 - Liver, 5 & 15 - Solid Trabecular Bone (200 mg/cc HA), 6 & 10 - Lung (Exhale), 7 & 11 - Adipose, 8 & 13 - Muscle, 17 - water

### c. Results

As a result of the calculations, two output files are generated. One contains the linear and non-linear fit results for the CT numbers, based on the set of the used materials, including results of the least square parametrization method and statistics results. The second file consists of the detailed information on the correlation of 4096 CT numbers (-1000 to 3096) with corresponding relative stopping power and relative radiation length. Based on the in-house procedure of the point selection, subsequently implemented into the Varian Eclipse TPS, the CT calibration curve resulted in 104 CT number points and corresponding RSP values (Figure 25).

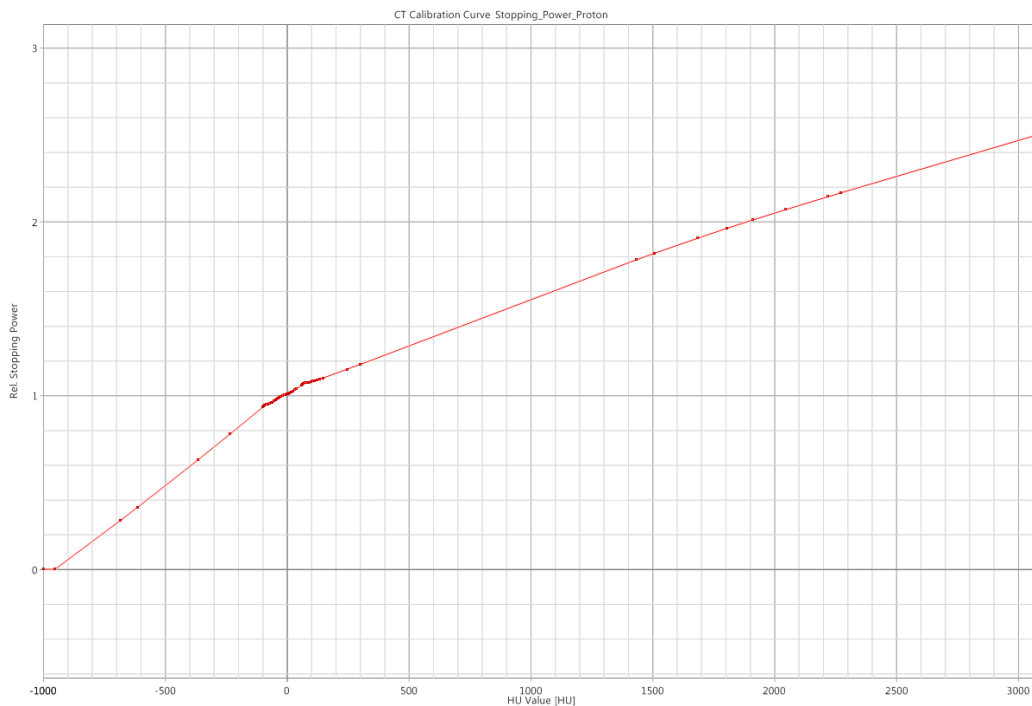


**Figure 25** The new CT calibration curve implemented into the TPS for reference facility

The comparison of two CT calibration curves, the CCB and reference facility, is presented in Figure 26. The differences in HU values  $>1000$  might result from (1) CT scanner calibration and (2) scanning procedure. To prepare the CCB calibration curve, the CIRS phantom was scanned with a 1.5 mm slice thickness, however, 3 mm was used during the scan in the reference facility. Moreover, the CIRS phantom was scanned twice at CCB, with and without the high bone density inserts to avoid the possible artifacts affecting the HU reading based on the acquired CT image. Therefore, it may explain the differences in CT curves, especially in the high HU values area. Nevertheless, the agreement is satisfactory in the most important area of interest (-1000 to 1000 HU).

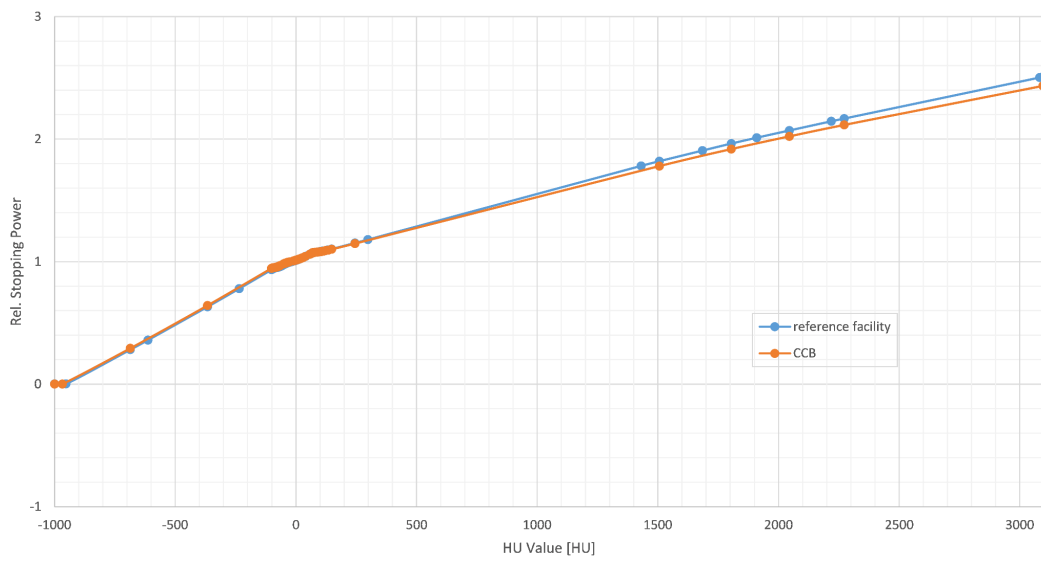


**Figure 26** The comparison of the CT calibration curves for the reference facility and CCB IFJ PAN



## **7. Study II: Proton vs photon radiotherapy of left-sided breast cancer**

### **a. Introduction**

The use of proton radiotherapy to treat deep situated tumors has been available in Poland since 2016, however, the modality is not available to treat all types of cancer and the indication list includes, mainly, head&neck and craniospinal cases. According to the increasing incidence rate for certain cancers, underlined in Chapter 5e and the dosimetric benefits of protons over conventional approaches, there might be an upcoming necessity for re-evaluation of currently dedicated radiotherapy modalities for specific indications in the future. The literature review, also presented in Chapter 4e, including clinical and research studies from the best radiotherapy centers worldwide, indicates that breast cancer is one of the localizations that might specifically profit from proton treatment. Therefore, the main aim of this study was to validate that assumption and evaluate the dosimetric benefit of protons over photon 3D modality using the proton beam model and treatment planning system implemented at the CCB IFJ PAN facility. In detail, the goals can be divided into (1) establishing the possible rationale for using protons in breast cancer treatments as an alternative to conventionally used photon modality in Poland, (2) evaluation of abilities of the IBA and Eclipse TPS systems available at CCB IFJ PAN in terms of breast cancer planning, (3) the dosimetric comparison of proton technique over photon 3D modality according to the literature proton planning and fractionation scheme approaches and (4) further evaluation of the dosimetric impact with the use DIBH technique. It is widely known that breath hold, commonly used in photon radiotherapy, allows for target separation from heart and cardiac substructures, thus impacting the dosimetric outcome. The results in protons are not as straightforwardly translated into the dosimetric gain as they are in photons, which is reflected in the results presented in the sections below.

## b. Materials and methods

The imaging data of 20 consecutive left breast cancer cases, who were treated with the photon DIBH technique, was used in the study. All patients underwent two CT scans dedicated for treatment planning and acquired during free breathing (FB) and breath hold (BH) to further assess the dosimetric advantage of using the DIBH technique over free breathing treatment. The illustrative difference between free and breath hold anatomy is presented in Figure 27. Patients were positioned on the breast board (The AIO Solution, Orfit Industries), in the head first-supine (HPS) position with both arms up, and scanned with Siemens SOMATOM Definition AS CT. The slice thickness was 3 mm and the B31f kernel was used for data reconstruction. The imaging protocol details are presented in Table 2. For breathing monitoring purposes and the acquisition of the BH CT scan, the optical surface imaging system VisionRT (VisionRT Ltd, United Kingdom) was employed. Targets and critical organs were previously delineated by experienced radiation oncologists from the NU-MED Radiotherapy Center in Elbląg, according to the Radiation Therapy Oncology Group (RTOG) guidelines. These cases included the whole left intact breast containing the apparent glandular tissue.

**Table 2** Imaging protocol details used for data collection

<b>Siemens SOMATOM Definition AS</b>	
slice thickness [mm]	3
data collection diameter [mm]	500
voltage [kV]	120
reconstruction filter/convolution kernel	B31f
exposure time [s]	0.5

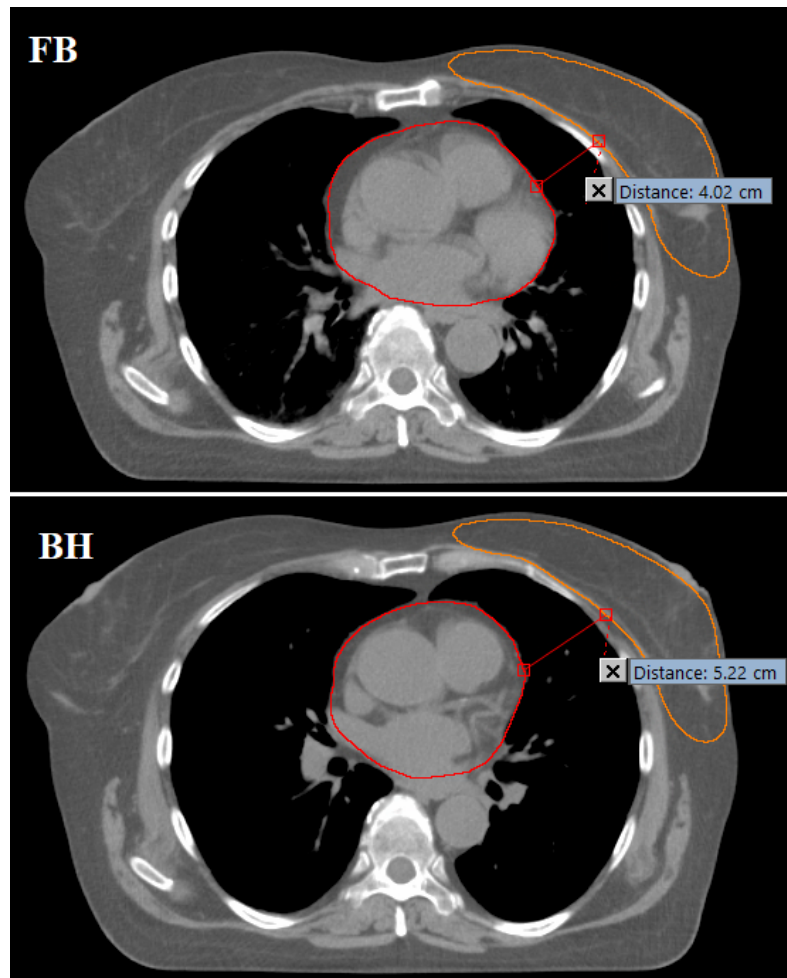


**Figure 27** The comparison of free (FB) and breath hold (BH) anatomies with measured mean distance indicating the increased gap between heart and target due to breath intake

The patient's cohort included a wide variety of anatomies and the CTV target volumes ranged from 345.5 cm<sup>3</sup> to 1333.1 cm<sup>3</sup> for FB and 343.0 cm<sup>3</sup> to 1314.96 cm<sup>3</sup> for BH. The influence of breath hold had a significant influence on the left lung volumes, ranging between 895.8 cm<sup>3</sup> to 1675.0 cm<sup>3</sup> for FB and between 1572.3 cm<sup>3</sup> to 2576.3 cm<sup>3</sup> for BH, which indicates the mean increase of 919.8 cm<sup>3</sup> for all patients.

The dosimetric comparison was based on two treatment planning modalities, i.e. photon 3D and proton IMPT. The photon 3D treatment planning was previously prepared for treatment purposes by experienced medical physicists at the NU-MED Radiotherapy Center in Elblag. The Varian Eclipse TPS version 13.6.30 and the

Anisotropic Analytical Algorithm were used to perform the optimization processes and dose calculations. Treatment plans were prepared according to the general approach used in breast cancer treatments with photon 3D technique, i.e. the application of two tangential, opposing fields of 6 MV energy, with additional supporting fields of lower weights, either 6 or 15 MV energy, to ensure satisfying target coverage and homogeneity. If necessary, the virtual dynamic or mechanical wedges were incorporated into the beam path to improve target dose uniformity and avoid local hot spots. Separate plans were prepared on FB and BH CT scans. All plans were optimized to the PTV volume, which consisted of the CTV target with an additional 7 mm margin to ensure clinically acceptable coverage. Because some of the patients were treated to the prescribed dose of 40.05 Gy in 15 fractions, these plans were recalculated to 50 Gy in 25 fractions for fair comparison.

The proton plans were calculated with the 13.6.32 version of Varian Eclipse TPS system, and according to photon 3D modality, for FB and BH anatomies, respectively. Based on the literature, the beam arrangement included three beams from oblique directions ( $20^\circ$ ,  $60^\circ$  and  $340^\circ$ ) to ensure good coverage and dose homogeneity within the target. The Proton Convolution Superposition (PSC) algorithm was used for dose optimization and calculation. Since the PTV target, created for the photon planning purposes, exceeded the skin surface, which would cause computational problems to proton beams, all plans were optimized to the CTV volume and supporting structure, defined as the CTV minus 3 or 5 mm skin area, depending on the patients' anatomy. The skin was considered a subsidiary area and where possible, the dose was minimized, however, the highest dose objective priority was given to target coverage. Due to the shallow target placement and minimum available energy of 70 MeV at CCB IFJ PAN, which corresponds to the range of  $\sim 4$  cm in water, the range shifter (RS) was placed in the beam path to further decrease the range of the beam. The used range shifter is made of Lexan material of  $1.20 \text{ g/cm}^3$  density, whose chemical composition contains  $H=0.0555$ ,  $C=0.7558$  and  $O=0.1888$  compounds (Shen et al., 2015). The water equivalent thickness (WET) of that RS, in particular, is 4.22 cm. To further support the optimization process and ensure good target coverage, additional proximal, distal and

lateral margins were added to the CTV in Field Properties. The calculation grid was set to 2.0 mm. According to the fractionation scheme found in the literature. The prescribed dose was 50 Gy or 50 Gy(RBE) in 25 fractions in photons and protons, respectively, assuming the relative biological effectiveness (RBE) of 1.1 for protons.

### **c. Results**

The dosimetric comparison of photon and proton plans included dose metrics related to target coverage and radiation burden of critical organs. Because photon plans were optimized to the PTV, for both modalities the CTV target doses were reported as a common thread. According to the clinically accepted and well-known standards, it was assumed that at least 98% of the target volume has to be covered with the isodose of 95% of the prescribed dose ( $V_{98\%}$ ). In more difficult anatomically cases, the coverage of 95% of the volume might also be accepted ( $V_{95\%}$ ). The coverage criteria were obtained in all cases. Moreover, the visual inspection of the plans was conducted to check the dose distribution for any significant inhomogeneities, local hot or cold spots of the dose.

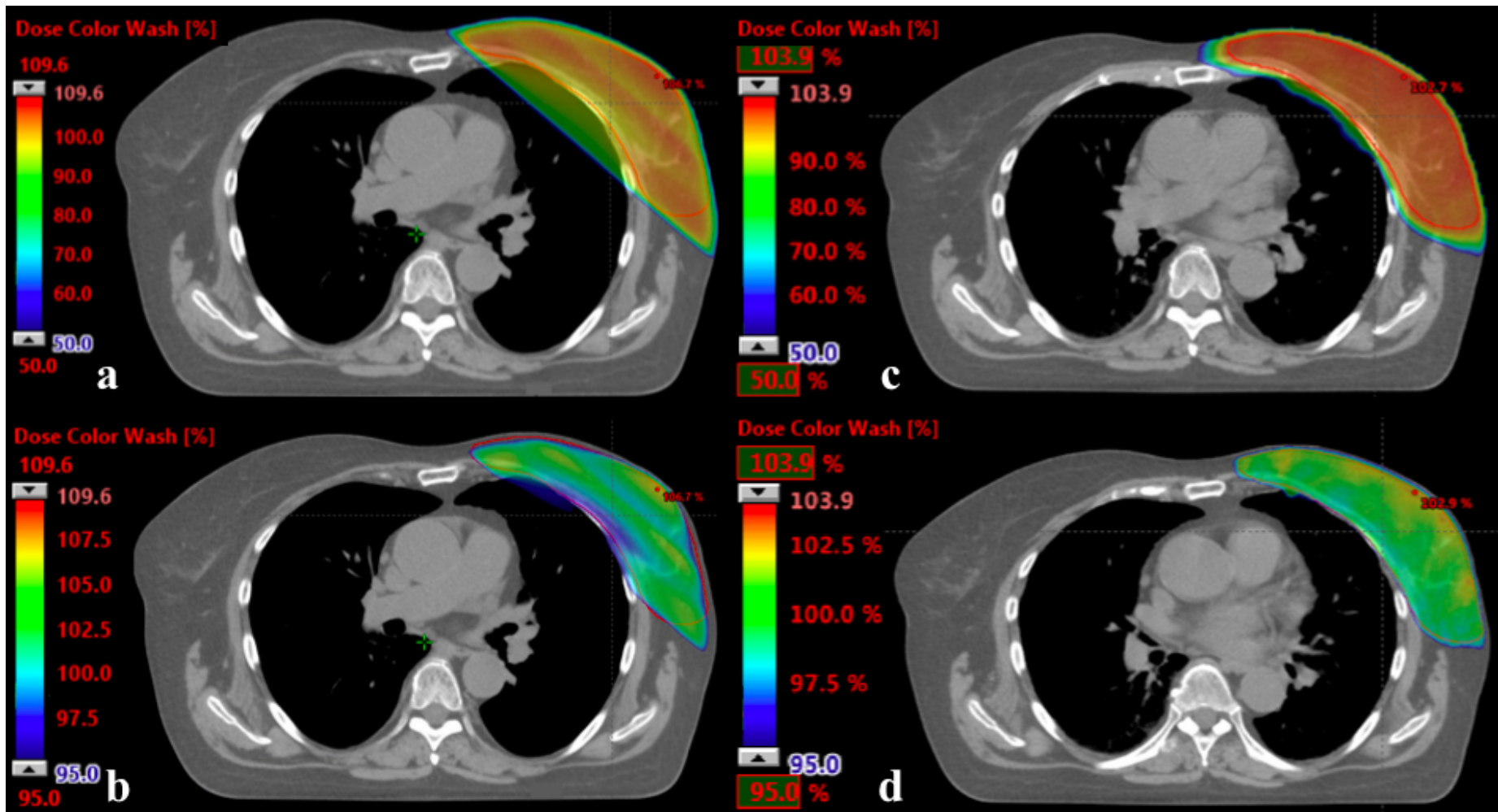


Figure 28 Comparison of 50% (top) and 95% (bottom) isodoses of the prescribed dose for a breath hold photon plan (a and b) and proton free breathing plan (c and d)

Figure 28 compares the dose distribution of 50% and 95% isodoses of the prescribed dose for breath hold photon 3D and free breathing proton IMPT plans, intentionally. Visually, the proton FB plan created a more homogenous area of the high dose region within the target and decreased the radiation burden to the left lung compared to the photon BH plan.

In terms of OARs sparing, the following dose metrics were evaluated, in both photon and proton plans:

1. heart: mean dose in [Gy] or [Gy(RBE)] units for photons and protons, respectively;
2. left lung: mean dose in [Gy] or [Gy(RBE)] units for photons and protons, respectively, and  $V_{20}$  (volume of the left lung receiving either 20 Gy or 20 Gy(RBE) expressed in [%] of the total left lung volume);
3. left anterior descending artery (LAD): mean, maximum and  $D_{\max}0.2 \text{ cm}^3$  doses in [Gy] or [Gy(RBE)] units for photons and protons, respectively. The  $D_{\max}0.2 \text{ cm}^3$  is the dose near maximum received by a small volume of  $0.2 \text{ cm}^3$  of the LAD. Additionally, the results for the  $V_{45}$  metric in [ $\text{cm}^3$ ] units were also reported. The  $V_{45}$  is the volume of the LAD receiving 45 Gy or Gy(RBE) for photons and protons, respectively.

Detailed dosimetric results are presented in Table 3 and Table 4.

**Table 3** Dosimetric comparison of heart and left lung doses obtained in photon and proton plans w/ the DIBH technique;  $D_{\text{mean}}$  - mean dose,  $V_{20}$  - volume receiving 20 Gy or Gy(RBE) for photons and protons, respectively

Patient no.	Target volume [cm <sup>3</sup> ]		Left lung volume [cm <sup>3</sup> ]		HEART				LEFT LUNG							
					$D_{\text{mean}}$				$D_{\text{mean}}$				$V_{20}$			
					photons [Gy]		protons [Gy(RBE)]		photons [Gy]		protons [Gy(RBE)]		photons [%]		protons [%]	
	FB	BH	FB	BH	FB	BH	FB	BH	FB	BH	FB	BH	FB	BH	FB	BH
1	679.3	641.5	1017.3	1904.3	2.8	1.0	0.2	0.0	8.4	7.1	2.7	3.5	14.9	12.0	5.0	6.9
2	678.6	680.7	1607.0	2336.8	3.1	1.4	0.3	0.4	10.3	9.0	4.6	6.6	18.9	15.6	8.3	12.3
3	479.8	459.2	925.7	1699.6	3.4	1.4	1.5	0.5	11.0	9.6	4.9	7.8	19.9	17.0	9.3	15.3
4	415.0	397.4	1304.9	2511.5	2.8	1.2	0.4	0.4	11.6	8.5	5.7	8.1	21.1	15.7	10.7	15.4
5	790.9	804.9	1475.5	2576.3	4.4	1.6	1.3	0.3	9.2	9.3	6.2	7.5	16.4	16.4	12.6	14.9
6	406.8	403.0	1529.9	2149.2	3.8	1.9	0.3	0.3	10.7	9.3	4.3	4.8	20.2	17.4	6.8	8.8
7	513.4	490.7	1204.5	2003.7	13.0	3.5	1.0	0.4	15.6	13.2	6.0	9.5	34.9	29.9	13.1	21.7
8	949.8	913.8	1246.9	2482.0	9.0	3.9	0.5	0.5	14.9	12.0	4.4	7.1	28.0	28.0	8.0	13.2
9	462.6	465.2	1060.4	2114.2	6.9	2.8	0.3	0.3	17.8	10.9	2.6	4.8	40.1	25.4	3.6	8.0
10	1333.1	1315.0	1176.1	2036.2	9.4	6.1	0.3	0.3	9.3	11.0	1.0	6.1	20.1	24.9	0.4	10.5
11	702.9	717.3	928.3	1773.6	9.8	7.1	1.3	0.8	10.1	11.1	5.5	9.9	22.7	25.8	11.1	21.8
12	391.3	365.5	989.8	1899.1	4.2	0.9	0.2	0.2	11.2	8.7	4.2	8.8	21.5	19.0	7.9	18.7
13	652.7	670.9	895.8	1836.2	10.5	7.1	0.1	0.2	15.6	14.7	1.6	5.1	29.6	27.6	2.3	9.4
14	1145.2	1160.1	1076.7	2427.6	6.1	1.5	0.1	0.1	8.5	7.2	1.2	4.5	14.6	14.6	1.1	7.2
15	640.0	635.0	1197.2	2525.6	6.1	1.7	0.9	0.5	12.0	12.1	7.4	9.9	22.3	22.8	16.9	21.8
16	770.3	769.8	1205.6	1886.6	5.1	2.2	0.7	0.5	12.6	8.9	7.5	8.7	24.0	15.8	15.8	16.5
17	903.8	891.0	987.3	1572.3	5.0	2.8	1.0	1.0	9.8	8.2	4.8	8.3	17.1	17.1	9.1	17.4
18	481.3	497.6	1675.0	2372.2	3.8	2.2	0.7	0.8	12.2	9.4	10.8	12.6	23.1	17.3	24.4	28.2
19	444.1	433.4	1095.4	1998.2	9.5	4.7	0.4	0.4	13.4	11.8	6.5	11.2	25.3	22.0	14.3	24.3
20	345.5	343.0	1503.8	2394.6	1.8	1.1	0.5	0.4	9.2	6.5	6.0	7.6	16.8	10.9	12.1	15.2
			<b>mean</b>		<b>6.0</b>	<b>2.8</b>	<b>0.6</b>	<b>0.4</b>	<b>11.7</b>	<b>9.9</b>	<b>4.9</b>	<b>7.6</b>	<b>22.6</b>	<b>19.8</b>	<b>9.6</b>	<b>15.4</b>
			<b>std</b>		<b>3.2</b>	<b>2.0</b>	<b>0.4</b>	<b>0.2</b>	<b>2.6</b>	<b>2.1</b>	<b>2.4</b>	<b>2.4</b>	<b>6.5</b>	<b>5.6</b>	<b>5.8</b>	<b>6.0</b>

**Table 4** Dosimetric comparison of LAD doses obtained in photon and proton plans w/ the DIBH technique;  $D_{\text{mean}}$  - mean dose,  $D_{\text{max}}$  - maximum dose,  $D_{0.2\text{cm}^3}$  - dose received by the 0.2 cm<sup>3</sup> volume of the LAD,  $V_{45}$  - volume receiving 45 Gy or Gy(RBE) for photons or protons, respectively

Patient no.	LAD															
	$D_{\text{mean}}$				$D_{\text{max}}$				$D_{\text{max}0.2 \text{ cm}^3}$				$V_{45}$			
	photons [Gy]		protons [Gy(RBE)]		photons [Gy]		protons [Gy(RBE)]		photons [Gy]		protons [Gy(RBE)]		photons [cm <sup>3</sup> ]		protons [cm <sup>3</sup> ]	
	FB	BH	FB	BH	FB	BH	FB	BH	FB	BH	FB	BH	FB	BH	FB	BH
1	21.5	2.8	0.4	0.1	47.9	4.8	5.9	1.8	36.4	3.7	0.4	0.2	0.1	0.0	0.0	0.0
2	33.0	5.0	2.8	1.3	47.8	16.0	18.1	13.9	46.0	8.4	4.8	3.1	0.4	0.0	0.0	0.0
3	26.3	12.8	8.6	6.6	53.2	42.0	48.0	22.6	52.0	23.0	35.4	11.2	0.6	0.0	0.0	0.0
4	13.5	4.3	1.6	1.1	48.5	18.8	13.6	10.9	32.7	5.9	2.6	1.5	0.0	0.0	0.0	0.0
5	25.1	7.1	12.0	1.3	49.6	33.1	46.8	9.8	48.1	13.7	40.1	3.6	0.6	0.0	0.0	0.0
6	27.0	18.4	6.1	4.3	49.1	45.8	31.0	21.8	48.0	44.2	20.4	13.9	1.3	0.1	0.0	0.0
7	40.2	23.0	7.6	2.7	50.9	48.7	40.6	25.2	50.3	47.7	35.7	11.6	2.5	0.9	0.0	0.0
8	36.4	22.9	3.4	2.1	51.2	47.5	29.4	12.8	50.8	46.6	15.7	5.9	2.4	0.8	0.0	0.0
9	30.8	16.4	1.6	1.2	48.2	47.9	16.3	10.8	48.0	46.4	7.1	4.5	0.4	0.4	0.0	0.0
10	28.1	25.2	1.9	2.8	50.3	48.8	26.1	25.3	49.6	47.9	11.9	11.9	2.1	1.7	0.0	0.0
11	35.5	34.0	9.7	3.3	51.8	51.7	48.4	26.6	51.6	50.5	35.8	15.1	3.8	2.9	0.0	0.0
12	25.5	4.4	2.0	3.4	50.2	20.1	19.0	27.0	49.7	8.3	9.1	10.2	1.6	0.0	0.0	0.0
13	34.7	36.1	1.2	1.1	51.9	50.0	23.0	15.8	51.6	49.2	5.9	3.4	2.1	1.7	0.0	0.0
14	38.6	7.6	0.9	0.4	48.9	33.8	25.3	4.9	48.7	23.3	5.2	1.8	3.5	0.0	0.0	0.0
15	34.8	9.4	12.5	2.3	52.0	39.9	44.7	12.4	51.2	24.7	34.8	7.0	1.8	0.0	0.0	0.0
16	30.2	19.0	5.8	3.1	49.4	49.6	32.1	25.6	49.0	47.9	17.6	9.8	1.1	0.6	0.0	0.0
17	24.4	16.6	5.6	4.3	52.3	39.7	39.8	26.6	50.2	38.4	18.6	13.4	0.8	0.0	0.0	0.0
18	21.8	14.1	3.9	3.1	50.8	46.1	18.7	13.2	48.9	42.0	9.2	8.6	0.8	0.0	0.0	0.0
19	43.3	26.0	5.4	1.9	52.9	52.6	31.1	18.1	52.0	51.6	16.4	7.6	2.1	1.6	0.0	0.0
20	12.5	3.8	5.3	1.1	45.0	11.2	36.1	13.0	35.7	6.5	16.3	4.3	0.0	0.0	0.0	0.0
<b>mean</b>	<b>29.2</b>	<b>15.4</b>	<b>4.9</b>	<b>2.4</b>	<b>50.1</b>	<b>37.4</b>	<b>29.7</b>	<b>16.9</b>	<b>47.5</b>	<b>31.5</b>	<b>17.1</b>	<b>7.4</b>	<b>1.4</b>	<b>0.5</b>	<b>0.0</b>	<b>0.0</b>
<b>std</b>	<b>8.2</b>	<b>10.1</b>	<b>3.6</b>	<b>1.6</b>	<b>2.1</b>	<b>15.0</b>	<b>12.4</b>	<b>7.7</b>	<b>5.7</b>	<b>18.2</b>	<b>12.7</b>	<b>4.5</b>	<b>1.1</b>	<b>0.8</b>	<b>0.0</b>	<b>0.0</b>

The results presented in Table 3 and Table 4 allows for a detailed dosimetric comparison of the doses to OARs, depending on the chosen planning technique and anatomy. Firstly, the differences between proton FB and BH plans were assessed to evaluate the validity of using DIBH in proton treatments. Furthermore, the comparison of proton FB and photon BH plans was conducted because all the patients, which CT datasets were used in that retrospective study, underwent the photon DIBH treatments. The DIBH technique is preferred in photons, when available and suitable for a patient, due to better dosimetric outcome, that is why that specific comparison was of the highest interest and is also presented below.

The  $D_{\text{mean}}$  for heart and both types of proton plans did not exceed the value of 1.5 Gy(RBE), which is the single result for the most demanding anatomy, and the mean calculated for the whole group of 20 patients achieved 0.6 Gy(RBE) and 0.4 Gy(RBE) in FB and BH plans, respectively. These results are satisfactory especially when related to Darby et al. (2013) publication, in which the dose to heart and cardiac substructures is pointed out to be minimized to decrease the risk of ischemic heart disease and late toxicity effects. In comparison to the QUANTEC (Quantitative Analysis of Normal Tissue Effects in the Clinic) guidelines, a document presenting the tolerance that normal tissues have to radiation, mean dose to the pericardium delivered with photons 3D should be below 26 Gy and the thresholds of  $V_{30}<45\%$  and  $V_{25}<10\%$  should not be exceeded to avoid pericarditis following the treatment (Bentzen et al., 2010). The dosimetric results achieved with protons are much lower than those presented by QUANTEC dose constraints. The document, however, does not include any further differentiation of the cardiac substructures, which might play a massive role in the identification of further probability of ischemic heart disease in the future. Thus, the dose to the left anterior descending artery (LAD) should be minimized, carefully analyzed and reported. That is why four additional dose metrics were chosen as suitable indicators of a plan quality in terms of OARs dose minimization, i.e. mean LAD dose, LAD maximum dose,  $D_{\text{max}0.2 \text{ cm}^3}$  and  $V_{45}$ .

The LAD mean doses calculated for the whole group of 20 patients did not exceed 4.9 Gy(RBE) and 2.4 Gy(RBE) for FB and BH plans, respectively, and the LAD

maximum achieved higher results in FB plans when compared to BH (29.0 Gy(RBE) vs. 17.1 Gy(RBE)). The same dependency was seen in the near maximum dose for a very small part of the total LAD volume, i.e. the  $D_{\max}0.2 \text{ cm}^3$ . The mean value calculated for the whole group of 20 patients achieved 17.0 Gy(RBE) and 7.4 Gy(RBE) for FB and BH plans, respectively. Additionally included and verified dose metric in proton plans analysis, which might have significant importance for radiation oncologists using photon treatments, is the  $V_{45}$ , however, that value was rarely overpassed in proton plans and resulted in mean 0.0  $\text{cm}^3$  volumes outcome.

Interesting results were observed for the lung doses in FB and BH plans for proton technique. Higher mean lung doses were observed in the BH cohort, leading to an increased mean result for the whole group, i.e. 7.6 Gy(RBE) (vs. 4.9 Gy(RBE) for FB anatomy). The same relationship was seen in the  $V_{20}$  results, i.e. the percentage of the ipsilateral lung receiving 20 Gy was higher in the BH plans, resulting in the mean outcome of 15.4%, which is significantly higher than the mean 9.6% obtained for the FB cohort.

Based on the above results and the fact that in breast cancer photon treatments in Poland, currently more affordable and available in Poland, is the photon DIBH technique, the photon BH plans were compared to protons planned on FB CT scans for fair comparison. Even though the photon DIBH technique might present excellent dosimetric results in certain cases, the presented comparison resulted in meaningful differences between chosen modalities. The mean heart doses given for the whole group of 20 patients achieved the level of 2.8 Gy for photon BH plans, which was decreased nearly by a factor five in proton FB plans (0.6 Gy(RBE)). Also, the mean LAD dose was decreased by a factor three in proton FB plans, i.e. 4.9 Gy(RBE) vs. 15.4 Gy for photons BH. Proton free breathing plans were also able to significantly minimize the maximum and  $D_{\max}0.2 \text{ cm}^3$  doses to the LAD and the  $V_{45}$ , which was presented in Table 4. Both low lung parameters, the mean dose and  $V_{20}$  Gy, were decreased by a factor two in proton FB plans compared to photon BH, i.e. 4.9 Gy(RBE) vs. 9.9 Gy and 9.6 Gy(RBE) vs. 19.8 Gy for protons and photons, respectively. Figure 29 presents the most

significant dosimetric difference between photon and proton plan resulting in an increasingly higher dose to the left lung area.

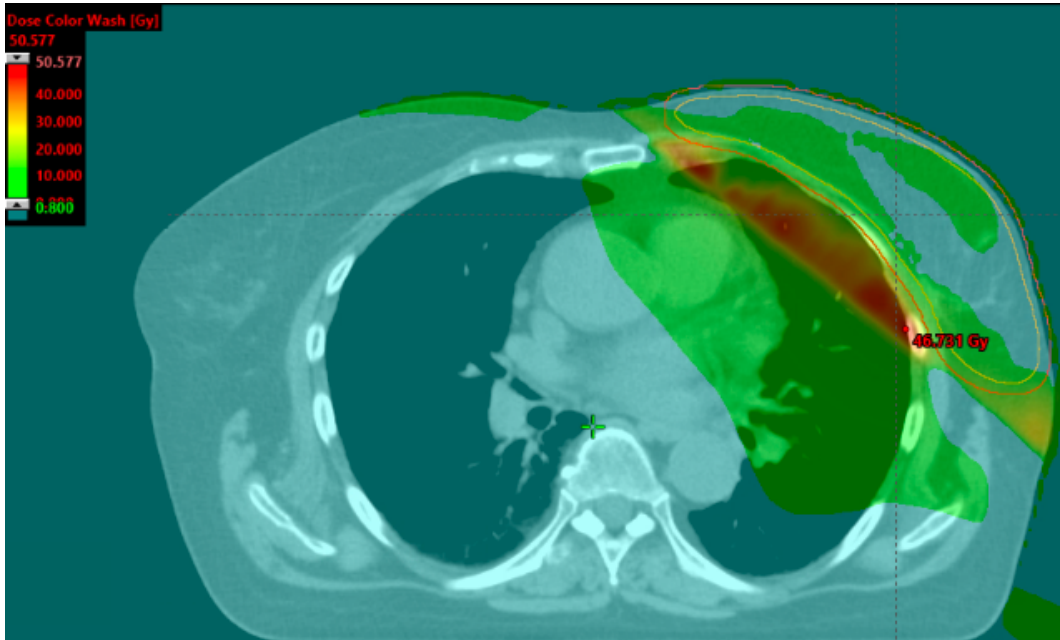


**Figure 29** The dosimetric difference between photon and proton plan; the most significant increase in radiation burden due to the higher dose deposition of a photon plans is seen in the left lung area

Obtained results and differences between modalities show that the proton technique might further reduce an unwanted dose to critical organs in breast cancer treatments, which might be reflected in better local control and minimization of the risk of ischemic heart disease following the treatment. In the presented study, patients CTs presented a wide variety of different anatomies and, despite that fact, the proton plans were superior to photon DIBH in all cases. The main concern when using protons together with the DIBH technique might be the increased dose to the left lung. Nevertheless, even in these cases the dose distribution still presented a better dosimetric outcome than with photons.

## **7. Study III: Significance of beam angle selection in proton radiotherapy of left-sided breast cancer**

### **a. Introduction**

Study III, a continuation of the works presented in Study II focuses on optimizing beam angles and revises the significance of their selection in proton treatment planning for breast cancer to obtain the best dosimetric and robustness results. No existing guidelines for breast cancer proton planning were the main motivation for conducting this study. Presented selection of possible beam arrangements and their impact on treatment plan quality, OARs sparing and the robustness sensitivity to the motion, might be used as a base for choosing the optimal beam selection and planning approach in certain cases. This work presented specifically the selection and optimization of beam angles for five left-sided breast cancer cases with the differentiation to both free (FB) and breath hold (BH) anatomies, and planned with the proton PBS technique. The main goal was to achieve proton treatment plans with clinically acceptable target coverage, minimize cardiac tissues exposure and integral dose, while considering each approach's sensitivity to possible range and setup uncertainties. The significance of using specific beam arrangements on a treatment plan quality was evaluated based on dosimetric differences and statistical analysis between calculated nominal plans. Moreover, their comparison with perturbed plans, representing various uncertainty scenarios, was also conducted as part of a robust 3D evaluation. To our knowledge, the only study using different planning approaches in left-sided breast cancer PBS planning was presented by Flejmer et al. (2017). The group considered the clinical impact of physiological breathing motion on resulting changes in the dose distributions. However, that study did not compare the significance of beam angle selection and optimization for the proton PBS technique in left-sided breast cancer itself. According to published research studies, which are based on a clinical experience or planning comparisons to photon modality, the treatment planning approach for breast cancer and PBS technique differs among centers, which results from

center-specific workflow, equipment and clinical procedures. The differences concern, e.g. prescribed dose, planning technique or a number of used beams and applied angles (Table 5).

**Table 5** Review of treatment planning approaches; NA- not applicable, WB - whole breast, CW - chest wall, PMC - post mastectomy, LPC - lumpectomy, LM - lymph nodes, IMN - internal mammary nodes, FB - free breathing, BH - breath hold, DIBH - deep inspiration BH, BHI - BH at inhalation, BHE - BH at exhalation, SFUD - single field uniform dose, IMPT - intensity modulated proton therapy, RBE - relative biological effectiveness

Publication	Target	L/R-sided	No. of patients	Prescribed dose	Technique (SFUD/IMPT)	No. of beams	Beam angles	Comparison with photons	FB/DIBH
Ares 2010	WB/CW + LN	L	20	50 Gy to PTV	IMPT	3-4	-15°- 75°; -20° -75°	Yes	No
Mast 2014	WB	L	20	42.56 Gy(RBE)/16fx	IMPT	3	345°, 27°, 75°	Yes	FB & DIBH
Lin 2015	WB	L	10	50 Gy(RBE)/25fx	NA	1	en face	Yes	DIBH
Fagundes 2015	CW + LN	L	10	50.4 Gy(RBE)/28fx	NA	NA	NA	Yes	No
Cuaron 2015	CW + LN	L/R	30	45 + 5.4 Gy(RBE)	NA	4	anteriorly oriented	No	No
Flejmer 2015	PMC/LPC	L/R	10	50 Gy(RBE)/25fx	SFUD/IMPT	3	20°, 60°, 340°	No	FB
Flejmer 2016	PMC/LPC	L	20	50 Gy(RBE)/25fx	SFUD/IMPT	3	20°, 60°, 340°	Yes	FB & DIBH
Oden 2017	WB	L	12	50 Gy(RBE)/25fx	IMPT	3	20°, 60°, 340°	Yes	FB & DIBH
Stick 2017	LPC + LM/IMN	L	41	50 Gy(RBE)/25fx	SFUD	2	5°-10°, 50°-60°	Yes	DIBH
Patel 2017	PMC	L	10	50.4/45 Gy(RBE)	IMPT	1	30°	Yes	FB & BH
Flejmer 2017	WB	L	12	50 Gy(RBE)/25fx	SFUD/IMPT	1 or 3	0° or 45° or 20°, 60°, 340°	No	FB & BHI & BHE
Jimenez 2019	WB/CW + LN	L/R/bilateral	69	50.4 Gy(RBE)/28fx	NA	NA	NA	No	No
Raptis 2020	thorax	L	12	50 Gy(RBE)/25fx	IMPT	3	20°, 60°, 340°	Yes	FB (IN/EH)
De Rose 2020	WB/CW	L	20	50 + 10 Gy(RBE)	IMPT	2	45°, 315°	Yes	FB & DIBH
Depauw 2020	PMC	NA	> 25	45 + 5.4 Gy(RBE)	IMPT	1	en face	No	No
Austin 2021	WB	L	16	40 Gy(RBE)/15fx	IMPT	1	en face	Yes	DIBH
Cunningham 2021	WBO/CW + LN	L	16	40.05 Gy(RBE)/15fx	SFUD	1	35°	Yes	DIBH

## b. Materials and methods

The study is based on the CT datasets used in Study II. All the imaging protocol details, targets and organs delineation and patient positioning and the breathing data acquisition are the same as presented in Chapter 6b. Presented cases below include patients no. 1, 2, 5, 7 and 11 from Study I. The chosen beam arrangement included the application of one to three beams from various directions, i.e. an *en face* beam, three sequences of two beams ( $0^\circ$  and *en face* beam, two oblique beams, *en face* beam and  $90^\circ$ ) and three beams from  $20^\circ$ ,  $60^\circ$  and  $340^\circ$  oblique directions, which was presented in Study II. To clarify the use of above-mentioned approaches, the following abbreviations were used: 1B, 2AP, 2PP, 2LAT and 3B, respectively. The same beam arrangements were applied to the BH CT datasets. The visualization of the general rule of choosing beam angles is presented in Figure 30.

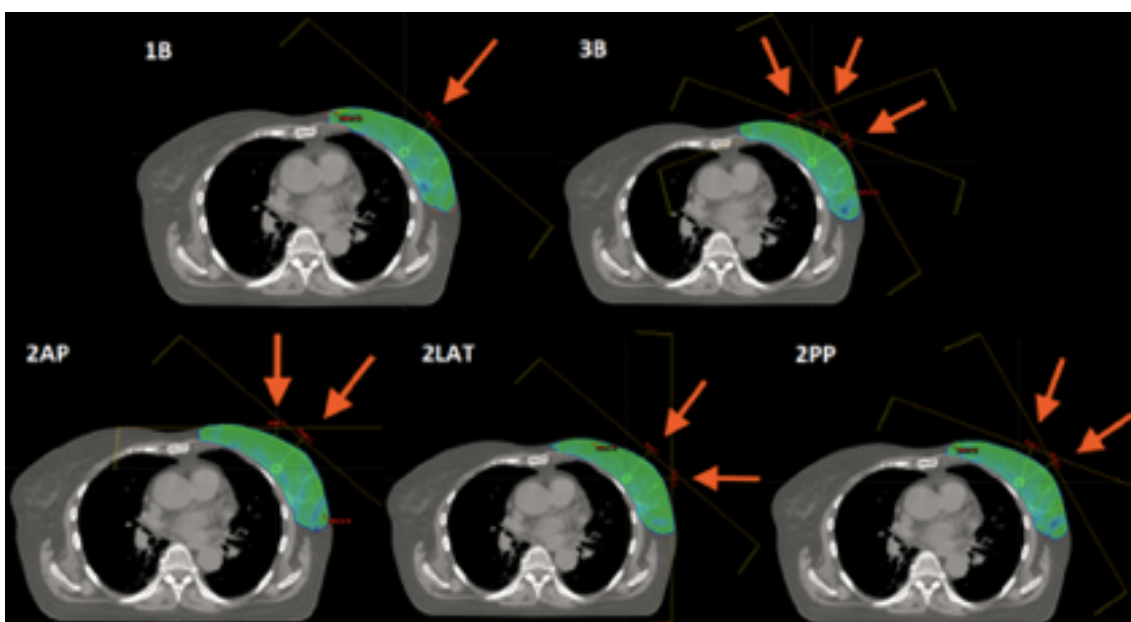


**Figure 30** Visualization of chosen beam arrangements for the study purposes

Applying a certain angle as an *en face* beam was based on choosing the beam direction as perpendicular to the breast curvature as possible, which heavily depends on patients' anatomy and the exact selected beam angle values varied between  $25^\circ$  and  $40^\circ$  (Table 6).

**Table 6** Chosen beam arrangements in Study III

Patient no.	CT scan	1B	2AP	2PP	2LAT	3B
1	FB	40°	0°+40°	20°+60°	40°+90°	20°+60°+340°
	BH	35°	0°+35°	15°+55°	35°+90°	20°+60°+340°
2	FB	30°	0°+30°	10°+50°	30°+90°	20°+60°+340°
	BH	35°	0°+35°	15°+55°	35°+90°	20°+60°+340°
3	FB	30°	0°+30°	10°+50°	30°+90°	20°+60°+340°
	BH	30°	0°+30°	10°+50°	30°+90°	20°+60°+340°
4	FB	25°	0°+25°	10°+50°	25°+90°	20°+60°+340°
	BH	25°	0°+25°	10°+50°	25°+90°	20°+60°+340°
5	FB	25°	0°+25°	5°+45°	25°+90°	20°+60°+340°
	BH	30°	0°+30°	5°+45°	30°+90°	20°+60°+340°

The treatment planning was conducted in the Varian Eclipse TPS version 13.6. Proton Convolution Superposition (PCS) algorithm and the intensity modulated proton technique (IMPT) were used for dose optimization and calculations. All plans were optimized to the CTV volume with additional margins in the Field Properties to insure good target coverage. The accuracy of calculations was increased by setting the calculation grid to 1.5 mm in all cases. The prescribed dose was 50 Gy(RBE) in 25 fractions, which is in accordance with the fractionation schemes found in the literature. The constant relative biological effectiveness (RBE) value of 1.1 was assumed in all calculations. Due to the shallow target placement and range of the energies available at CCB IFJ PAN, the range shifter (RS) was additionally placed in the beam path to decrease the beam energy and allow for covering the proximal part of CTV. The RS characteristic was also presented in Study II of this dissertation. The main criteria during the dose optimization was to create acceptable target coverage and minimize the skin dose, which 5 mm external part was assumed to be a subsidiary area and, where available, was spared. Subsequently, the doses to OARs were minimized as much as possible, but not to deteriorate obtained target coverage. Last step of the treatment planning process was the calculation of the perturbed scenarios, which included the 2

mm setup uncertainty and 3.5% curve calibration error. However, the plans were not robustly optimized due to the used PCS algorithm limitations. The thorough comparison between nominal-worst case and best-worst case scenarios was supported by an in-house developed *TPS\_Histogram\_Analyzer 0.9.0* program and the statistical analysis was conducted using a paired two-tailed Student's t-test and an analysis of variance ANOVA.

### c. Results

To thoroughly assess the dosimetric differences, additional dose metrics had to be introduced to observe the subtle diversities in doses between planning approaches. Moreover, the same dose metrics were reported for all 12 perturbed plans recalculated independently for each of the planning scenarios:

- 1) CTV coverage: the doses received by 98% ( $V_{98\%}$ ) and 95% ( $V_{95\%}$ ) of the CTV volume expressed in [%];
- 2) heart: mean and maximum doses in [Gy(RBE)] units. The low dose heart parameters, i.e.  $V_{10}$  and  $V_5$  are related to the volumes of the heart receiving either 10 or 5 Gy(RBE) expressed in [%] of the total heart volume;
- 3) left lung: mean dose in [Gy(RBE)] units. The low dose left lung parameters, i.e.  $V_{20}$ ,  $V_{10}$ ,  $V_5$  are the volumes of the left lung receiving either 20, 10 or 5 Gy(RBE) expressed in [%] of the total left lung volume;
- 4) left anterior descending artery (LAD): mean, maximum,  $D_{\max 0.2 \text{ cm}^3}$ , and  $D_{10\%}$  and  $D_{5\%}$  doses in [Gy(RBE)] units. The  $D_{\max 0.2 \text{ cm}^3}$  is the dose near maximum received by a small volume of  $0.2 \text{ cm}^3$  of the LAD. The  $D_{10\%}$  and  $D_{5\%}$  are the doses received by 10% or 5% of the total LAD volume expressed in [Gy(RBE)] units.

Target coverage, which was to achieve at least 98% of the CTV covered with the 95% isodose of the prescribed dose, was obtained in all scenarios. However, the lowest coverage values were observed for *en face* beam arrangement in FB and BH resulting in

$V_{98\%}$  of 95.3% and 95.9%, respectively. These differences were statistically significant with regard to other beams selection:

→ p-values for FB plans:

- ◆ 1B vs. 2AP=0.0298
- ◆ 1B vs. 2LAT=0.0234
- ◆ 1B vs. 2PP=0.0031
- ◆ 1B vs. 3B=0.0009

→ p-values for BH plans:

- ◆ 1B vs. 2AP=0.0004
- ◆ 1B vs. 2LAT=0.0002
- ◆ 1B vs. 2AP<0.0001
- ◆ 1B vs. 3B<0.0001

Additional metric validating the plan quality and dose homogeneity within the target was the homogeneity index (HI) calculated according to the ICRU 83 report (ICRU 83, 2010). The highest values were reached in the 1B scenario achieving  $7.2\pm 1.3\%$  in FB and  $7.5\pm 0.7\%$  in BH plans. The results for other beam arrangements prove that HI value decreases with an increasing number of beams, e.g. for 3B scenarios, the HI reaches  $4.1\pm 0.2\%$  in FB and  $4.2\pm 0.2\%$  in BH plans (Table 7). The differences in HI values between FB and BH anatomy were statistically significant (p-value=0.0260), as well as the results between 1B and other beam arrangements:

→ p-values for FB plans:

- ◆ 1B vs. 2AP=0.0005
- ◆ 1B vs. 2LAT<0.0001
- ◆ 1B vs. 2PP=0.0002
- ◆ 1B vs. 3B<0.0001

→ p-values for BH plans:

- ◆ 1B vs. 2AP<0.0001
- ◆ 1B vs. 2LAT<0.0001
- ◆ 1B vs. 2AP<0.0001
- ◆ 1B vs. 3B<0.0001

To evaluate the radiation burden due to the application of a higher number of beams, the integral body, defined as the difference between the whole body structure and the CTV volume was also analyzed (Table 7). The integral body dose defined as the whole body-CTV volume, in 4 out of 5 patient cases achieved the highest values in the 1B beam arrangement and the dosimetric differences between FB and BH were statistically significant (p-value=0.0008). No significant correlation was found with regard to the chosen planning approach. Figure 31 presents the dose distributions for selected beam arrangements and both anatomy scenarios with the 10% isodose of the prescribed dose to present the differences in low dose regions for all cases.

**Table 7** Dosimetric results (mean±one standard deviation) for CTV coverage ( $V_{98\%}$ ,  $V_{95\%}$ ), homogeneity index (HI) and integral body dose with regard to selected beam arrangement

	$V_{98\%}$ [%]		$V_{95\%}$ [%]		HI [%]		Integral body dose [Gy(RBE)]	
	FB	BH	FB	BH	FB	BH	FB	BH
<b>1B</b>	96.9±1.0	96.7±0.6	98.3±0.6	98.3±0.3	7.2±1.3	7.5±0.8	1.3±0.2	1.4±0.3
<b>2AP</b>	98.0±0.4	97.9±0.1	98.7±0.3	98.7±0.1	4.9±0.6	5.1±0.3	1.3±0.2	1.4±0.3
<b>2LAT</b>	98.0±0.5	98.0±0.5	98.7±0.4	98.7±0.3	4.5±0.6	4.7±0.7	1.2±0.2	1.3±0.2
<b>2PP</b>	98.4±0.2	98.2±0.1	99.0±0.2	98.9±0.1	4.7±0.2	4.8±0.2	1.2±0.2	1.4±0.3
<b>3B</b>	98.6±0.3	98.6±0.2	99.0±0.3	99.0±0.1	4.2±0.2	4.2±0.3	1.3±0.2	1.4±0.3

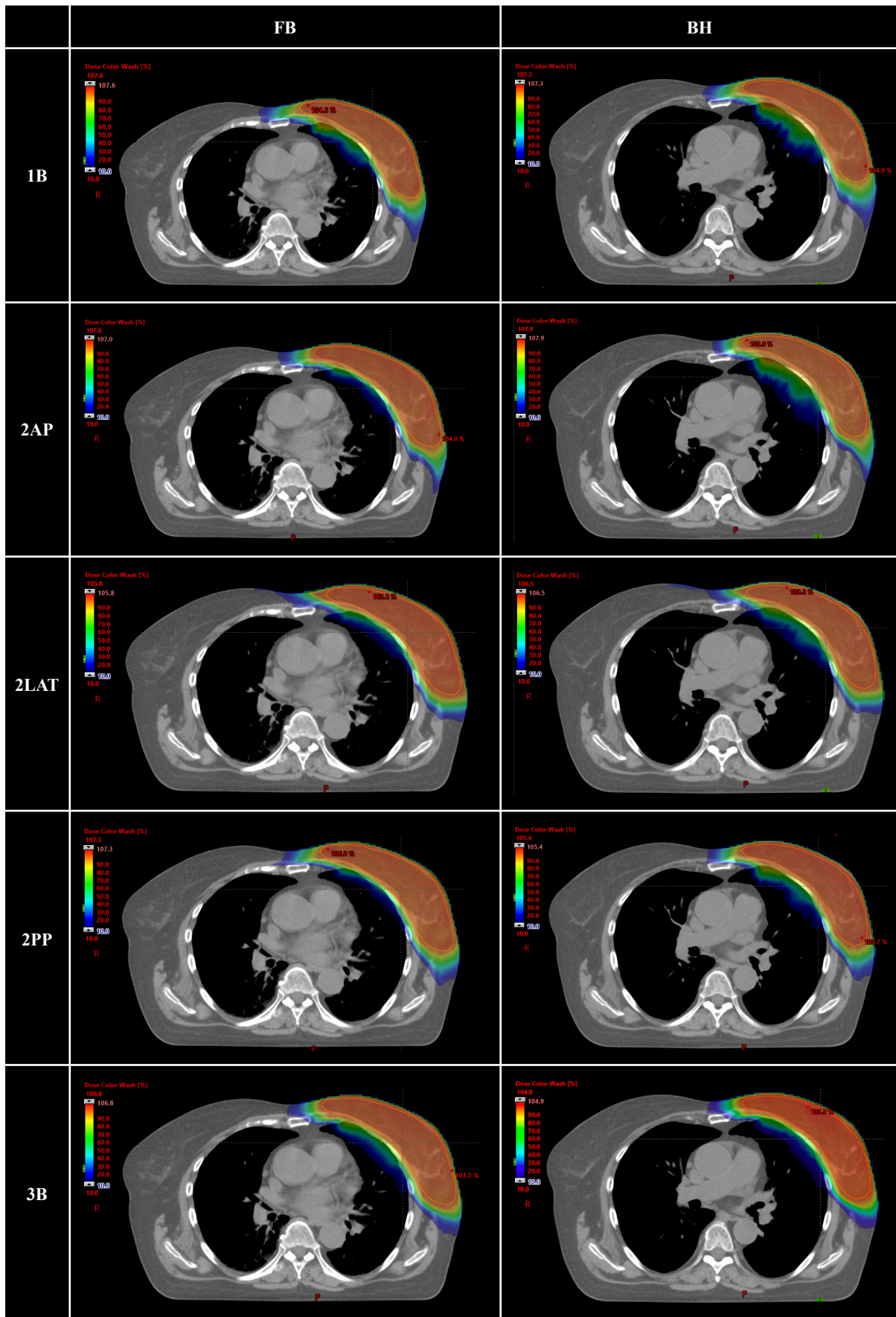


**Figure 31** Dose distributions (10% isodose of the prescribed dose) for all beam arrangements used in the study; abbreviations: 1B (an *en face* beam), 3B (three oblique beams: 20°, 60° and 340°), 2AP (0° and *en face* beam), 2PP (two oblique beams), 2LAT (an *en face* beam and 90°)

The standardly reported OARs dose parameters listed by several guidelines, i.e. QUANTEC and additional metrics, enabling the performance of more detailed dosimetric comparison between planning approaches, are presented in Table 8. The mean heart doses did not exceed  $0.3\pm 0.2$  Gy(RBE) in FB and BH plans. However, the highest results for  $V_{10}$  and  $V_5$  metrics were reported for the 2LAT beam arrangement. Also, the highest differences between doses and the selected beam approach were observed for the  $V_5$ . The 2LAT scenario achieved  $1.7\pm 1.9\%$  and  $1.9\pm 1.6\%$  of the total heart volume for FB and BH, respectively, which also means that the low heart doses were increased for BH anatomy. Additionally, the maximum dose to the heart was also evaluated, with the highest results obtained in 1B arrangement, both FB and BH. The analysis of all heart dose metrics showed no statistical significance between certain planning approaches and differences between FB and BH were negligible. The mean and low dose parameters to the left lung, calculated for the whole group of five patients, showed no clear correlation between the results and chosen beam scenario, and were not statistically significant. However, all metrics resulted in higher values for BH plans, which is consistent with observations in Study II and these differences were statistically significant (FB vs. BH, p-values:  $D_{\text{mean}} < 0.0001$ ,  $V_{20} = 0.0054$ ,  $V_{10} = 0.0017$ ,  $V_5 = 0.0008$ ). Moreover, to expand the analysis for cardiac substructures, the whole set of various LAD doses was prepared for detailed comparison due to the unique structure characteristics. The mean,  $D_{\text{max}0.2 \text{ cm}^2}$  and  $D_{10\%}$  doses achieved the highest values in the 2LAT beam scenario and the  $D_{5\%}$  outcome was the worst either in 2LAT or 1B arrangement. Also, the comparison between FB and BH plans regarding cardiac substructures burden showed an increase in BH plans, however, these results were not statistically significant when compared between different beam arrangements.

In accordance with proton treatment planning, a standard part of the plan preparation is the performance of either robust 3D planning or robust 3D evaluation. Due to the chosen algorithm for optimization, the PCS available in the Varian Eclipse TPS, the plans were not robustly 3D optimized. Still, they included additional margins, which allowed for a partial minimization of the deteriorating factors. Thus, for each beam scenario, a corresponding set of perturbed plans was recalculated for 2 mm setup

and 3.5% curve calibration uncertainties, resulting in 12 additional dosimetric scenarios. Due to the fact that the level of doses obtained with protons for selected OARs was already at a low and clinically reasonable level, an even more restricted analysis was performed in the robustness 3D analysis. The quality of each beam arrangement was assessed based on several additional dose metrics and derived data from the dose-volume histograms (DVHs) for the perturbed scenarios. Moreover, every chosen metric was compared between nominal-best and nominal-worst robust scenarios, and between best and worst robust scenarios as well.

**Table 8** Dosimetric results (mean±one standard deviation) for left lung, heart and LAD, with regard to selected beam arrangement;  $D_{\text{mean}}$  - mean dose,  $D_{0.2\text{cm}^3}$  - dose received by the 0.2 cm<sup>3</sup> volume of the LAD,  $D_{\text{max}}$  - maximum dose,  $V_{20}/V_{10}/V_5$  - volumes receiving 20/10/5 Gy(RBE), respectively and  $D_{10\%}/D_{5\%}$  - doses received by 10%/5% of the volume, respectively

IPSILATERAL LUNG								
	$D_{\text{mean}}$ [Gy(RBE)]		$V_{20}$ [%]		$V_{10}$ [%]		$V_5$ [%]	
	FB	BH	FB	BH	FB	BH	FB	BH
<b>1B</b>	2.8±1.2	4.1±1.1	4.5±3.1	7.2±2.9	10.7±4.8	15.7±4.7	16.1±6.5	23.0±6.1
<b>2AP</b>	2.8±1.2	4.4±1.2	2.7±1.9	6.0±2.6	10.3±4.9	16.6±5.3	18.6±8.6	27.3±8.6
<b>2LAT</b>	2.4±1.1	3.1±0.8	2.8±2.4	3.9±1.8	9.1±4.4	11.8±2.8	15.2±6.1	19.6±5.6
<b>2PP</b>	2.4±1.1	3.9±1.0	2.1±1.7	4.7±1.2	8.6±4.7	14.4±3.8	16.3±7.8	24.3±7.4
<b>3B</b>	3.1±1.2	4.1±1.5	4.0±2.6	5.4±2.6	11.7±5.0	15.8±6.2	19.1±7.1	25.3±9.1
HEART								
	$D_{\text{mean}}$ [Gy(RBE)]		$D_{\text{max}}$ [Gy(RBE)]		$V_{10}$ [%]		$V_5$ [%]	
	FB	BH	FB	BH	FB	BH	FB	BH
<b>1B</b>	0.2±0.2	0.2±0.2	25.3±9.3	26.3±8.1	0.4±0.6	0.6±0.6	1.2±1.1	1.5±1.3
<b>2AP</b>	0.2±0.1	0.1±0.1	20.6±8.3	17.0±5.4	0.2±0.4	0.2±0.3	0.8±0.8	0.8±0.9
<b>2LAT</b>	0.3±0.2	0.3±0.2	23.5±8.2	23.5±9.7	0.5±0.7	0.7±0.7	1.7±1.9	1.9±1.6
<b>2PP</b>	0.1±0.1	0.2±0.1	20.5±10.5	19.4±7.1	0.2±0.5	0.3±0.2	0.7±0.9	0.9±0.6
<b>3B</b>	0.2±0.1	0.1±0.1	21.4±8.5	14.1±4.9	0.2±0.3	0.1±0.1	0.8±0.6	0.6±0.4
LEFT ANTERIOR DESCENDING ARTERY								
	$D_{\text{mean}}$ [Gy(RBE)]		$D_{0.2\text{cm}^3}$ [Gy(RBE)]		$D_{10\%}$ [Gy(RBE)]		$D_{5\%}$ [Gy(RBE)]	
	FB	BH	FB	BH	FB	BH	FB	BH
<b>1B</b>	1.8±1.3	2.4±3.2	4.2±3.6	5.6±6.9	4.9±3.4	5.9±7.2	6.6±4.3	7.1±7.9
<b>2AP</b>	1.1±1.0	1.7±2.5	2.9±3.1	3.8±4.8	3.2±2.9	4.0±5.2	4.2±3.7	4.8±5.9
<b>2LAT</b>	2.4±1.7	2.6±3.1	5.5±4.4	5.7±6.1	6.1±4.3	6.2±7.0	7.4±5.3	7.0±7.8
<b>2PP</b>	1.1±1.0	1.1±1.2	2.8±3.1	2.8±3.2	3.0±2.8	3.0±3.1	4.2±3.8	3.7±3.5
<b>3B</b>	1.2±0.7	1.2±1.3	3.1±2.7	2.7±2.9	3.3±2.1	2.8±2.8	4.6±3.0	3.5±3.3

The CTV robustness evaluation resulted in the highest discrepancies for 1B beam arrangement in terms of the  $D_{98\%}$  differences between nominal and worst case scenarios (Table 9). These differences are seen in both, FB and BH plans:

→ p-values for FB plans:

- ◆ 1B vs. 2AP=0.0006
- ◆ 1B vs. 2LAT=0.0022
- ◆ 1B vs. 2PP=0.0001
- ◆ 1B vs. 3B=0.0006

→ p-values for BH plans:

- ◆ 1B vs. 2AP<0.0001
- ◆ 1B vs. 2LAT<0.0001
- ◆ 1B vs. 2AP<0.0001
- ◆ 1B vs. 3B<0.0001

**Table 9** Dosimetric results (mean±one standard deviation) for CTV with regard to selected beam arrangement;  $D_{98\%}$  - dose received by 98% of the CTV volume

CTV	$D_{98\%}$ [Gy(RBE)]			
	nominal-worst		best-worst	
	FB	BH	FB	BH
<b>1B</b>	0.5±0.1	0.5±0.1	2.0±0.4	2.2±0.2
<b>2AP</b>	0.1±0.1	0.1±0.0	1.9±0.5	2.0±0.2
<b>2LAT</b>	0.2±0.1	0.1±0.1	1.8±0.5	1.7±0.2
<b>2PP</b>	0.1±0.0	0.1±0.0	1.4±0.3	1.5±0.3
<b>3B</b>	0.1±0.1	0.2±0.1	1.8±0.3	1.9±0.2

On the other hand, the differences between maximum or near-maximum doses, i.e.  $D_{max}$ ,  $D_{5\%}$  and  $D_{2\%}$  showed that the *en face* beam arrangement was the least sensitive with regard to the chosen robustness variables between nominal and perturbed scenarios, e.g. for  $D_{2\%}$ :

→ p-values for FB plans:

- ◆ 1B vs. 2AP=0.0046
- ◆ 1B vs. 2LAT<0.0001
- ◆ 1B vs. 2PP=0.0127
- ◆ 1B vs. 3B<0.0001

→ p-values for BH plans:

- ◆ 1B vs. 2AP=0.0002
- ◆ 1B vs. 2LAT<0.0001
- ◆ 1B vs. 2AP=0.0031
- ◆ 1B vs. 3B<0.0001

The discrepancies between best and worst cases were also minimized in the 1B beam selection, which applied to both FB and BH plans. The significantly worst dosimetric outcome with regard to near-maximum doses, i.e. the  $D_{5\%}$  and  $D_{2\%}$  analyzed, was achieved in the 2LAT arrangement and FB anatomy with the same observation for BH anatomies. However, here 3 out of 5 worst results were achieved in the 2LAT arrangement and 2 out of 5 in the 3B scenario. The results are presented in Table 10.

The robustness 3D analysis for OARs included more dose parameters evaluated between nominal-worst and best-worst scenarios, i.e.  $D_{5\%}$ ,  $D_{10\%}$ ,  $D_{20\%}$ ,  $D_{30\%}$ ,  $D_{40\%}$ ,  $D_{50\%}$  and maximum doses, to have a thorough insight into the plan quality based on chosen beam arrangement. There was no clear correlation between worst dosimetric results and selected beam angles regarding the left lung doses, regardless of the anatomy. However, in the case of heart, the  $D_{5\%}$ ,  $D_{10\%}$  and  $D_{20\%}$  comparison of nominal-worst and best-worst scenarios reached the highest values for the 2LAT arrangement in all patients (Table 11). The analysis of low doses to the LAD, i.e.  $D_{5\%}$  and  $D_{10\%}$  presented that, in 4 out of 5 patient cases, the worst nominal-worst and best-worst scenario results were obtained in the 1B arrangement. There was no clear correlation though in the results for  $D_{20\%}$ ,  $D_{30\%}$ ,  $D_{50\%}$  or maximum doses and certain planning approaches.

**Table 10** Dosimetric results (mean±one standard deviation) for CTV with regard to selected beam arrangement;  $D_{5\%}/D_{2\%}$  - dose received by 5%/2% of the CTV volume

CTV	$D_{5\%}$ [Gy(RBE)]				$D_{2\%}$ [Gy(RBE)]			
	nominal-worst		best-worst		nominal-worst		best-worst	
	FB	BH	FB	BH	FB	BH	FB	BH
<b>1B</b>	0.1±0.0	0.1±0.0	0.2±0.0	0.2±0.0	0.1±0.0	0.1±0.0	0.3±0.0	0.2±0.0
<b>2AP</b>	0.4±0.1	0.5±0.1	0.5±0.1	0.5±0.1	0.8±0.2	0.9±0.2	0.9±0.2	1.0±0.2
<b>2LAT</b>	1.6±0.5	1.2±0.4	1.7±0.4	1.3±0.4	1.8±0.6	1.4±0.4	1.8±0.5	1.4±0.4
<b>2PP</b>	0.6±0.1	0.6±0.2	0.7±0.2	0.7±0.2	0.8±0.1	0.7±0.2	0.9±0.1	0.8±0.2
<b>3B</b>	1.0±0.2	1.0±0.1	1.1±0.3	1.2±0.3	1.2±0.1	1.3±0.1	1.3±0.2	1.4±0.2

To conclude, the main aim of that study was to evaluate the impact and importance of beam angle selection in proton PBS breast cancer treatment planning. Five beam arrangements were applied to FB and BH anatomies, varying from one to three beams from oblique directions to create a highly homogeneous dose distribution within the target, while maximally sparing OARs. However, the characteristics of proton beams interactions with matter require a more advanced and careful approach to planning the treatment than other modalities. Therefore, it is vital to evaluate the impact of any density changes that might occur in the beam path during the single fraction and due to the motion action. To assess each plan sensitivity to the prescribed perturbations and their impact on treatment plan quality, a robust 3D analysis was conducted after all plan optimization and calculation. The results show that with all beam arrangements it is possible to obtain clinically acceptable treatment plans with dose levels significantly decreased with regard to the reported doses for photon technique. However, the thorough analysis of the dose distribution within the patient, not only the target, is necessary to evaluate the possible deteriorating impact on surrounding healthy tissues to minimize the risk of secondary cancers in the future. The robustness analysis showed a few important messages regarding the applied beam arrangement. The worst dosimetric outcome was obtained with the 2LAT scenario, which includes, apart from the use of an oblique beam, also a laterally directed beam. That approach had the worst OARs results. Also, the low lung and cardiac parameters showed significantly increased low dose region, which might be crucial in minimizing the toxicity effects. Another concern employing the 2LAT scenario was the additional dose to the contralateral breast, which should be avoided. The selection of one beam only, commonly used in many centers worldwide, might also increase the doses to surrounding tissues in certain cases, which might be successfully minimized with other approaches.

**Table 11** Dosimetric results (mean±one standard deviation) for left lung, heart and LAD, with regard to selected beam arrangement;  $D_{10\%}/D_{5\%}$  - doses received by 10%/5% of the volume, respectively

<b>IPSILATERAL LUNG</b>								
	<b><math>D_{10\%}</math> [Gy(RBE)]</b>				<b><math>D_{5\%}</math> [Gy(RBE)]</b>			
	<b>nominal-worst</b>		<b>best-worst</b>		<b>nominal-worst</b>		<b>best-worst</b>	
	<b>FB</b>	<b>BH</b>	<b>FB</b>	<b>BH</b>	<b>FB</b>	<b>BH</b>	<b>FB</b>	<b>BH</b>
<b>1B</b>	7.5±1.5	7.2±0.6	12.6±3.7	13.1±1.1	9.0±1.1	7.5±0.5	16.6±1.7	14.6±1.3
<b>2AP</b>	6.6±2.1	7.1±0.3	11.0±3.8	12.8±0.8	8.4±0.9	7.6±0.5	14.8±2.3	14.4±1.0
<b>2LAT</b>	6.1±1.9	6.5±0.9	10.0±3.7	11.0±1.9	7.8±0.8	8.1±0.6	13.6±2.3	14.5±1.3
<b>2PP</b>	6.0±1.9	6.4±0.5	9.8±3.6	11.3±1.2	7.8±1.0	7.6±0.8	13.3±2.4	14.0±1.0
<b>3B</b>	6.4±1.2	6.2±1.1	10.9±2.6	11.0±2.4	8.1±0.9	7.2±0.3	14.6±1.3	13.1±0.8
<b>HEART</b>								
	<b><math>D_{10\%}</math> [Gy(RBE)]</b>				<b><math>D_{5\%}</math> [Gy(RBE)]</b>			
	<b>nominal-worst</b>		<b>best-worst</b>		<b>nominal-worst</b>		<b>best-worst</b>	
	<b>FB</b>	<b>BH</b>	<b>FB</b>	<b>BH</b>	<b>FB</b>	<b>BH</b>	<b>FB</b>	<b>BH</b>
<b>1B</b>	0.2±0.4	0.3±0.4	0.3±0.5	0.4±0.6	1.2±1.1	1.1±1.1	1.7±1.7	1.6±1.8
<b>2AP</b>	0.2±0.3	0.1±0.2	0.3±0.5	0.2±0.4	0.9±0.9	0.6±0.7	1.2±1.4	1.0±1.2
<b>2LAT</b>	0.6±0.6	0.6±0.5	0.9±0.9	0.9±0.8	1.5±0.9	1.3±0.9	2.5±1.6	2.2±1.5
<b>2PP</b>	0.2±0.3	0.2±0.2	0.2±0.4	0.2±0.3	0.7±0.8	0.8±0.6	1.0±1.2	1.2±0.9
<b>3B</b>	0.2±0.2	0.2±0.2	0.2±0.3	0.3±0.3	0.8±0.5	0.8±0.5	1.1±0.8	1.2±0.8
<b>LEFT ANTERIOR DESCENDING ARTERY</b>								
	<b><math>D_{10\%}</math> [Gy(RBE)]</b>				<b><math>D_{5\%}</math> [Gy(RBE)]</b>			
	<b>nominal-worst</b>		<b>best-worst</b>		<b>nominal-worst</b>		<b>best-worst</b>	
	<b>FB</b>	<b>BH</b>	<b>FB</b>	<b>BH</b>	<b>FB</b>	<b>BH</b>	<b>FB</b>	<b>BH</b>
<b>1B</b>	5.4±2.4	3.8±2.6	8.3±4.1	6.2±4.9	6.2±2.3	4.4±2.3	9.7±4.2	7.1±4.6
<b>2AP</b>	3.7±2.0	2.8±2.3	5.4±3.3	4.5±4.2	4.4±1.9	3.3±2.4	6.5±3.4	5.2±4.3
<b>2LAT</b>	4.1±1.5	2.7±1.7	6.4±2.5	4.6±3.1	4.6±1.6	2.9±1.6	7.2±2.7	4.9±3.1
<b>2PP</b>	3.7±2.4	2.8±2.0	5.4±3.8	4.3±3.4	4.3±2.6	3.5±2.2	6.5±4.2	5.3±3.6
<b>3B</b>	3.7±1.8	2.3±1.7	5.5±2.8	3.5±2.8	3.7±2.1	2.8±1.9	5.2±3.7	4.3±3.2

## 8. Study IV: Proton radiotherapy of lung cancer

### a. Introduction

To enable treatments of moving targets at any radiotherapy facility, many steps have to be taken before implementing the treatments in clinics. In the case of proton beams, special attention has to be paid to the beam range and delivery accuracy, the preparation phase takes much longer due to the expanded workload and the range of needed testing. The motivation for conducting this work was to verify the clinically available tools and capabilities of both the Varian Eclipse TPS and IBA systems, available at Cyclotron Centre Bronowice IFJ PAN, to enable the possible treatments of moving targets in the future. The main goal was to perform the time-resolved imaging, treatment planning and test the delivery capabilities together with dosimetry solutions for lung cancer, imitated by a CIRS Dynamic Thorax Motion Phantom for the study purposes (Figure 32). Each of these phases needed multiple verification steps, which will be presented below in three parts, i.e. 4D imaging and contouring, treatment planning (with or without the robust 3D optimization) and delivery/dosimetry testing.

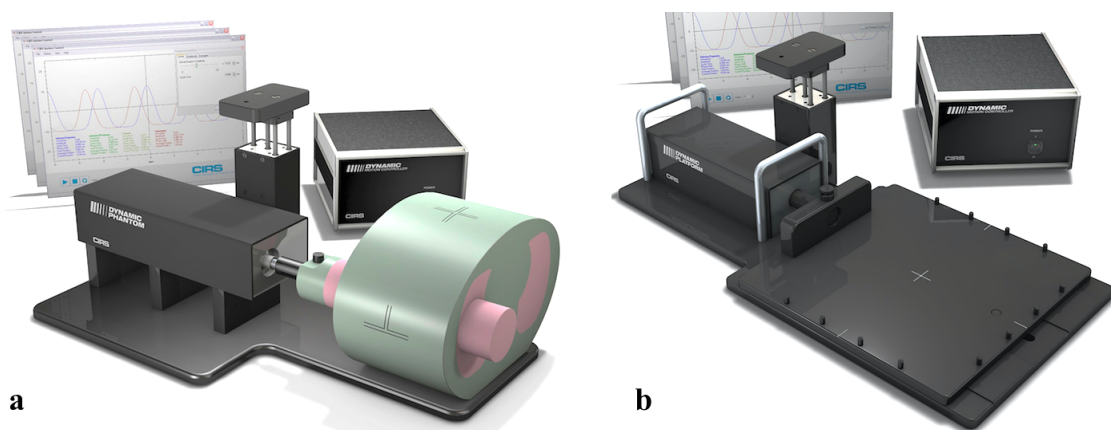


**Figure 32** The CIRS Dynamic Thorax Motion Phantom (a) and the CIRS Dynamic Platform (b) (CIRS Dynamic Thorax Phantom: Brochure, CIRS Dynamic Platform: Brochure)

## b. 4D imaging, treatment planning and robust 4D optimization

### i. Materials and methods

The CIRS Dynamic Thorax Motion Phantom represents an average human thorax made of tissue equivalent materials with interchangeable inserts dedicated to quality assurance, imaging and dosimetry. The phantom body mimics simplified patient geometry and is made of CIRS tissue equivalent epoxy materials, whose linear attenuation coefficients of simulated real tissues are within 1% and 3% (energy range 0.05-15 MeV) tolerance with relation to water/bone and lung, respectively. Additionally, the phantom contains a three-dimensional anthropomorphic spine representing cortical and trabecular bones, and external surface landmarks for phantom positioning along with lasers. Estimated CIRS materials properties, reproduced from CIRS Dynamic Motion Thorax Brochure and given by the producer, are presented in Table 12.

**Table 12** CIRS materials properties reproduced from CIRS Dynamic Motion Thorax Brochure (CIRS Dynamic Motion Thorax Brochure)

Material	Density [g/cc]	Electron Density [ $\times 10^{23}/\text{cc}$ ]	Ratio to H <sub>2</sub> O
Plastic Water® DT	1.04	3.35	1.003
Lung	0.21	0.69	0.207
Cortical Bone	1.91	5.95	1.782
Trabecular Bone	1.20	3.86	1.156
Soft tissue target	1.06	3.43	1.028

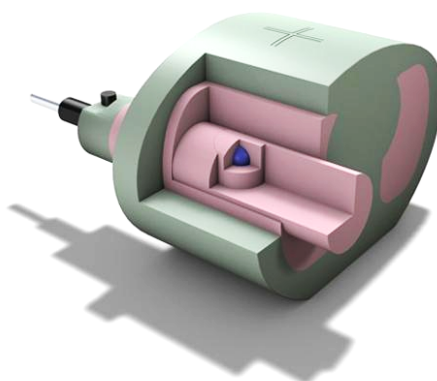


**Figure 33** The cut away view of the CIRS Dynamic Thorax Motion Phantom depicting the soft tissue target inside the phantom (CIRS Dynamic Thorax Motion Phantom Brochure)

The phantom set contains various interchangeable inserts of 6.35 cm diameter, made of lung equivalent epoxy and with density matching the surrounding lung lobe, making it radiographically invisible during imaging. The body is connected to a motion actuator and a controller, which together with the Motion Control Software manage the rod motion in three dimensions inside the phantom. The maximum available peak-to-peak amplitude is 50 mm in superior-inferior (S-I) direction via translations, 10 mm in anterior-posterior (A-P) and 5 mm in lateral (LAT) directions via rotations. There are a few programmed motion waveforms, which can be chosen in the Motion Control software, e.g.  $\sin(t)$ ,  $1-2\cos^4(t)$ ,  $1-2\cos^6(t)$ , sawtooth or sharkfin. Figure 33 presents the cut away view of the phantom consisting of the blue soft tissue imaging target.

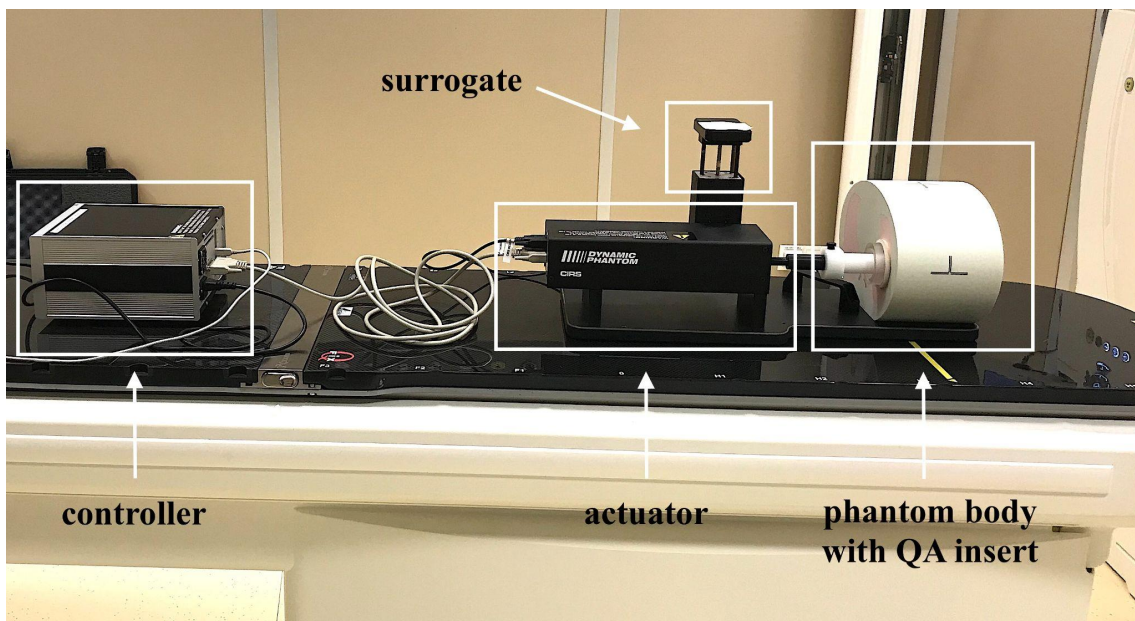


**Figure 34** The breathing phantom setup prepared for time-resolved imaging

The actuator base is equipped with bipolar stepper motors, which enable the translational and rotational movements of  $\pm 0.1$  mm and  $0.2^\circ$  accuracy, respectively. Additionally, an independently controlled gating device is mounted to the actuator's plate (surrogate), which can simulate the chest or diaphragm motion, depending on the surrogate platform position. The coordination between predefined, via the Motion Control Software, movement scenario is assured by the motion controller. Figure 34

presents a setup prepared for time-resolved imaging with the QA insert positioned in the phantom.

Imaging inserts of various diameters or dedicated to different kinds of detectors might be positioned within the phantom, and translated or rotated in the phantom's lung lobe. Figure 35 presents the breathing phantom with a  $\varnothing 3$  cm soft tissue target inserted for 4DCT imaging purposes and Figure 36 shows the internal structure and dimensions of the imaging rod.

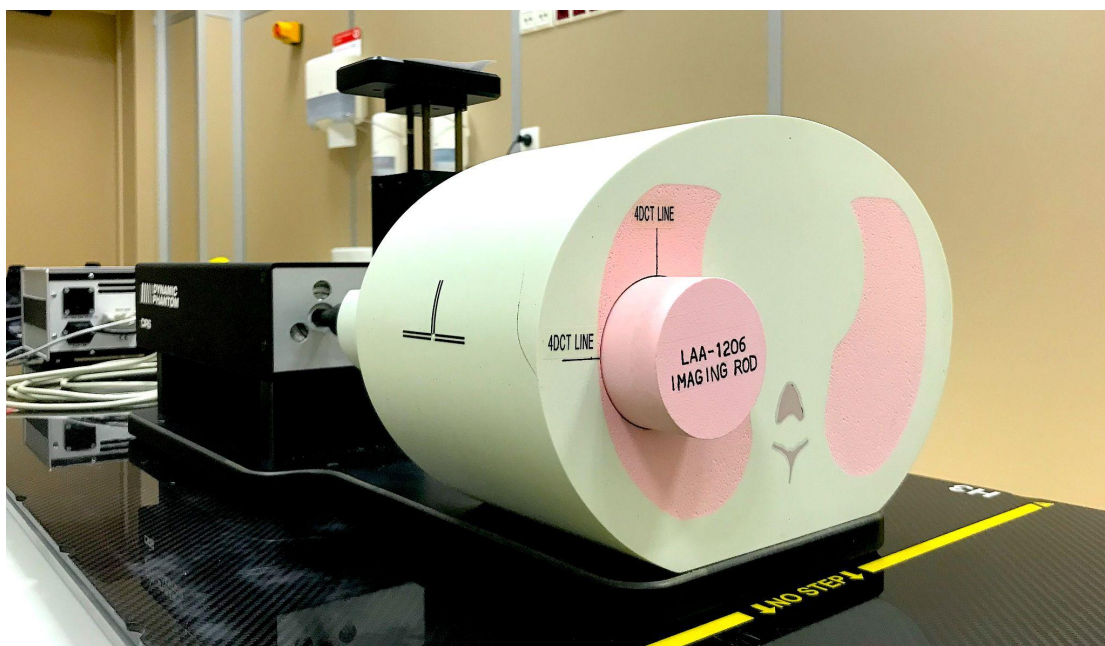


**Figure 35** The breathing phantom with inserted imaging rod

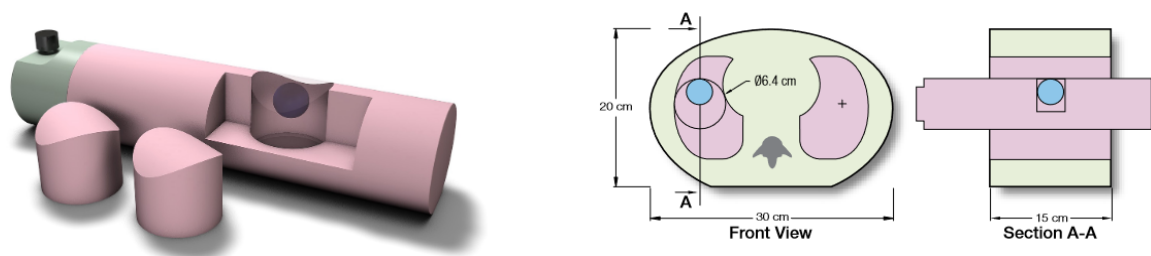


**Figure 36** Cut view and internal structure of the imaging rod (CIRS Dynamic Thorax Motion Phantom: Brochure, 2013)

The CIRS Dynamic Platform (Figure 32) operates similarly to the presented CIRS Dynamic Motion Thorax Phantom. The platform is also connected to the actuator box, with a surrogate platform mimicking chest or diaphragm motion and a controller receiving the signal from Motion Control software (CIRS, 2017). However, the platform can provide the movement only in the superior-inferior direction with  $\pm 0.1$  mm motion accuracy. Due to the platform dimensions and shape, different types of detectors might be used for dosimetric testing, e.g. MatriXX (IBA Dosimetry, Germany) detector.

For 4D imaging purposes, the soft tissue target of  $\varnothing 3$  cm, imitating middle lobe lung cancer, was used. Target movements were controlled with the Motion Control Software version 2.3.0. Three motion scenarios of various amplitudes were chosen for the study, with a motion pattern assumed to have stable and repeatable sinus waveform:

- 1) S-I 5.0 mm,
- 2) S-I 10.0 mm,
- 3) S-I 7.0 mm/A-P 2.5 mm/LAT 1.5 mm.

The breathing cycle time was set to 4 seconds, according to the average quiet respiratory rhythm cycle duration, and there were no variations regarding the starting position. The surrogate, simulating the chest motion, was set to 5.0 mm to assess the correlation between its and the tumor motion. Figure 37 presents the software view regarding the third chosen motion scenario with movements applied in three directions.

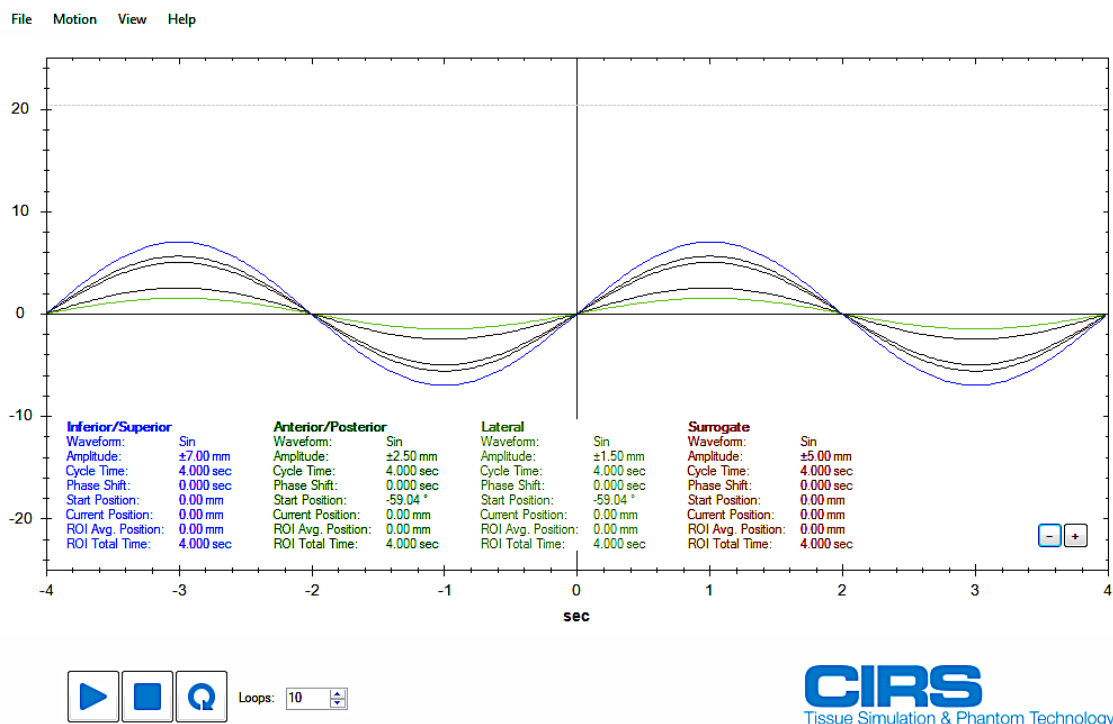


**Figure 37** The CIRS Motion Control Software presenting the details for the third motion scenario including S-I, A-P and LAT target movement directions

Siemens SOMATOM Definition AS was used to perform the time-resolved 4DCT scan. The imaging protocol details are collected in Table 13. The acquired 4DCTs were reconstructed into 10 phases, evenly distributed among the breathing cycle, and exported to the treatment planning system and the average CTs, created independently for each CT dataset from the 4D image. Moreover, the GateCT system was used for data collection and provided the motion pattern information for CT reconstruction to subsequent breathing phases.

**Table 13** Imaging protocol details used for 4DCT data collection

Siemens SOMATOM Definition AS	
slice thickness [mm]	2
data collection diameter [mm]	500
voltage [kV]	120
reconstruction filter/convolution kernel	B30f
exposure time [s]	0.5

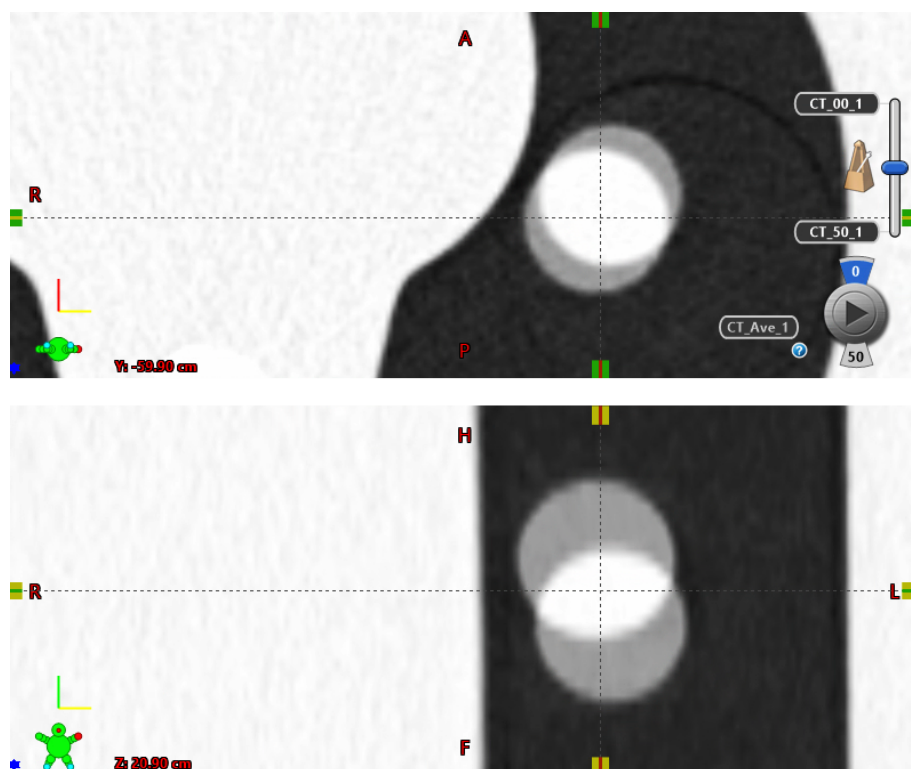


**Figure 38** An example of tumor displacement due to breathing (0% and 50% of the breathing cycle blended)

Based on the acquired 4DCT data, the clinical target volumes (CTVs) were individually delineated on each breathing phase, and, subsequently, their superposition resulted in the internal clinical target volume (ICTV). Due to the anatomical placement of the target, i.e. middle lung lobe, an additional margin of 5.0 mm was added to the ICTV for optimization purposes (ITV). Moreover, the ITV density was overridden to 64 HU, in accordance with the target density value provided by CIRS (1.06 g/cc) and with regard to the measured HU values on the acquired 4DCTs. Figure 38 presents two extreme phases of the (3) motion scenario, i.e. maximum inhale (0%) and maximum exhale (50%) to show the extent of target displacement due to breathing.

The treatment planning was conducted in the Varian Eclipse TPS version 16.1. The prescribed dose was 60 Gy(RBE) in 30 fractions and the calculation grid was set to 1.5 mm to provide high calculation accuracy. Two optimization algorithms were used in the planning process, i.e. PCS and NUPO, to evaluate their differences regarding the dose calculations in demanding anatomies. Three beams from 0°, 45° and 120° angles

were applied. Additional proximal, distal and lateral margins were added in the Field Properties to support the optimization process and achieve good target coverage. Moreover, in plans calculated with the PCS algorithms, all three beams consisted of RS, unlike in NUPO, where it was applied in one beam only (45°). Dedicated dose objectives templates were prepared for both algorithms to ensure planning consistency among different motion scenarios and optimization models. The main planning goal was to achieve clinically acceptable target coverage, thus the constraints regarding the CTV good and homogeneous dose distribution were set at the highest plan priority. Moreover, the NUPO based plans were robustly 3D optimized and the CTV constraints were set as robust objectives and requested to achieve 1 Gy(RBE) more maximally. The robustness evaluation was performed for all PCS and NUPO plans, and included a 2 mm setup and 3.5% curve calibration error uncertainties. The comparison of used optimization algorithms was conducted for all motion scenarios (1, 2, 3).

## **ii. Results**

The next step on the implementation path of moving targets treatments at CCB IFJ PAN was the validation of two optimization algorithms available in the Varian Eclipse TPS, their verification in terms of planning abilities and both dosimetric and robustness results. This part of the study comprised the use of a breathing phantom, described in the previous section, which underwent the 4D imaging and treatment planning using different optimization algorithms (PCS, NUPO) and various motion scenarios. The robust 3D evaluation for the 2 mm setup and 3.5% curve calibration error uncertainties were calculated despite the used algorithm. Therefore, the plans were analyzed in terms of the dose delivered to 98% and 95% volume of the CTV in nominal plans and in possible perturbed scenarios. Table 14 presents the dosimetric differences in target coverage for chosen algorithms.

**Table 14** Dosimetric results for the ITV-optimized plans (including nominal and perturbed scenarios) for various motion amplitudes and different optimization algorithms w/ the robust 3D optimization

optimization algorithm	motion scenario	plan			
		nominal		perturbed (worst-case)	
		V98% [%]	V95% [%]	V98% [%]	V95% [%]
PCS	1	96.50	97.77	88.14	91.75
	2	96.68	98.02	89.03	92.75
	3	97.23	98.28	89.02	92.77
NUPO	1	98.00	98.70	96.50	97.62
	2	98.62	98.99	97.48	98.34
	3	98.75	98.75	96.82	96.82

Nominal plans achieved good target coverage and in all cases reached 98% of the CTV volume covered with at least 95% isodose of the prescribed dose. However, the perturbed scenarios presented bigger discrepancies with regard to the chosen optimization method. The worst perturbed cases of the PCS plans passed the V95% coverage criteria but did not reach the V98%, where the coverage was at the level of 88%-89% of the prescribed dose. Underlying the significant differences with regard to the target coverage and plans robustness is the choice of optimization algorithm and following post-processing procedures. As expected, the dosimetric outcome for the non-robustly ITV-optimized PCS plans showed that these plans were more affected by the applied perturbations. In the case of the NUPO algorithm, target coverage reached the level of clinical acceptability even in the worst-case scenarios. Figure 39 and Figure 40 present the comparison of dose distributions for PCS and NUPO algorithms in the first and second motion scenario, respectively.

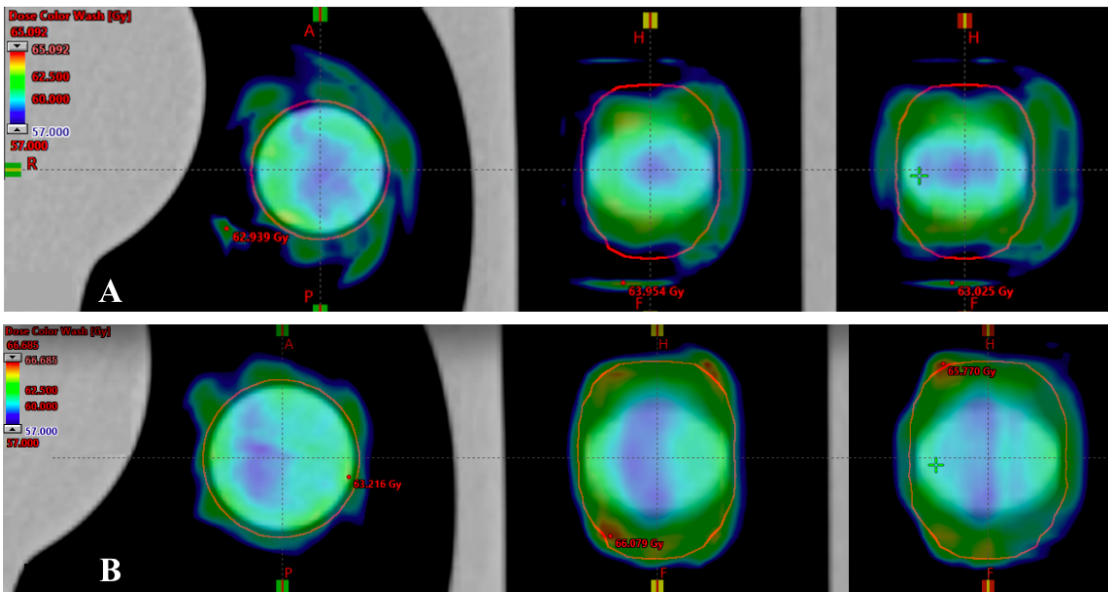


**Figure 39** Comparison of dose distributions (95% isodose of the prescribed dose) for (A) PCS and (B) NUPO algorithms and second motion scenario (S-I, 5.0 mm amplitude); red contour represents the CTV structure

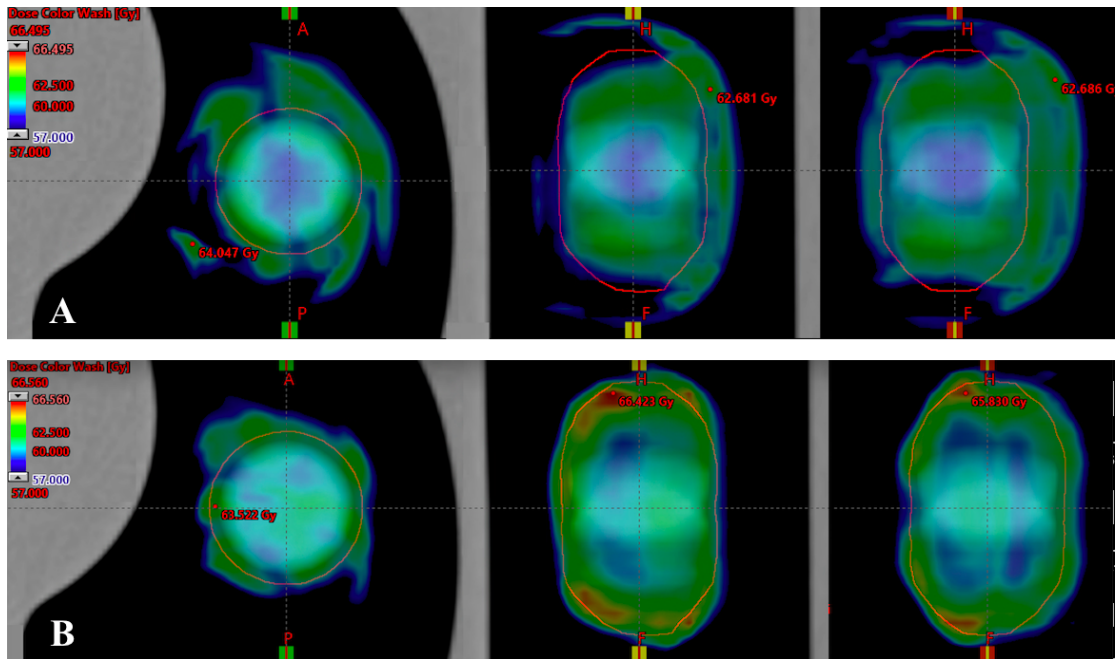


**Figure 40** Comparison of dose distributions (95% isodose of the prescribed dose) for (A) PCS and (B) NUPO algorithms and second motion scenario (S-I, 10.0 mm amplitude); red contour represents the CTV structure

To visualize robustness differences between optimization algorithms, Figure 41 shows the dose-volume histograms (DVHs) for the CTV structure with the inclusion of perturbed scenarios.

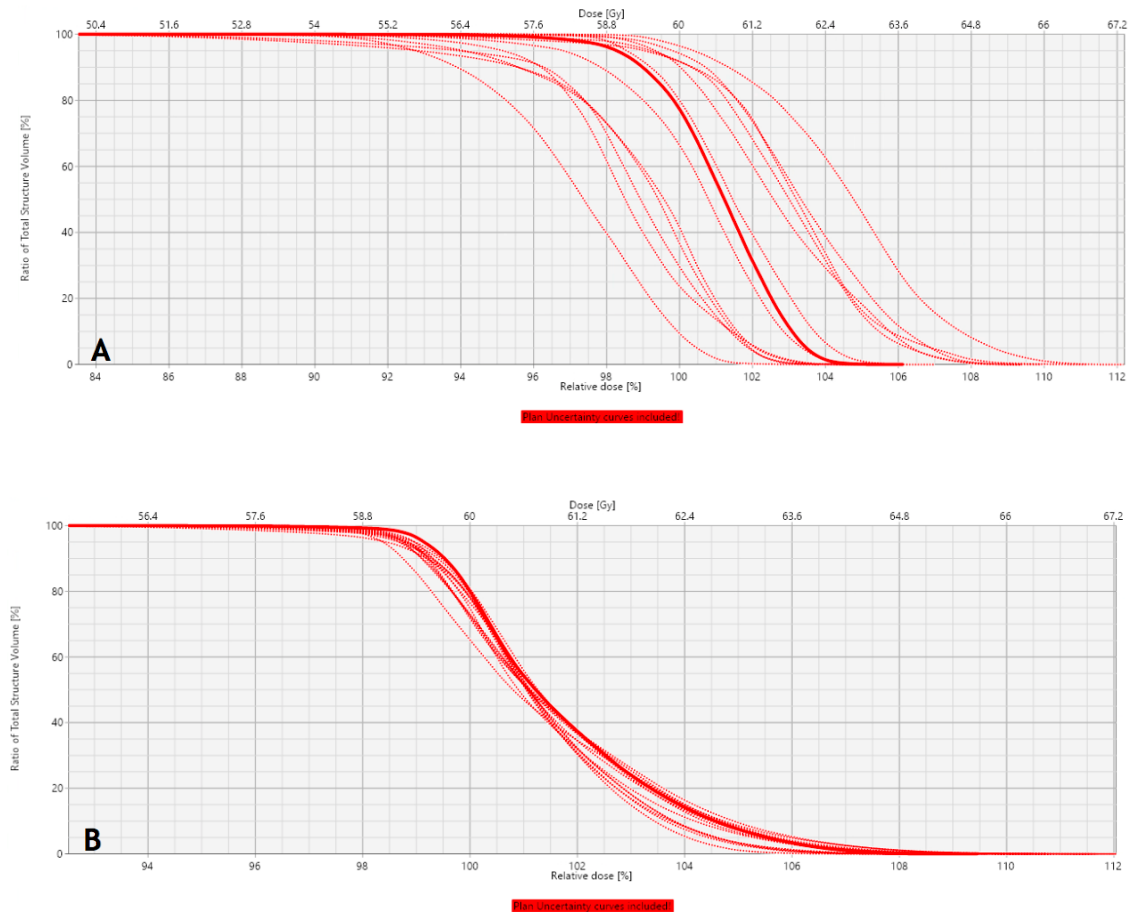


**Figure 41** The dose-volume histograms for the CTV structure and plans optimized with PCS (A) and NUPO (B) algorithms for motion scenario (1) and with included plan uncertainty scenarios

The results of dose distribution and coverage, and the robustness evaluation of plans optimized with PCS or NUPO algorithm, present that the individual use of an ITV-based approach in the treatment planning process is insufficient to create plans of fully acceptable robustness with the PCS only for predefined motion amplitudes. The combination of the ITV-based approach and robust 3D optimization in the NUPO algorithm enabled the assessment of good target coverage, also in case of perturbed scenarios.

### **c. Implementation and validation of rescanning modality**

#### **i. Materials and methods**

Implementation of repainting (also: rescanning) during PBS delivery might be useful in moving target treatments, as it improves the dosimetric outcome by minimizing the deteriorating influence of the interplay effect on planned dose distribution. Main assumption of this technique is to divide the dose to be delivered into many repetitions, thus irradiating either the whole 3D target volume (volumetric) or individual energy layer (layered) several times (Engwall et al., 2018). Moreover, Zenklusen et al. (2010) presented two variations of the layered repainting mode, i.e. scaled and iso-layered (Zenklusen et al., 2010). Scaled repainting refers to an application of a fixed number of rescans to all layers. In the iso-layered repainting the monitor units (MU) value or the dose are determined by the maximum threshold, defined in the TPS Beam Configuration. That leads to various numbers of repaintings for certain energy layers, meaning some of them will be rescanned more times than the others (Engwall et al., 2018). Nevertheless, after repainting the individual layer, the system moves to the layer of lower energy in order to start the painting anew. In the Varian Eclipse TPS there are a few iso-layered rescanning settings which might be chosen during the beam model implementation, i.e. the calculation of numbers of repaints for a given layer might be based on the maximum MU or maximum dose. However, clinically, only a scaled repainting approach is considered with others being under research investigation (Knopf et al., 2011; Zenklusen et al., 2010; Engwall et al., 2018).

At the time of conducting this thesis, none of the repainting strategies were applied at the CCB IFJ PAN and for first testing, as well research purposes, the scaled technique was preferred. The evaluation has started from testing simple geometry plans in order to verify the modality's accuracy and also verify the possibilities of this specific method implementation. Plans were prepared in a *pld* format, a simple format of the input files into the BMS (Beam Management System), quality assurance (QA) and research mode. The reason for using *pld* files was very practical. First of all, the standardly used by the treatment planning and data management systems format, i.e.

DICOM (Digital Imaging and Communications in Medicine), contains not only the information and details regarding the planned beams delivery, but also, e.g. about the patient or imaging. Secondly, the *pld*'s together with BMS mode allows for manual data implementation, simple application of modifications and are often used in QA procedures (OMA Project Description, 2017). In the structure of a *pld* file there are following informations:

- number of layers and total MUs per each field,
- energy, number of elements and spots, MUs per each layer,
- x and y position and MU per each spot.

These are the main input data, which had to be defined at the stage of plan preparation. Moreover, the number of fixed repainting was also added in the *pld* file structure. Regarding the plans itself, these included measurements of single spots and homogeneous fields of 15x15 cm<sup>2</sup> size for 70, 150 and 225 MeV proton beam energies (details included in Table 15 and Table 16). All plans were prepared and measured without repainting, and either 2x or 3x times rescanned, which means that each energy layer was repainted two or three times, respectively. Important informations to take into account, while creating the repainted strategies, were detailed plan properties like the MU/spot value with regard to the set machine parameters, e.g. maximum charge per spot and minimum charge for repainting. In the Varian Eclipse TPS set minimum and maximum MU/spot values are 0.02 and 12.00 MU/spot, respectively. All plans were measured using the Lynx® PT detector (IBA Dosimetry, 2012), which is presented below.

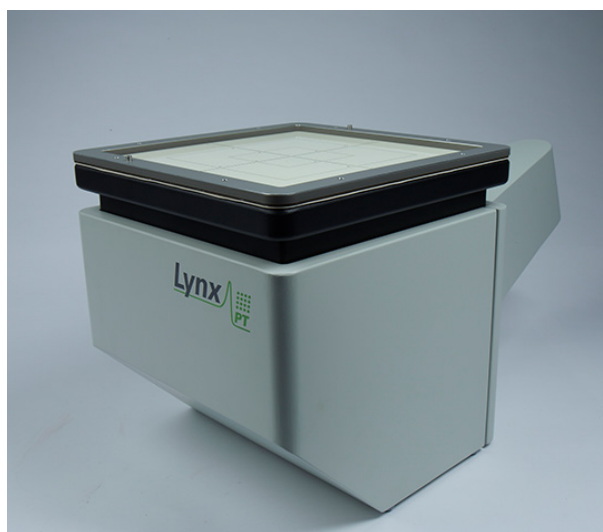


**Figure 42** Lynx® PT detector (IBA Dosimetry, Germany)

The Lynx® PT is a two-dimensional, high accuracy and resolution detector, which enables the performance of a proton beam characterization and is commonly used in the QA procedures (Figure 42). It is a box-shaped device containing a scintillating screen of gadolinium-based, 0.4 mm thick plastic material, which allows for the conversion of the energy loss, due to the radiation, into photons of 540 nm wavelength (green light). Then, photons are reflected by a mirror and collected by the photodiodes of the CCD (charge-coupled device) camera, which is coupled with the scintillating screen. The active surface area of the detector is  $300 \times 300 \text{ mm}^2$ , which allows for the data collection of an effective spatial resolution of 0.5 mm. The detector is also equipped with a various aperture collimation system (iris), in the range of 0 and 100 (where 0 means the iris is closed and 100 means the iris is fully open). For measurement purposes the iris was set to 55.

**Table 15** Details of *pld* plans prepared for the measurements of single spots

Energy [MeV]	delivery mode	total plan MU	MU/spot
<b>70</b>	no repainting	12.50	12.50
	2x	12.50	6.25
	3x	12.50	4.17
<b>150</b>	no repainting	5.00	5.00
	2x	5.00	2.50
	3x	5.00	1.67
<b>225</b>	no repainting	2.00	2.00
	2x	2.00	1.00
	3x	2.00	0.67

**Table 16** Details of *pld* plans prepared for the measurements of 15x15 cm<sup>2</sup> homogeneous fields

Energy [MeV]	delivery mode	total plan MU	MU/spot
<b>70</b>	no repainting	744.20	0.20
	2x	744.20	0.10
	3x	744.20	0.07
<b>150</b>	no repainting	744.20	0.20
	2x	744.20	0.10
	3x	744.20	0.07
<b>225</b>	no repainting	744.20	0.20
	2x	744.20	0.10
	3x	744.20	0.07

An important aspect to include was the correlation of the coordinates of the Lynx® detector measurements with the gantry room coordinate systems, the Fixed Reference System (FRS) and the Gantry Coordinate System (GCS), presented in Figure 43 (AAPM Report of Task Group 11, 2003; IEC, 2011; Ion Beam Applications, 2014). Both systems have their origin at the isocenter. Unlike the FRS system, the GCS is stationary with regard to the rotating gantry (i.e. is moving together with the gantry, perpendicular to the  $z$  axis directed towards the virtual source) and allows for a reference to the Beam Eye View, in which the Lynx® PT coordinates are also defined (Mojżeszek, 2018).

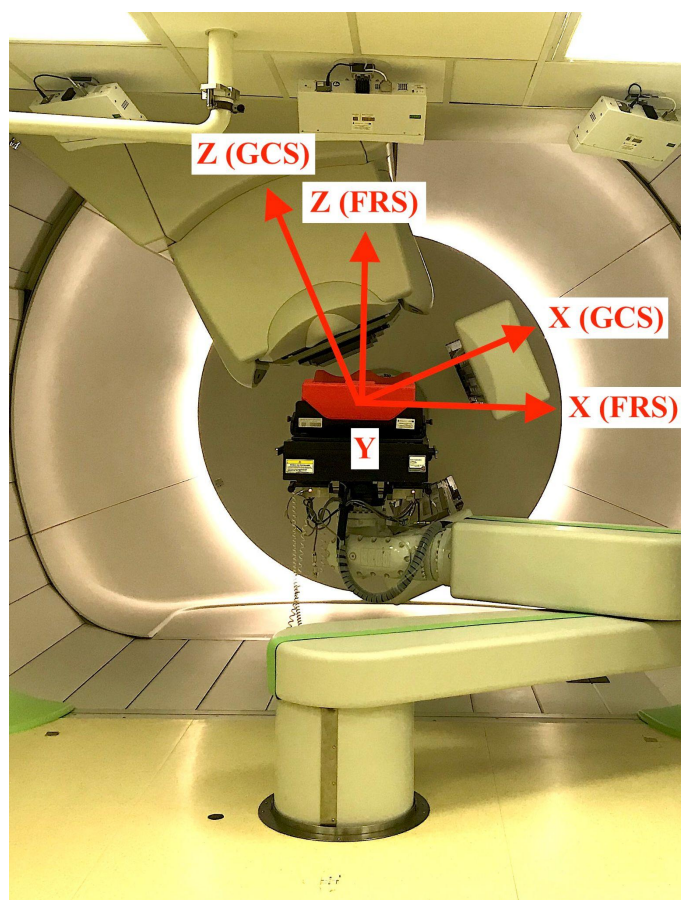


**Figure 43** Standard coordinate systems used at the gantry room, i.e. FRS and GCS

The Lynx® PT detector was used for measurements of singles spots and fields of various proton energies. Obtained results were referred to the guidelines, i.e. international ICRU 78 (2007) and Polish Regulation of Ministry of Health of 3 April 2017 (Journal of Laws, item 884) (acronym *from Polish* “Obwieszczenie Ministra Zdrowia z dnia 3 kwietnia 2017 r. w sprawie ogłoszenia jednolitego tekstu rozporządzenia Ministra Zdrowia w sprawie warunków bezpiecznego stosowania promieniowania jonizującego dla wszystkich ekspozycji medycznej”, 2017), defining the quantitative and qualitative requirements in radiotherapy (ICRU 78, 2007). An in-house developed Matlab-based software (Matlab R2016a) was used for data analysis, i.e. *AnalyseSpot* and *AnalyseField*. Both programs were developed for QA procedures at CCB IFJ PAN by medical physicists from Dosimetry and Quality Control Laboratory, and are dedicated to the installed IBA system and used dosimetry equipment (Liszka, 2019). The input files might be either in the DICOM or OPG format. The first step of

analysis, common for both programs, is the correlation of the coordinate systems of the detector and proton beam, taking into account the camera position with regard to the nozzle. In *AnalyseSpot*, the analysis includes fitting 1D Gaussians to the profiles going through the center of mass or the integrals along  $x$  and  $y$  directions, to derive the spot size ( $\sigma_x, \sigma_y$  - standard deviations of 1D Gaussians in  $x$  and  $y$  directions, respectively) and symmetry ( $S$ ), which is defined as:

$$S = \frac{\sigma_y - \sigma_x}{\sigma_y + \sigma_x} \cdot 100\% \quad (10)$$

In *AnalyseField*, the software derives the  $x$  and  $y$  profiles, normalized to the central part of the field. Then, the lateral penumbra, a region where the dose decreases from 80% to 20% of the maximum value, is derived for both sides of the  $x$  and  $y$  profiles (left/right), which allows, in the next step, for the resulting field size definition. The 1D symmetry ( $S_{field}$ ) and 1D flatness ( $F$ ), for  $x$  and  $y$  directions individually, are calculated according to the equations:

$$S_{field} = \frac{D_L - D_R}{D_L + D_R} \cdot 100\% \quad (11)$$

$$F = \frac{D_{max} - D_{min}}{D_{max} + D_{min}} \cdot 100\% \quad (12)$$

where  $D_L$  and  $D_R$  are the integrals along the left and right side of profiles, respectively. The  $D_{max}$  and  $D_{min}$  are the maximal and minimal dose values within the homogenous, so-called *plateau* field area (above the 80% of the maximum dose).

The next step, after calculating and validating all of the above presented beam parameters, was the analysis of machine log files in order to verify the system performance when the repainting mode is applied. Log files are the documented details regarding the irradiation, recorded after each delivery in the TCS system, relying on the input beam configuration data. Based on that data and irradiation plans, specification maps for the machine are prepared before the delivery. Subsequently, after the irradiation, the log files are recorded with detailed information regarding the time structure of the beam, beam position, charge, dose, etc. All data can be exported from the TCS for further analysis in terms of the delivery structure for a specific plan. The

log files analysis of the plans prepared for this study carefully verified and analyzed the beam position in  $x$  and  $y$  directions, which were measured by two ionization chambers located in the nozzle (IC2/3). The IC2/3 main task is to collect the beam data and control the correctness of beam delivery in terms of its position and dose. The beam position information was derived from recorded files and verified the performance of repainting mode, as well as validated the accuracy of machine delivery.

## ii. Results

As described above, the validation of repainting strategy at the gantry room included the preparation and measurements of single spots and fields for three proton beam energies (70, 150 and 225 MeV), with a Lynx® PT detector. Up to 3 repaintings of each plan were prepared. Subsequently, all the results were analyzed using an in-house developed software, i.e. *AnalaseSpot* and *AnalyseField*, to verify the spot and field sizes, flatness and symmetry results (Table 17, Table 18, Table 19 and Table 20), according to the methodology presented in the previous section.

The beam spot sizes, as well as the symmetry results, for the *no repainting* mode were compared with the beam parameters obtained during reference measurements for that specific gantry and beam model (Table 17). The percentage absolute differences of spot sizes in both directions, i.e.  $x$  and  $y$ , with regard to the reference, did not exceed 0.72% (for the 70 MeV  $\sigma_x$  specifically). Comparison of symmetry results show higher discrepancies, however, obtained results are much lower than agreed center-specific and national consensus for the proton beam symmetry, which is at the level of 10%. Therefore, these results are much alike to be clinically acceptable and show good agreement with the reference.

**Table 17** The results of measured spot sizes ( $\sigma_x$ ,  $\sigma_y$ ) and symmetry ( $S$ ) for proton beams of 70, 150 and 225 MeV energy (meas) with the reference (ref);  $x_{diff}$  and  $y_{diff}$  are the percentage differences of spot sizes in  $x$  and  $y$  directions

Energy [MeV]	$\sigma_x$ [mm]		$\sigma_y$ [mm]		$ x_{diff} $ [%]	$ y_{diff} $ [%]	S [%]		$ S_{diff} $ [%]
	meas	ref	meas	ref			meas	ref	
70	6.443	6.490	6.725	6.710	0.72	0.22	2.1	1.7	0.4
150	3.911	3.920	4.053	4.050	0.23	0.07	1.8	1.6	0.2
225	2.484	2.480	2.713	2.720	0.16	0.26	4.4	4.6	0.2

Table 18 presents the comparison of the same beam parameters, but including various delivery modes. Due to the fact that results for the *no repainting* mode were comparable with the reference obtained during reference measurements, the outcome for repainted strategies was validated against that mode only. The absolute differences in spot sizes between various modes were negligible, as expected, and the observed variations were within tolerance for the scanned beam delivery. Also no significant discrepancies were obtained for the symmetry parameter.

**Table 18** The results of measured spot sizes ( $\sigma_x$ ,  $\sigma_y$ ) and symmetry ( $S$ ) for proton beams of 70, 150 and 225 MeV energy and various delivery modes including *no repainting* or  $2x/3x$  rescanning;  $x_{diff}$  and  $y_{diff}$  are the percentage differences of spot sizes with regard to the *no repainting* delivery mode

Energy [MeV]	delivery mode	$\sigma_x$ [mm]	$\sigma_y$ [mm]	$ x_{diff} $ [%]	$ y_{diff} $ [%]	S [%]
70	no repainting	6.443	6.725	-	-	2.1
	2x	6.436	6.730	0.001	0.001	2.2
	3x	6.435	6.800	0.001	0.011	2.8
150	no repainting	3.911	4.053	-	-	1.8
	2x	3.903	4.069	0.002	0.004	2.1
	3x	3.927	4.087	0.004	0.008	2.0
225	no repainting	2.484	2.713	-	-	4.4
	2x	2.489	2.726	0.002	0.005	4.5
	3x	2.475	2.711	0.004	0.001	4.5

Figures 44-46 present the comparison of single spots distributions of 70, 150 and 225 MeV, measured with Lynx® PT and analyzed with OmniPro I-mRT software, with regard to the chosen delivery mode (IBA Dosimetry, 2012). The *no repainting* and  $2x$  *repainting* modes are compared, and the chart represents profiles going through the

center of each spot in y direction. The measurements were normalized to 100% of the dose.

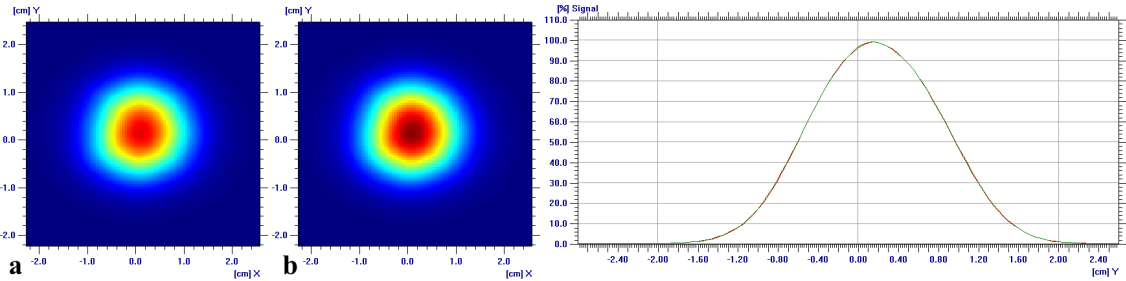


**Figure 44** The comparison of single spots distribution of 70 MeV energy for (a) *no repainting* and (b) *2x repainting* delivery mode; the chart presents comparison of profiles going through the center of spots in y direction

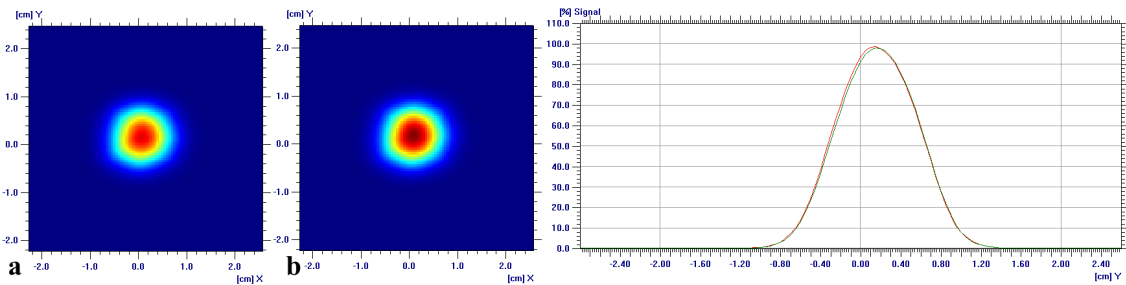


**Figure 45** The comparison of single spots distribution of 150 MeV energy for (a) *no repainting* and (b) *2x repainting* delivery mode; the chart presents comparison of profiles going through the center of spots in y direction

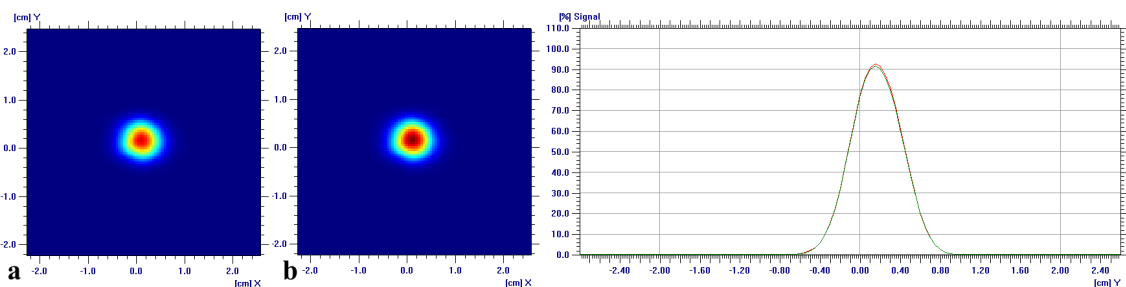


**Figure 46** The comparison of single spots distribution of 225 MeV energy for (a) *no repainting* and (b) *2x repainting* delivery mode; the chart presents comparison of profiles going through the center of spots in y direction

Following step was the analysis of homogeneous 15x15 cm<sup>2</sup> fields for three proton beam energies (70, 150 and 225 MeV) with regard to the applied repainting approach. Table 19 presents the results of field size and symmetry in x and y directions,

as well as the field flatness for three delivery scenarios. The assessed absolute percentage differences between *no repainting* and *2x/3x* rescanning mode showed small variations in the field size (<0.17% for 70 MeV and *x* direction specifically), flatness (<0.32% for 225 MeV),  $S_x$  (<0.14% for 70 MeV) and  $S_y$  (<0.04% for 225 MeV), as assumed.

Table 20 presents complement results for the measured fields including the penumbra (20%-80% of the dose) values for both (left and right) slopes of *x* and *y* profiles. The absolute differences between corresponding left and right slopes of the *x* profiles did not exceed 1.45% for the 225 MeV and 0.72% for 150 MeV energy. The same metrics verified for *y* profiles resulted in the highest values of 2.78% for 70 MeV and 2.33% for 225 MeV energy, respectively.

**Table 19** The results of measured field size (*x*, *y*), flatness (*F*) and symmetry ( $S_x$ ,  $S_y$ ) for proton beams of 70, 150 and 225 MeV energy and various delivery modes including *no repainting* or *2x/3x* rescanning;  $x_{diff}$  and  $y_{diff}$ ,  $F_{diff}$ ,  $S_{x-diff}$  and  $S_{y-diff}$  are the percentage differences of field sizes, flatness and symmetry with regard to the *no repainting* delivery mode, respectively

Energy [MeV]	delivery mode	x [mm]	y [mm]	$ x_{diff} $ [%]	$ y_{diff} $ [%]	F [%]	$ F_{diff} $ [%]	$S_x$ [%]	$S_y$ [%]	$ S_{x-diff} $ [%]	$ S_{y-diff} $ [%]
70	no repainting	152.36	152.41	-	-	2.06	-	0.12	0.09	-	-
	2x	152.51	152.36	0.10	0.04	2.00	0.06	-0.02	0.08	0.14	0.01
	3x	152.62	152.52	0.17	0.07	2.14	0.08	0.11	0.09	0.01	0.00
150	no repainting	152.40	152.73	-	-	2.26	-	0.14	0.09	-	-
	2x	152.45	152.73	0.03	0.00	2.30	0.04	0.13	0.08	0.01	0.01
	3x	152.51	152.76	0.07	0.02	2.20	0.06	0.13	0.08	0.01	0.01
225	no repainting	152.23	152.55	-	-	2.58	-	0.14	0.13	-	-
	2x	152.26	152.65	0.02	0.07	2.47	0.11	0.13	0.09	0.01	0.04
	3x	152.39	152.73	0.10	0.12	2.26	0.32	0.12	0.09	0.02	0.04

**Table 20** The results of measured left/right (L/R) penumbra in  $x$  ( $x_{PL}$ ,  $x_{PR}$ ) and  $y$  ( $y_{PL}$ ,  $y_{PR}$ ) directions for proton beams of 70, 150 and 225 MeV energy and various delivery modes including *no repainting* or  $2x/3x$  rescanning;  $x_{PL/PR-diff}$  and  $y_{PL/PR-diff}$  are the percentage differences in penumbra with regard to the *no repainting* mode delivery

Energy [MeV]	delivery mode	$x_{PL}$ [mm]	$x_{PR}$ [mm]	$y_{PL}$ [mm]	$y_{PR}$ [mm]	$ x_{PL-diff} $ [%]	$ x_{PR-diff} $ [%]	$ y_{PL-diff} $ [%]	$ y_{PR-diff} $ [%]
70	no repainting	11.05	10.90	11.61	11.61	-	-	-	-
	2x	11.11	10.93	11.93	11.69	0.50	0.32	2.78	0.65
	3x	10.99	10.85	11.86	11.79	0.56	0.44	2.17	1.56
150	no repainting	6.60	6.61	6.94	7.00	-	-	-	-
	2x	6.63	6.61	6.95	7.12	0.45	0.09	0.16	1.62
	3x	6.67	6.66	6.99	7.10	1.07	0.72	0.80	1.34
225	no repainting	4.26	4.30	4.64	4.69	-	-	-	-
	2x	4.32	4.33	4.73	4.80	1.47	0.68	2.08	2.33
	3x	4.29	4.28	4.71	4.72	0.70	0.42	1.55	0.52

Figures 47-49 present the comparison of homogeneous  $15 \times 15$  cm<sup>2</sup> fields distributions of 70, 150 and 225 MeV, measured with Lynx® PT and analyzed with OmniPro I-mRT software, with regard to the chosen delivery mode. The *no repainting* and  $2x$  *repainting* modes are compared, and the chart represents profiles going through the center of each field in  $y$  direction. The measurements were normalized to 100% of the dose.

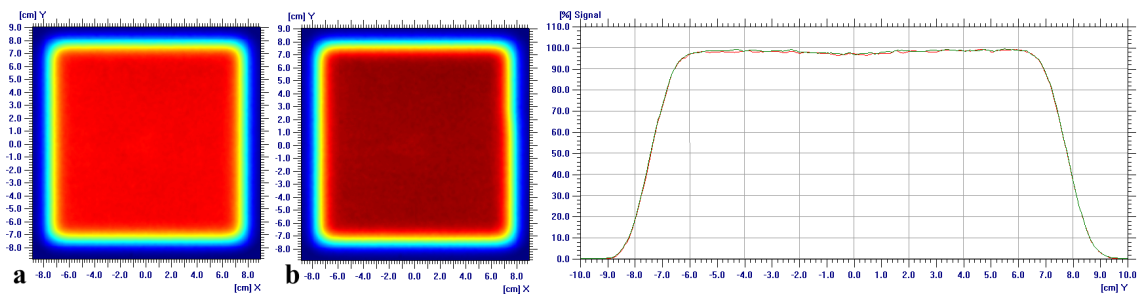


**Figure 47** The comparison of homogeneous  $15 \times 15$  cm<sup>2</sup> fields distribution of 70 MeV energy for (a) *no repainting* and (b)  $2x$  *repainting* delivery mode; the chart presents comparison of profiles going through the center of fields in  $y$  direction

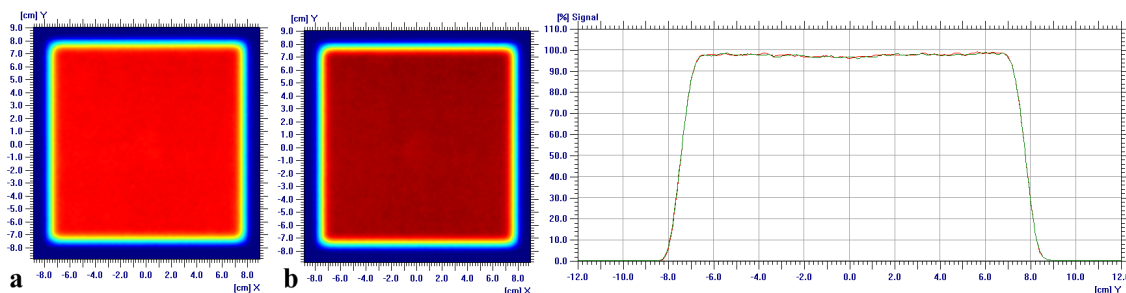


**Figure 48** The comparison of homogeneous 15x15 cm<sup>2</sup> fields distribution of 150 MeV energy for (a) *no repainting* and (b) *2x repainting* delivery mode; the chart presents comparison of profiles going through the center of fields in y direction

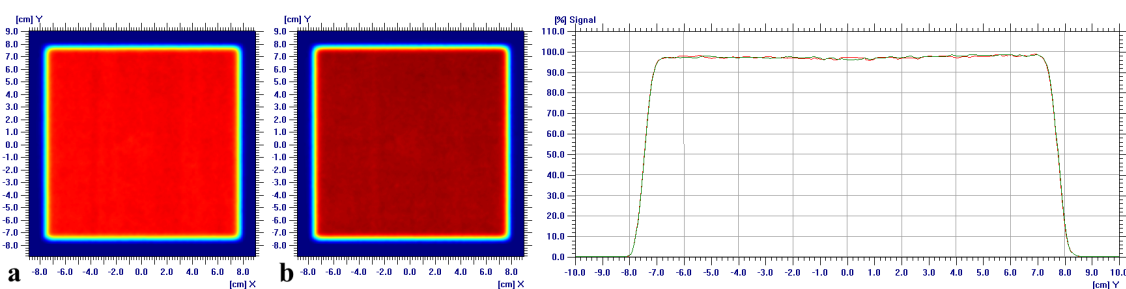


**Figure 49** The comparison of homogeneous 15x15 cm<sup>2</sup> fields distribution of 225 MeV energy for (a) *no repainting* and (b) *2x repainting* delivery mode; the chart presents comparison of profiles going through the center of fields in y direction

Presented results show high reproducibility in the beam spot size and field properties, despite the number of applied repainting, which proves high beam stability during the measurements and ensures the proper functioning of the rescanning modality at the gantry room, which has not been tested before. As mentioned in the previous section, for the plans of simple geometry, the analysis of log files was also conducted to have a thorough view into the rescanning mechanisms during the machine performance. The verification of X and Y positions of the beam on the IC2/3 ionization chambers, derived from log files, directly reflected the application of repainting strategy. The delivery of individual spots and homogeneous fields was divided into predefined, fixed numbers of rescans, i.e. 2x/3x.

#### **d. Equipment and preparations for dosimetry testing**

##### **i. Materials and methods**

The dosimetric testing at the gantry room, due to the platform's limitation, was performed for the two first motion scenarios (in the S-I direction) of the ITV-based

plans. The measurement configuration included the CIRS Dynamic Platform and MatriXX (IBA Dosimetry, 2012) detector, used along with the RW3 Slab Phantom (PTW Freiburg, Germany) (Figure 50).

The RW3 Slab Phantom (PTW Freiburg, Germany) is a water-equivalent phantom dedicated for quality assurance in radiotherapy and is made of Goettingen White Water with a tolerance thickness of  $\pm 1$  mm (Figure 51). The water equivalent thickness of RW3 slabs, which was previously measured for the QA purposes, resulted in 1.035 value.

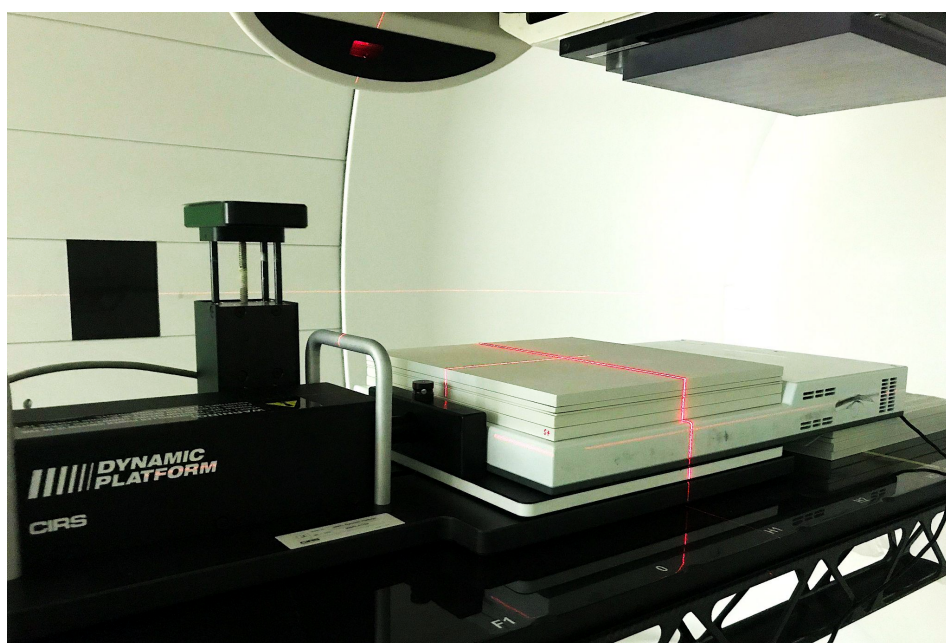


**Figure 50** Setup prepared for measurements: CIRS Dynamic Platform, MatriXX detector and RW3 slab phantom positioned at the treatment couch and aligned with lasers

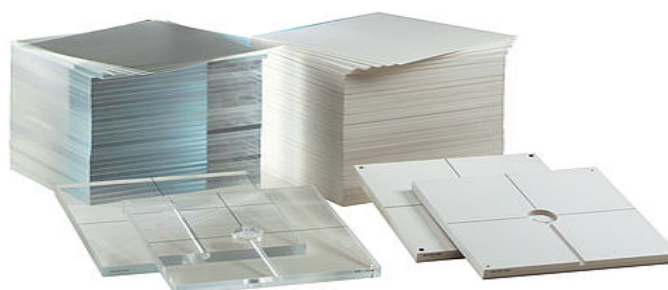


**Figure 51** The PTW absolute dosimetry phantoms with chamber adaptation plates; the RW3 Slab Phantom is presented on the right (PTW Radiation Medicine QA Catalog, Germany)

The MatriXX detector is a 2D ionization chambers array commonly used for treatment plans verification and QA procedures (Figure 52). It allows, e.g. for the comparison of the calculation and delivery quality through the differences assessment between measured 2D and planned dose distributions. The detector consists of an array of 1020 vented ionization chambers in a 32x32 grid and active measurement area of 24.4x24.4 cm. The ionization chambers have 4.2 mm diameter and 2.0 mm height. The measurement resolution responds with the 7.619 mm distance between chambers. The effective point of measurement is located 6 mm below the MatriXX surface, which is marked on the detector's side, which corresponds to the 6.2 mm water equivalent thickness (MatriXX PT User's Guide, IBA Dosimetry, Germany). The detector allows for achieving the so-called *gamma index* (GI) distribution, which provides quantitative dose distribution evaluation, including low and high dose gradients. According to Low et al. (1998), the GI means finding the minimum distance between measured (evaluated) and calculated (reference) points with regard to the defined distance and dose difference criteria, which forms an ellipsoid around the calculated point. The GI passing criteria is met ( $\leq 1$ ) if the measured point is placed within that area. The acceptance GI level was assumed GI(3%/2mm), with the 3% as the accepted dose-difference (DD) value and 2 mm as the measured distance-to-agreement (DTA). The acceptance level was set to 90%. For the dosimetric verification purposes, the dose distributions recalculated in water were used for dose comparison.

The ITV-based plans were prepared according to the PatientQA procedure implemented at CCB. Therefore, all plans were recalculated on a dedicated virtual phantom and the isocenter was set to be within the 95% of the biological total dose for the plan, which corresponded to the 4.0 cm value. Due to the setup configuration, the gantry angles were set to 0 degrees. However, due to the measurements taken in the RW3 Slab Phantom, a recalculation of the measurement depth at the gantry, including the water equivalent thickness of slabs and MatriXX detector together, was necessary and resulted in 3.4 cm thickness of the RW3 phantom as a build-up material.



**Figure 52** The MatriXX detector (MatriXX PT User’s Guide, IBA Dosimetry, Germany)

Subsequently, at the stage of treatment plans preparation for the dosimetric testing, the plans were exported from the TPS. Next, the RT doses, in the *DICOM* format, were converted into the *pld* files, a format of input files read by the BMS mode. The detailed characteristics of the *pld* files was presented in the previous section. For this purpose, as the plans were calculated in the TPS system, an IBA developed software was used. The same software was also used for the preparation of corresponding sets of repainted strategies. For the (1) and (2) motion scenarios, apart from the nominal plans, also the *2x* and *3x repainted* deliveries were prepared in the *pld* format (layered rescanning). However, only *2x repainted* plans were only for motion scenario (1). The conversion of the file format had two reasons. First of all, the BMS mode was preferred to be used during the research testing and thus, the conversion of the plans and modification of the repaintings number, either in the IBA software or manually in the TCS system, were necessary. Secondly, the number of applied repaintings was chosen to have a fixed number and represent scaled repainting mode.

The configuration setup was fixed at the treatment couch. The MatriXX detector was placed on top of the CIRS Dynamic Platform’s movable part. Platform was connected to the actuator, controller and computer with the Motion Control Software installed. The level of the detector was checked and its position was corrected in terms of any pitch or roll rotations, thanks to the six degrees of freedom of the robotic arm.

Then, the MatriXX was carefully aligned at the isocenter with lasers and RW3 Slab Phantom was placed on top of the detector as a build-up material. As mentioned above, the build-up material resulted in 3.4 cm, whose thickness was determined taking into account the WET of the MatriXX effective point of measurement, as well as the 4.0 cm QA plan isocenter for which it was calculated in the TPS. Again, the lasers and setup rotations were checked. Then, the programmed motion scenarios were applied in the Motion Control Software and the preciseness of the motion performance was verified with the use of GateRT camera and software available at the gantry treatment room. However, the software was only used for motion monitoring, the gated delivery was not a part of this study. Irradiation was executed in the BMS mode. Measurements were collected and analyzed in the OmniPro I'mRT software.

## ii. Results

The details regarding the 4D imaging and planning for this study were disclosed in previous sections. For dosimetric verification the total number of four nominal plans were prepared to be delivered according to proposed setup geometry (Figure 50). Moreover, additionally  $2x$  and  $3x$  repainted strategies were also created in the *pld* format. All of the measurements were performed at the zero gantry angle and each of the plans consisted of three irradiation fields. The PCS optimized plans included the RS in all beams, however, in the NUPO plans, the RS was applied only in one beam. The delivery was divided into three parts. First, the reference measurements (static) for both motion scenarios and different optimization algorithms were collected (ITV1\_P, ITV2\_P, ITV1\_N, ITV2\_N, where number (1 or 2) indicates motion scenario and letter (P or N) - the chosen optimizer). Subsequently, the predefined motion amplitude was applied in the Motion Control Software to perform the irradiation during 5.0 or 10.0 mm platform displacement with *no repainting* or  $2x/3x$  rescanned, when applicable, as the third set of measurements. These measurements were conducted assuming constant starting phase and free breathing during the whole time of beam delivery. The OmniPro I'mRT software was used for collecting the dose distributions and to perform the GI(3%/2mm) analysis, assuming 90% level of acceptance. Before starting the analysis, each planned dose distribution plane, exported from TPS, had changed resolution in

order to match the resolution of measurements with the MatriXX detector, which is 7.619 mm. If the measured plan did not pass the GI criteria, the  $\pm 2$  mm planes of the planned dose distributions, exported from the TPS, were allowed for the agreement verification. The results of the gamma index for the (1) and (2) motion scenario, including different algorithms, and analyzed individually for each field, are presented in Table 21 and Table 22.

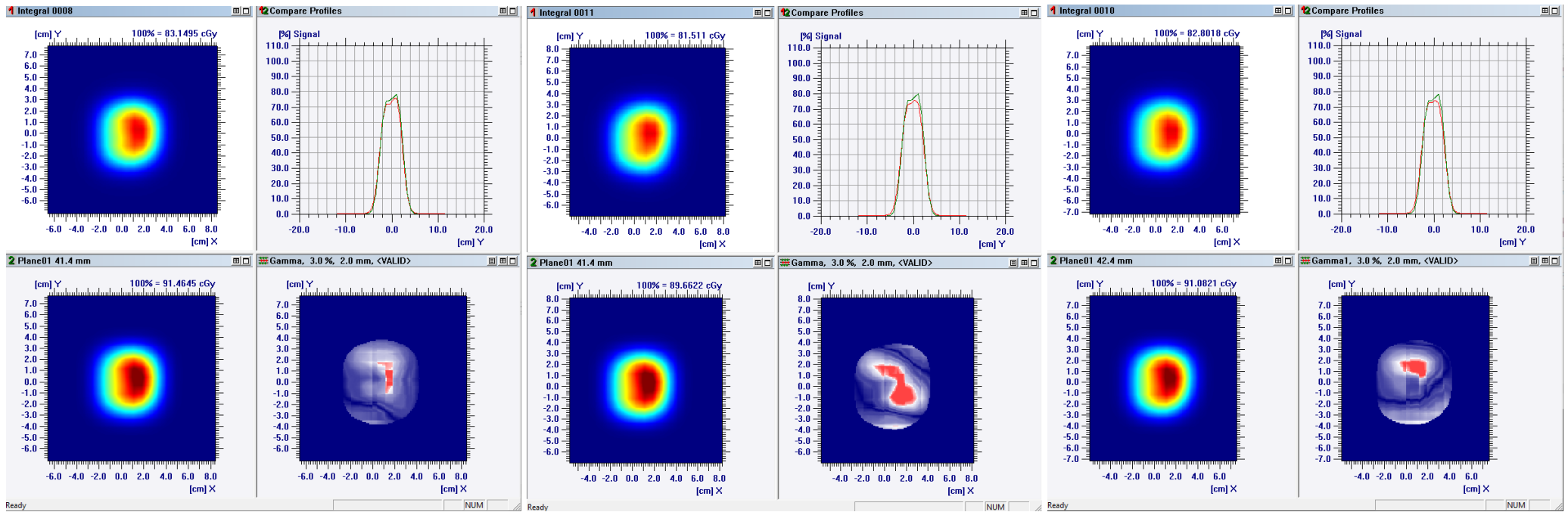
**Table 21** The GI(3%/2mm) results for isocenter and +1mm plane for ITV1\_P and ITV1\_N plans, optimized with the PCS and NUPO algorithm, respectively and (1) motion scenario

	ITV1_P				ITV1_N			
	Field no.	MU	GI (3%/2mm) results [%]		Field no.	MU	GI (3%/2mm) results [%]	
			isocenter plane	+1 mm plane			isocenter plane	+1 mm plane
<b>reference</b>	1	126.81	96.19	-	1	89.88	100.00	-
	2	116.42	88.36	98.65	2	94.35	93.38	-
	3	132.06	87.24	100.00	3	101.30	99.97	-
<b>S-I 5.0 mm (no repainting)</b>	1	126.81	85.32	90.79	1	89.88	98.15	-
	2	116.42	84.35	96.33	2	94.35	80.83	86.47
	3	132.06	83.82	94.92	3	101.30	88.34	75.16
<b>S-I 5.0 mm + 2x repainting</b>	1	126.81	90.25	-	1	89.88	95.47	-
	2	116.42	74.96	86.16	2	94.35	85.65	90.80
	3	132.06	79.19	92.74	3	101.30	91.70	-

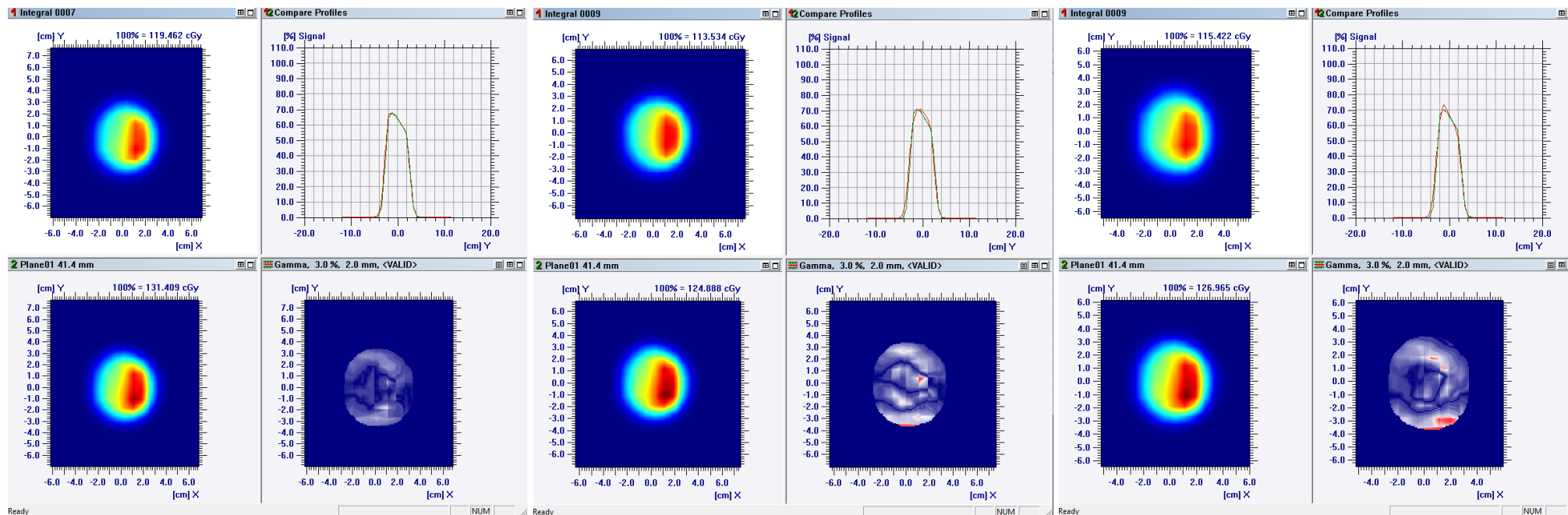
All reference (static) measurements, for both motion scenarios, passed the GI(3%/2mm) criteria, as expected. However, the results for measurements with simulated motion up to 5.0 mm or 10.0 mm showed significant dose deterioration due to target displacement, despite the used optimization algorithm during treatment planning. The dosimetric outcome for motion scenario (1) and PCS algorithm also passed the presumed GI(3%/2mm) metric in the *no repainting* delivery mode (F1=90.79%, F2=96.33%, F3=94.92%). The analysis of the same motion amplitude for a plan optimized with the NUPO algorithm and *no repainting* delivery approach did not pass the acceptance level in two out of three fields (F1=98.15%, F2=86.47%, F3=75.16%). Third set of measurements for motion (1), which included simulated platform

movement combined with the *2x repainting* scenario presented interesting results, i.e. the repainting mode did not improve the dosimetric outcome in plans optimized with the PCS algorithm (two out of three fields passed the criteria, i.e. F1=90.25%, F2=86.16%, F3=92.47%), however, all three fields of the NUPO plan achieved at least 90% of the GI(3%/2mm) metric (F1=95.47%, F2=90.80%, F3=91.70%).

Figure 53 and Figure 54 presents the exemplary results of dose distributions, profiles and GI(3%/2mm) metric for Field 1 for the isocenter plane of the ITV1\_P and ITV1\_N plans, respectively and for three delivery modes. These measurements were conducted for motion scenario S-I 5.0 mm (which corresponds to 10.0 mm peak-to-peak amplitude). The results for the static scenario present good agreement between measured and planned dose distribution. Visible dose deterioration and worse GI(3%/2mm) are seen in the case of simulated motion and applied *repainting* strategy, which was expected. Even so, both plans passed the acceptance criteria during the simulated free breathing delivery, with better results obtained for the NUPO-optimized plan, which might signal its better plan quality and positive influence of the robust 3D optimization, as well as the *rescanning* modality on minimization the deteriorating effect of both motion and *interplay effect*.



**Figure 53** Comparison of dose distributions, profiles and GI(3%/2mm) results for the isocenter plane of ITV1\_P plan, Field 1 for different delivery modes: static (left), S-I (*no repainting*) (middle) and *2x repainting* (right); red curves present the measurements, green curves present the planes exported from TPS (plan was recalculated in a water tank with an isocenter set to 4.14 cm, corresponding to 4.04 cm of RW3 slabs and MatriXX effective point of measurement)



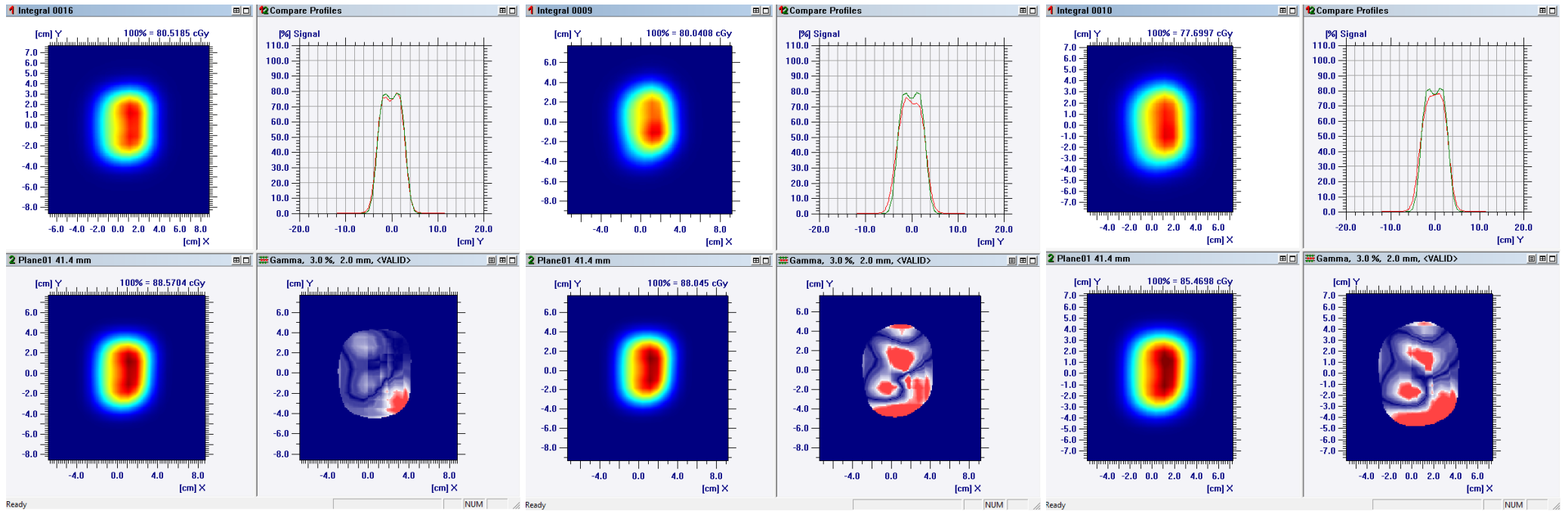
**Figure 54** Comparison of dose distributions, profiles and GI(3%/2mm) results for the isocenter plane of ITV1\_N plan, Field 1 for different delivery modes: static (left), S-I (*no repainting*) (middle) and *2x repainting* (right); red curves present the measurements, green curves present the planes exported from TPS (plan was recalculated in a water tank with an isocenter set to 4.14 cm, corresponding to 4.04 cm of RW3 slabs and MatriXX effective point of measurement)

Table 22 contains the GI(3%/2mm) results for motion scenario (2), i.e. the motion of 10.0 mm in S-I direction (which corresponds to 20.0 mm peak-to-peak amplitude). As mentioned above, all static measurements passed the presumed criteria, however, in the measurements with simulated motion, the dose deterioration was much more affected by both the motion and *interplay effect*. The dosimetric outcome for the plan optimized with the PCS algorithm, for *no repainting* and *2x/3x repaintings* present similar results, however, none of these passed the acceptance criteria. In the case of the plan optimized with the NUPO algorithm, the results for *no repainting* and *2x repainting* were comparable to the PCS, but the implementation of *3x repainting* did improve the outcome and one out of three fields passed the GI(3%/2mm) level. In the PCS plan, the *3x repainting* mode also improved the dosimetric outcome, however, none of the fields passed the acceptance criteria.

**Table 22** The GI(3%/2mm) results for isocenter and -1mm plane for ITV2\_P and ITV2\_N plans, optimized with the PCS and NUPO algorithm, respectively and (2) motion scenario

	Plan ITV2_P				Plan ITV2_N			
	Field no.	MU	GI (3%/2mm) results [%]		Field no.	MU	GI (3%/2mm) results [%]	
			isocenter plane	-1 mm plane			isocenter plane	-1 mm plane
<b>reference</b>	1	152.60	93.43	-	1	106.10	55.50	95.45
	2	139.60	91.25	-	2	96.34	74.51	99.86
	3	154.40	72.41	99.58	3	140.20	90.18	-
<b>S-I 10.0 mm (no repainting)</b>	1	152.60	66.05	74.35	1	106.10	46.34	70.76
	2	139.60	78.23	77.21	2	96.34	71.70	89.12
	3	154.40	60.55	86.65	3	140.20	49.77	47.95
<b>S-I 10.0 mm + 2x repainting</b>	1	152.60	73.85	75.71	1	106.10	47.54	65.54
	2	139.60	75.51	75.26	2	96.34	64.97	66.91
	3	154.40	61.12	77.41	3	140.20	55.61	54.69
<b>S-I 10.0 mm + 3x repainting</b>	1	152.60	81.42	82.96	1	106.10	52.68	91.07
	2	139.60	85.56	89.48	2	96.34	66.02	74.43
	3	154.40	69.38	83.72	3	140.20	77.46	74.89

Figure 55 and Figure 56 also present exemplary results for one of the fields (Field 1) measured at isocenter for ITV1\_P and ITV1\_N plans, respectively. Deteriorated dose distributions for the same plane, as for motion scenario (1), are presented for fair comparison and also in order to highlight the significant impact of motion (here, up to 20.0 mm peak-to-peak amplitude) on the resulting treatment plan quality. In both cases, the use of passive techniques, i.e. an ITV-based approach, *rescanning*, and robust 3D optimization (NUPO), in order to minimize the dose deterioration due to motion, has not been sufficient to overcome the negative impact of breathing during the beam delivery and occurring *interplay effect*. The gated treatments should be considered, as well as the robust 4D optimization, in treatment planning of targets with motion extent exceeding 10.0 mm amplitude.



**Figure 55** Comparison of dose distributions, profiles and GI(3%/2mm) results for the isocenter plane of ITV2\_P plan, Field 1 for different delivery modes: static (left), S-I (*no repainting*) (middle) and *2x repainting* (right); red curves present the measurements, green curves present the planes exported from TPS (plan was recalculated in a water tank with an isocenter set to 4.14 cm, corresponding to 4.04 cm of RW3 slabs and MatriXX effective point of measurement)

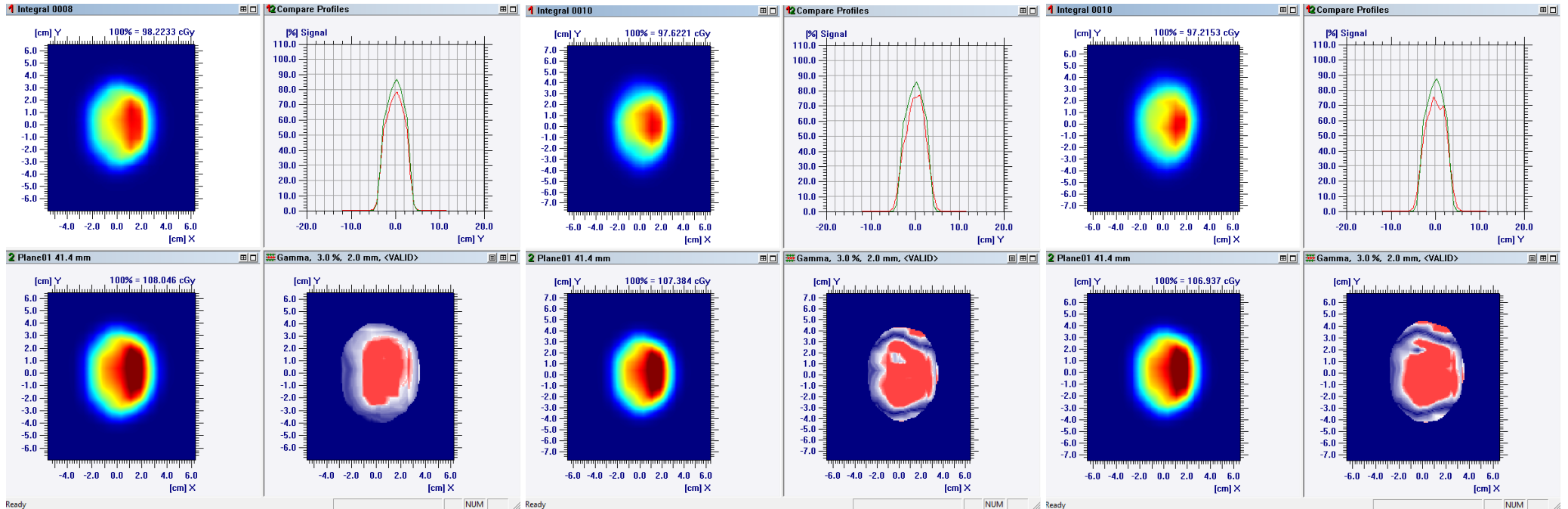


**Figure 56** Comparison of dose distributions, profiles and GI(3%/2mm) results for the isocenter plane of ITV2\_N plan, Field 1 for different delivery modes: static (left), S-I (*no repainting*) (middle) and *2x repainting* (right); red curves present the measurements, green curves present the planes exported from TPS (plan was recalculated in a water tank with an isocenter set to 4.14 cm, corresponding to 4.04 cm of RW3 slabs and MatriXX effective point of measurement)



## 9. Conclusions

The introduction of new indications and their inclusion into the standard clinical practice for a particular facility is always a very complex issue, which combines three main pillars of any kind of radiotherapy, i.e. imaging, treatment planning and dosimetry. The main goal of conducting this thesis was to perform the activities which could support and enable future proton radiotherapy treatments of moving targets at the CCB IFJ PAN facility in Krakow, Poland. Two indications, the main subject of this dissertation, are breast and lung cancer. The choice of these types of cancer, not accidental, was dictated by the facility's future treatment visions. Moreover, based on the world-class literature and the clinical practice of the best radiotherapy centers in the world, there are existing prerequisites demonstrating that these indications might especially profit from proton therapy.

The first goal of the dissertation (Study I) was to assess the dosimetric differences between proton and photon radiotherapy to justify the use of protons in breast cancer treatments and validate the usage of DIBH in proton planning in terms of further OARs sparing. That part of the study was conducted closely with the NU-MED Radiotherapy Center in Elblag, Poland. Relevant to notice is that it was the first study of this kind performed in Poland. The preparation phase for Study I included the measurement and implementation of the CT calibration curve of the CT scanner, which was used for the data collection. Subsequently, the proton plans of 40 were prepared for both FB and BH anatomies (Study II). The dosimetric outcome questioned the advantage of using the DIBH with protons. These results were not as straightforwardly translated into the OARs sparing, as it is in photon radiotherapy. Even though the dose to the heart and cardiac substructures were further minimized with BH, when compared to the FB scenario, there was a significant increase in low doses to the lung, which might play a massive role in the higher probability of late toxicity effects appearance. Based on these results, the FB proton plans were compared to DIBH photon plans. Firstly, the results of FB and BH proton plans were comparable, apart from the doses to

the ipsilateral lung, thus the FB scenario was preferred for further comparison with photons. Secondly, the DIBH technique is commonly used and preferred in photon radiotherapy treatments when available and executable by the patient. Thirdly, the group of patients, which CT imaging data was used in the study, was treated with the DIBH modality. The dosimetric comparison between FB proton and BH photon plans presented a significant reduction in the doses to OARs ensuring excellent target coverage and high conformity of the treatment plans. As underlined in previous sections, by quoting the high-quality research studies from the leading cancer radiotherapy centers in the world, the reduction of the unwanted dose to the heart and cardiac substructures during breast cancer treatments plays a crucial role in the minimization of late effects following the treatment.

Study III is a continuation of Study II. It presents a thorough examination of proton PBS planning approaches, with the special attention paid to the beam angles optimization in breast cancer. The main motivation for conducting this work was lack of consensus guidelines or the consistency in planning among centers, and the significant impact the beam selection has in moving targets treatments due to the increased complexity of such treatments. Two of the chosen beam angle arrangements had priority based on the literature review. However, the dosimetric results and robustness of these plans were not similar. Therefore, the selection was expanded to a total number of five angles scenarios. Planning, which was conducted for both FB and BH anatomies and the robust 3D evaluation results, showed that the choice of three beams might increase the OARs doses, and a similar or better dosimetric outcome might be achieved with other beam arrangements. The use of an *en face* beam might be sufficient from the dosimetric and plan robustness point of view, however, only in certain anatomical cases, in which the proximity to cardiac substructures would not constrict the plan quality nor the beam selection would unnecessarily increase the OARs doses. Using two perpendicular beams to the breast curvature presented the best robustness outcome. It might be preferred in demanding anatomies as a compromise between good target coverage and optimal OARs sparing. The worst dosimetric results presented the lateral beam scenario. The lack of plan robustness resulted in the increased low dose region to the left lung and

deposited the dose to the contralateral breast, which has to be absolutely avoided. The significance of assessed dose differences between planning approaches was achieved by performing statistical analysis presented in Chapter 7. To summarize, the chosen beam arrangement and the additional use of the DIBH technique in protons should be carefully analyzed considering each patients' anatomy individually. In many cases, the solution is not straightforward. A compromise between the chosen planning approach and robustness results may be necessary to achieve the best possible dosimetric outcome. Nevertheless, the study presented optimal planning approaches for breast cancer with PBS beams at CCB IFJ PAN, providing thus a thorough assessment of possible solutions to upcoming challenges and might be a base for creating planning procedures at CCB IFJ PAN in the future.

Study IV is fully dedicated lung cancer treatments, which is a classical 4D indication and covers a wide range of the radiotherapy aspects. However, performed activities might be related to treatments of moving targets in general, as they cover imaging, planning and dosimetry aspects in case the motion occurs. Therefore, the study is divided into three main parts, starting from the 4D imaging, through treatment planning to the beam delivery, including repainting strategy implementation and verification at the CCB IFJ PAN facility. The 4D imaging modality was used to collect the CT datasets for further planning and dosimetry purposes and to validate the VisionRT software usage in breathing signal acquisition. Treatment planning, based on the acquired 4D datasets, was performed with the use of different optimization algorithms to assess their capabilities in lung cancer planning, including the robustness outcome. The NUPO algorithm, which enables the inclusion of robust 3D optimization for selected structures, presented more uncertainty-resistant plans, which in moving targets is of great significance. Next part of Study III implementing rescanning modality, which was subsequently used in the treatment plans testing at the gantry room. The implementation and validation included measurements of single spots and homogeneous fields, for up to 3x repaintings, to verify the system's reproducibility and consistency, when the rescanning delivery mode was enabled. The results showed very good beam parameters repeatability and the conducted log files analysis presented the

machine's performance during the irradiation of repainted plans. The last part of this study was the irradiation of previously prepared plans, optimized with the use of different algorithms, with and without applied rescanning modality during the delivery, to assess the impact of the interplay effect and the dosimetric outcome in the case of the used repainting strategy. The measurements conducted for two motion scenarios presented poor dosimetric results during the combined motion and beam delivery, also in the rescanned scenarios, which might indicate the insufficiency of robust 3D optimization and the significant impact of the interplay effect on these treatment plans quality. The robust 3D optimizer in the NUPO algorithm, a tool available in the Varian Eclipse TPS, should not be individually used in targets of higher motion amplitude, to individually include the motion aspect. However, more data and measurements are needed to verify these assumptions.

To summarize, the common goal of the above-presented studies was to support the implementation procedures for the moving targets treatments at CCB IFJ PAN in the future, through the verification and validation of available radiotherapy tools in terms of their suitability and sufficiency in presented indications.

## Bibliography

- AAPM Report of Task Group 11 (2003). Computer Committee. Information Transfer From Beam Data Acquisition Systems. Online: [https://www.aapm.org/pubs/reports/OR\\_01.pdf](https://www.aapm.org/pubs/reports/OR_01.pdf)
- AlignRT User Guide (2015). Materials provided by VisionRT company (VisionRT Ltd, London, United Kingdom)
- Ares, C., Khan, S., MacArtain, A. M., Heuberger, J., Goitein, G., Gruber, G., Lutters, G., Hug, E. B., Bodis, S., & Lomax, A. J. (2010). Postoperative Proton Radiotherapy for Localized and Locoregional Breast Cancer: Potential for Clinically Relevant Improvements? *International Journal of Radiation Oncology\*Biophysics*, 76(3), 685–697
- Austin, A. M., Douglass, M. J. J., Nguyen, G. T., Cunningham, L., Le, H., Hu, Y., & Penfold, S. N. (2021). Individualised selection of left-sided breast cancer patients for proton therapy based on cost-effectiveness. *Journal of Medical Radiation Sciences*, 68(1), 44–51
- Bentzen, S. M., Constine, L. S., Deasy, J. O., Eisbruch, A., Jackson, A., Marks, L. B., Ten Haken, R. K., & Yorke, E. D. (2010). Quantitative Analyses of Normal Tissue Effects in the Clinic (QUANTEC): An Introduction to the Scientific Issues. *International Journal of Radiation Oncology\*Biophysics*, 76(3), S3–S9
- Bergom, C., Currey, A., Desai, N., Tai, A., & Strauss, J. B. (2018). Deep Inspiration Breath Hold: Techniques and Advantages for Cardiac Sparing During Breast Cancer Irradiation. *Frontiers in Oncology*, 8, 87
- Bert, C., Graeff, C., Riboldi, M., Nill, S., Baroni, G., & Knopf, A.-C. (2014). Advances in 4D Treatment Planning for Scanned Particle Beam Therapy—Report of Dedicated Workshops. *Technology in Cancer Research & Treatment*, 13(6), 485–495
- Bertholet, J., Knopf, A., Eiben, B., McClelland, J., Grimwood, A., Harris, E., Menten, M., Poulsen, P., Nguyen, D. T., Keall, P., & Oelfke, U. (2019). Real-time intrafraction motion monitoring in external beam radiotherapy. *Physics in Medicine & Biology*, 64(15), 15TR01
- Biau, J., Chautard, E., Verrelle, P., & Dutreix, M. (2019). Altering DNA Repair to Improve Radiation Therapy: Specific and Multiple Pathway Targeting. *Frontiers in Oncology*, 9, 1009
- Bortfeld, T. (1997). An analytical approximation of the Bragg curve for therapeutic proton beams. *Medical Physics*, 24(12), 2024–2033
- Bortfeld, T. (2006). IMRT: A review and preview. *Physics in Medicine and Biology*, 51(13), R363–R379
- Bortfeld, T., & Jeraj, R. (2011). The physical basis and future of radiation therapy. *The British Journal of Radiology*, 84(1002), 485–498
- Bradley, J., Bae, K., Choi, N., Forster, K., Siegel, B. A., Brunetti, J., Purdy, J., Faria, S., Vu, T., Thorstad, W., & Choy, H. (2012). A Phase II Comparative Study of Gross Tumor Volume Definition With or Without PET/CT Fusion in Dosimetric Planning for Non-Small-Cell Lung Cancer (NSCLC): Primary Analysis of Radiation Therapy Oncology Group (RTOG) 0515. *International Journal of Radiation Oncology\*Biophysics*, 82(1), 435–441.e1
- Brahme, A., Roos, J.-E., & Lax, I. (1982). Solution of an integral equation encountered in rotation therapy. *Physics in Medicine and Biology*, 27(10), 1221–1229

- Cai, J., Zhang, Y., Vergalasova, I., Zhang, F., Segars, W. P., & Yin, F.-F. (2014). An Integrated Simulation System Based on Digital Human Phantom for 4D Radiation Therapy of Lung Cancer. *Journal of Cancer Therapy*, 05(08), 749–758
- Chang, J. Y., Li, H., Zhu, X. R., Liao, Z., Zhao, L., Liu, A., Li, Y., Sahoo, N., Poenisch, F., Gomez, D. R., Wu, R., Gillin, M., & Zhang, X. (2014). Clinical Implementation of Intensity Modulated Proton Therapy for Thoracic Malignancies. *International Journal of Radiation Oncology\*Biography\*Physics*, 90(4), 809–818
- Chang, J. Y., Zhang, X., Knopf, A., Li, H., Mori, S., Dong, L., Lu, H.-M., Liu, W., Badiyan, S. N., Both, S., Meijers, A., Lin, L., Flampouri, S., Li, Z., Umegaki, K., Simone, C. B., & Zhu, X. R. (2017). Consensus Guidelines for Implementing Pencil-Beam Scanning Proton Therapy for Thoracic Malignancies on Behalf of the PTCOG Thoracic and Lymphoma Subcommittee. *International Journal of Radiation Oncology\*Biography\*Physics*, 99(1), 41–50
- CIRS Dynamic Platform Model 008PL (2013). Dynamic Platform: Brochure. Materials provided by CIRS company (Computerized Imaging Reference Systems, Inc.)
- CIRS Dynamic Thorax Phantom Model 008A (2013). Dynamic Thorax Motion Phantom: Brochure. Materials provided by CIRS company (Computerized Imaging Reference Systems, Inc.)
- CIRS Electron Density Phantom Model 062M (2013). Electron Density Phantom: Data Sheet. Materials provided by CIRS company (Computerized Imaging Reference Systems, Inc.)
- CIRS Motion Control Software (2017). Motion Control Software. Materials provided by CIRS company (Computerized Imaging Reference Systems, Inc.)
- Corbin, K. S., & Mutter, R. W. (2018). Proton therapy for breast cancer: Progress & pitfalls. *Breast Cancer Management*, 7(1), BMT06
- Cuaron, J. J., Chon, B., Tsai, H., Goenka, A., DeBlois, D., Ho, A., Powell, S., Hug, E., & Cahlon, O. (2015). Early Toxicity in Patients Treated With Postoperative Proton Therapy for Locally Advanced Breast Cancer. *International Journal of Radiation Oncology\*Biography\*Physics*, 92(2), 284–291
- Cunningham, L., Penfold, S., Giles, E., Le, H., & Short, M. (2021). Impact of Breast Size on Dosimetric Indices in Proton Versus X-ray Radiotherapy for Breast Cancer. *Journal of Personalized Medicine*, 11(4), 282
- Czerska, K., Emert, F., Kopec, R., Langen, K., McClelland, J. R., Meijers, A., Miyamoto, N., Riboldi, M., Shimizu, S., Terunuma, T., Zou, W., Knopf, A., & Rucinski, A. (2021). Clinical practice vs. state-of-the-art research and future visions: Report on the 4D treatment planning workshop for particle therapy – Edition 2018 and 2019. *Physica Medica*, 82, 54–63
- Darby, S. C., Ewertz, M., McGale, P., Bennet, A. M., Blom-Goldman, U., Brønnum, D., Correa, C., Cutter, D., Gagliardi, G., Gigante, B., Jensen, M.-B., Nisbet, A., Peto, R., Rahimi, K., Taylor, C., & Hall, P. (2013). Risk of Ischemic Heart Disease in Women after Radiotherapy for Breast Cancer. *New England Journal of Medicine*, 368(11), 987–998
- De Kock, E. A. (2003). Program CT\_CALIBRATE. CT calibration curves for proton radiotherapy planning. Medical Radiation Group, iThemba LABS, Republic of South Africa
- De Rose, F., Cozzi, L., Meattini, I., Fogliata, A., Franceschini, D., Franzese, C., Tomatis, S., Becherini, C., Livi, L., & Scorsetti, M. (2020). The Potential Role of Intensity-modulated Proton Therapy in the Regional Nodal Irradiation of Breast Cancer: A Treatment Planning Study. *Clinical Oncology*, 32(1), 26–34

- De Ruyscher, D., Sterpin, E., Haustermans, K., & Depuydt, T. (2015). Tumour Movement in Proton Therapy: Solutions and Remaining Questions: A Review. *Cancers*, 7(3), 1143–1153
- den Otter, L. A., Anakotta, R. M., Weessies, M., Roos, C. T. G., Sijtsema, N. M., Muijs, C. T., Dieters, M., Wijsman, R., Troost, E. G. C., Richter, C., Meijers, A., Langendijk, J. A., Both, S., & Knopf, A. (2020). Investigation of inter-fraction target motion variations in the context of pencil beam scanned proton therapy in non-small cell lung cancer patients. *Medical Physics*, 47(9), 3835–3844
- Depauw, N., Batin, E., Daartz, J., Rosenfeld, A., Adams, J., Kooy, H., MacDonald, S., & Lu, H.-M. (2015). A Novel Approach to Postmastectomy Radiation Therapy Using Scanned Proton Beams. *International Journal of Radiation Oncology\*Biophysics*, 91(2), 427–434
- Depauw, N., Batin, E., Johnson, A., MacDonald, S. M., & Jimenez, R. B. (2020). Arms positioning in post-mastectomy proton radiation: Feasibility and development of a new arms down contouring atlas. *Physics and Imaging in Radiation Oncology*, 14, 6–11
- Durante, M., Orecchia, R., & Loeffler, J. S. (2017). Charged-particle therapy in cancer: Clinical uses and future perspectives. *Nature Reviews Clinical Oncology*, 14(8), 483–495
- Early Breast Cancer Trialists' Collaborative Group (EBCTCG) (2011). Effect of radiotherapy after breast-conserving surgery on 10-year recurrence and 15-year breast cancer death: Meta-analysis of individual patient data for 10 801 women in 17 randomised trials. (2011). *The Lancet*, 378(9804), 1707–1716
- Ehrbar, S., Jöhl, A., Tartas, A., Stark, L. S., Riesterer, O., Klöck, S., Guckenberger, M., & Tanadini-Lang, S. (2017). ITV, mid-ventilation, gating or couch tracking – A comparison of respiratory motion-management techniques based on 4D dose calculations. *Radiotherapy and Oncology*, 124(1), 80–88
- Engwall, E., Glimelius, L., & Hynning, E. (2018). Effectiveness of different rescanning techniques for scanned proton radiotherapy in lung cancer patients. *Physics in Medicine & Biology*, 63(9), 095006
- Fagundes, M., Hug, E. B., Pankuch, M., Fang, C., McNeeley, S., Mao, L., Lavilla, M., Schmidt, S. L., Ward, C., Cahlon, O., & Hartsell, W. F. (2015). Proton Therapy for Local-regionally Advanced Breast Cancer Maximizes Cardiac Sparing. *International Journal of Particle Therapy*, 1(4), 827–844
- Fano, U. (1954). Inelastic Collisions and the Molière Theory of Multiple Scattering. *Physical Review*, 93(1), 117–120
- Fattori, G., Safai, S., Carmona, P. F., Peroni, M., Perrin, R., Weber, D. C., & Lomax, A. J. (2017). Monitoring of breathing motion in image-guided PBS proton therapy: Comparative analysis of optical and electromagnetic technologies. *Radiation Oncology*, 12(1), 63
- Flejmer, A. M., Chehrazi, B., Josefsson, D., Toma-Dasu, I., & Dasu, A. (2017). Impact of physiological breathing motion for breast cancer radiotherapy with proton beam scanning – An in silico study. *Physica Medica*, 39, 88–94
- Flejmer, A. M., Edvardsson, A., Dohlmar, F., Josefsson, D., Nilsson, M., Witt Nyström, P., & Dasu, A. (2016). Respiratory gating for proton beam scanning versus photon 3D-CRT for breast cancer radiotherapy. *Acta Oncologica*, 55(5), 577–583

- Flejmer, A. M., Nyström, P. W., Dohmar, F., Josefsson, D., & Dasu, A. (2015). Potential Benefit of Scanned Proton Beam versus Photons as Adjuvant Radiation Therapy in Breast Cancer. *International Journal of Particle Therapy*, 1(4), 845–855
- GateCT User Guide (2015). Materials provided by VisionRT company (VisionRT Ltd, London, United Kingdom)
- GateRT User Guide (2015). Materials provided by VisionRT company (VisionRT Ltd, London, United Kingdom)
- Gottschalk, B. (2004). Passive Beam Spreading in Proton Radiation therapy. Online: <http://gray.mgh.harvard.edu/attachments/article/212/pbs.pdf>
- Grassberger, C. (2014). Doctoral dissertation: Four-Dimensional Monte Carlo Simulations of Lung Cancer Treatments with Scanned Proton Beams (ETH Zurich, Switzerland)
- Grau, C. (2013). The model-based approach to clinical studies in particle radiotherapy – A new concept in evidence based radiation oncology? *Radiotherapy and Oncology*, 107(3), 265–266
- Hug, E. B. (2018). Proton Therapy for Primary Breast Cancer. *Breast Care*, 13(3), 168–172
- IBA Dosimetry (2012). MatriXX User’s Guide
- IBA Dosimetry (2012). LynX PT User’s Guide
- IBA Dosimetry (2012). OmniPro-Accept User’s Guide
- ICRU 29 (1978). ICRU Report 29: Dose specification for reporting external beam therapy in photons and electrons
- ICRU 49 (1994). ICRU Report 49: Stopping Powers and Ranges for Protons and Alpha Particles
- ICRU 50 (1993). ICRU Report 50: Prescribing, Recording, and Reporting Photon-Beam Therapy
- ICRU 62 (1999). ICRU Report 62: Prescribing, Recording, and Reporting Photon-Beam Therapy (Supplement to ICRU 50)
- ICRU 63 (2001). ICRU Report 63: Nuclear Data for Neutron and Proton Radiotherapy and for Radiation Protection
- ICRU 78 (2007). ICRU Report 78: Prescribing, Recording, and Reporting Proton-Beam Therapy
- ICRU 83 (2010). ICRU Report 83: Prescribing, Recording, and Reporting Intensity-Modulated Photon-Beam Therapy (IMRT)
- International Electrotechnical Commission, International Electrotechnical Commission, & Technical Committee 62. (2011). *Radiotherapy equipment—Coordinates, movements and scales*. International Electrotechnical Commission
- Ion Beam Applications (2014). Proton Therapy System. System description. Materials provided by IBA company (Ion Beam Applications)
- Jensen, N. K. G., Mulder, D., Lock, M., Fisher, B., Zener, R., Beech, B., Kozak, R., Chen, J., Lee, T.-Y., & Wong, E. (2014). Dynamic contrast enhanced CT aiding gross tumor volume delineation of liver tumors: An interobserver variability study. *Radiotherapy and Oncology*, 111(1), 153–157
- Jimenez, R. B., Hickey, S., DePauw, N., Yeap, B. Y., Batin, E., Gadd, M. A., Specht, M., Isakoff, S. J., Smith, B. L., Liao, E. C., Colwell, A. S., Ho, A., Januzzi, J. L., Passeri, J., Neilan, T. G., Taghian, A. G., Lu, H.-M., & MacDonald, S. M. (2019). Phase II Study of Proton Beam Radiation Therapy for Patients With Breast Cancer Requiring Regional Nodal Irradiation. *Journal of Clinical Oncology*, 37(30), 2778–2785

- Jordan, T. J., & Williams, P. C. (1994). The design and performance characteristics of a multileaf collimator. *Physics in Medicine and Biology*, 39(2), 231–251
- Kang, Y., Zhang, X., Chang, J. Y., Wang, H., Wei, X., Liao, Z., Komaki, R., Cox, J. D., Balter, P. A., Liu, H., Zhu, X. R., Mohan, R., & Dong, L. (2007). 4D Proton treatment planning strategy for mobile lung tumors. *International Journal of Radiation Oncology\*Biophysics*, 67(3), 906–914
- Kardar, L., Li, Y., Li, X., Li, H., Cao, W., Chang, J. Y., Liao, L., Zhu, R. X., Sahoo, N., Gillin, M., Liao, Z., Komaki, R., Cox, J. D., Lim, G., & Zhang, X. (2014). Evaluation and mitigation of the interplay effects of intensity modulated proton therapy for lung cancer in a clinical setting. *Practical Radiation Oncology*, 4(6), e259–e268
- Käsmann, L., Dietrich, A., Staab-Weijnitz, C. A., Manapov, F., Behr, J., Rimner, A., Jeremic, B., Senan, S., De Ruysscher, D., Lauber, K., & Belka, C. (2020). Radiation-induced lung toxicity – cellular and molecular mechanisms of pathogenesis, management, and literature review. *Radiation Oncology*, 15(1), 214
- Khamfongkhrua, C., Thongsawad, S., Tannanonta, C., & Chamchod, S. (2017). Comparison of CT images with average intensity projection, free breathing, and mid-ventilation for dose calculation in lung cancer. *Journal of Applied Clinical Medical Physics*, 18(2), 26–36
- Kłodowska, M. (2018). Doctoral dissertation: Application of Monte Carlo methods in transport modelling of the therapeutic proton beam (Institute of Nuclear Physics Polish Academy of Sciences, Krakow, Poland)
- Knopf, A., Bert, C., Heath, E., Nill, S., Kraus, K., Richter, D., Hug, E., Pedroni, E., Safai, S., Albertini, F., Zenklusen, S., Boye, D., Söhn, M., Soukup, M., Sobotta, B., & Lomax, A. (2010). Special report: Workshop on 4D-treatment planning in actively scanned particle therapy-Recommendations, technical challenges, and future research directions: 4D-treatment planning in actively scanned particle therapy. *Medical Physics*, 37(9), 4608–4614
- Knopf, A.-C., Czerska, K., Fracchiolla, F., Graeff, C., Molinelli, S., Rinaldi, I., Rucincki, A., Sterpin, E., Stützer, K., Trnkova, P., Zhang, Y., Chang, J. Y., Giap, H., Liu, W., Schild, S. E., Simone, C. B., Lomax, A. J., & Meijers, A. (2022). Clinical necessity of multi-image based (4DMIB) optimization for targets affected by respiratory motion and treated with scanned particle therapy – A comprehensive review. *Radiotherapy and Oncology*, 169, 77–85
- Knopf, A.-C., Hong, T. S., & Lomax, A. (2011). Scanned proton radiotherapy for mobile targets—The effectiveness of re-scanning in the context of different treatment planning approaches and for different motion characteristics. *Physics in Medicine and Biology*, 56(22), 7257–7271
- Knopf, A.-C., Stützer, K., Richter, C., Rucinski, A., da Silva, J., Phillips, J., Engelsman, M., Shimizu, S., Werner, R., Jakobi, A., Göksel, O., Zhang, Y., Oshea, T., Fast, M., Perrin, R., Bert, C., Rinaldi, I., Korevaar, E., & McClelland, J. (2016). Required transition from research to clinical application: Report on the 4D treatment planning workshops 2014 and 2015. *Physica Medica*, 32(7), 874–882
- Krieger, M., Giger, A., Salomir, R., Bieri, O., Celicanin, Z., Cattin, P. C., Lomax, A. J., Weber, D. C., & Zhang, Y. (2020). Impact of internal target volume definition for pencil beam scanned proton treatment planning in the presence of respiratory motion variability for lung cancer: A proof of concept. *Radiotherapy and Oncology*, 145, 154–161
- Langendijk, J. A., Lambin, P., De Ruysscher, D., Widder, J., Bos, M., & Verheij, M. (2013). Selection of patients for radiotherapy with protons aiming at reduction of side effects: The model-based approach. *Radiotherapy and Oncology*, 107(3), 267–273

- Lazarev, S., Rosenzweig, K., Samstein, R., Salgado, L. R., Hasan, S., Press, R. H., Sharma, S., Powell, C. A., Hirsch, F. R., & Simone, C. B. (2021). Where are we with proton beam therapy for thoracic malignancies? Current status and future perspectives. *Lung Cancer*, *152*, 157–164
- Li, H., Zhu, X. R., & Zhang, X. (2015). Reducing Dose Uncertainty for Spot-Scanning Proton Beam Therapy of Moving Tumors by Optimizing the Spot Delivery Sequence. *International Journal of Radiation Oncology\*Biography\*Physics*, *93*(3), 547–556
- Li, Y., Kardar, L., Li, X., Li, H., Cao, W., Chang, J. Y., Liao, L., Zhu, R. X., Sahoo, N., Gillin, M., Liao, Z., Komaki, R., Cox, J. D., Lim, G., & Zhang, X. (2014). On the interplay effects with proton scanning beams in stage III lung cancer: Interplay effects with proton scanning in lung cancer. *Medical Physics*, *41*(2), 021721
- Lin, L. L., Vennarini, S., Dimofte, A., Ravanelli, D., Shillington, K., Batra, S., Tochner, Z., Both, S., & Freedman, G. (2015). Proton beam versus photon beam dose to the heart and left anterior descending artery for left-sided breast cancer. *Acta Oncologica*, *54*(7), 1032–1039
- Liszka, M. (2019). Doctoral dissertation: Dozymetria referencyjna skanującej wiązki protonowej z zastosowaniem komór jonizacyjnych (Institute of Nuclear Physics Polish Academy of Sciences, Krakow, Poland)
- Liu, H. H., Balter, P., Tutt, T., Choi, B., Zhang, J., Wang, C., Chi, M., Luo, D., Pan, T., Hunjan, S., Starkschall, G., Rosen, I., Prado, K., Liao, Z., Chang, J., Komaki, R., Cox, J. D., Mohan, R., & Dong, L. (2007). Assessing Respiration-Induced Tumor Motion and Internal Target Volume Using Four-Dimensional Computed Tomography for Radiotherapy of Lung Cancer. *International Journal of Radiation Oncology\*Biography\*Physics*, *68*(2), 531–540
- Liu, W., Liao, Z., Schild, S. E., Liu, Z., Li, H., Li, Y., Park, P. C., Li, X., Stoker, J., Shen, J., Keole, S., Anand, A., Fatyga, M., Dong, L., Sahoo, N., Vora, S., Wong, W., Zhu, X. R., Bues, M., & Mohan, R. (2015). Impact of respiratory motion on worst-case scenario optimized intensity modulated proton therapy for lung cancers. *Practical Radiation Oncology*, *5*(2), e77–e86
- Low, D. A., Harms, W. B., Mutic, S., & Purdy, J. A. (1998). A technique for the quantitative evaluation of dose distributions. *Medical Physics*, *25*(5), 656–661
- Lühr, A., von Neubeck, C., Krause, M., & Troost, E. G. C. (2018). Relative biological effectiveness in proton beam therapy – Current knowledge and future challenges. *Clinical and Translational Radiation Oncology*, *9*, 35–41
- Mackie, T. R. (2006). History of tomotherapy. *Physics in Medicine and Biology*, *51*(13), R427–R453
- Malicki, J. & Ślosarek, K., red. (2018). *Planowanie leczenia i dozymetria w radioterapii. T. 2 T. 2. Via Medica*
- Mast, M. E., Vredeveld, E. J., Credoe, H. M., van Egmond, J., Heijenbrok, M. W., Hug, E. B., Kalk, P., van Kempen-Harteveld, L. M. L., Korevaar, E. W., van der Laan, H. P., Langendijk, J. A., Rozema, H. J. E., Petoukhova, A. L., Schippers, J. M., Struikmans, H., & Maduro, J. H. (2014). Whole breast proton irradiation for maximal reduction of heart dose in breast cancer patients. *Breast Cancer Research and Treatment*, *148*(1), 33–39
- Matsuura, T., Miyamoto, N., Shimizu, S., Fujii, Y., Umezawa, M., Takao, S., Nihongi, H., Toramatsu, C., Sutherland, K., Suzuki, R., Ishikawa, M., Kinoshita, R., Maeda, K., Umegaki, K., & Shirato, H. (2013). Integration of a real-time tumor monitoring system into gated proton spot-scanning beam therapy: An initial phantom study using patient tumor trajectory data: Integration of real-time tumor-monitoring into gated proton therapy. *Medical Physics*, *40*(7), 071729

- Meijers, A., Jakobi, A., Stützer, K., Guterres Marmitt, G., Both, S., Langendijk, J. A., Richter, C., & Knopf, A. (2019). Log file-based dose reconstruction and accumulation for 4D adaptive pencil beam scanned proton therapy in a clinical treatment planning system: Implementation and proof-of-concept. *Medical Physics*, *46*(3), 1140–1149
- Meijers, A., Seller, O. C., Free, J., Bondesson, D., Seller Oria, C., Rabe, M., Parodi, K., Landry, G., Langendijk, J. A., Both, S., Kurz, C., & Knopf, A. (2020). Assessment of range uncertainty in lung-like tissue using a porcine lung phantom and proton radiography. *Physics in Medicine & Biology*, *65*(15), 155014
- Mojżeszek, N. (2018). Doctoral dissertation: Dozymetria i kontrola jakości skanującej wiązki protonowej na stanowisku gantry (Institute of Nuclear Physics Polish Academy of Sciences, Krakow, Poland)
- Moliere, G. (1947). Theorie der Streuung schneller geladener Teilchen I. Einzelstreuung am abgeschirmten Coulomb-Feld. *Zeitschrift Für Naturforschung A*, *2*(3), 133–145
- Moliere, G. (1948). Theorie der Streuung schneller geladener Teilchen II Mehrfach-und Vielfachstreuung. *Zeitschrift Für Naturforschung A*, *3*(2), 78–97
- Mondlane, G., Gubanski, M., Lind, P. A., Ureba, A., & Siegbahn, A. (2017). Comparative study of the calculated risk of radiation-induced cancer after photon- and proton-beam based radiosurgery of liver metastases. *Physica Medica*, *42*, 263–270
- Mori, S., Knopf, A., & Umegaki, K. (2018). Motion management in particle therapy. *Medical Physics*, *45*(11)
- Muirhead, R., McNee, S. G., Featherstone, C., Moore, K., & Muscat, S. (2008). Use of Maximum Intensity Projections (MIPs) for Target Outlining in 4DCT Radiotherapy Planning. *Journal of Thoracic Oncology*, *3*(12), 1433–1438
- Murray, L. J., & Lilley, J. (2020). Radiotherapy: Technical aspects. *Medicine*, *48*(2), 79–83
- Mutter, R. W., Choi, J. I., Jimenez, R. B., Kirova, Y. M., Fagundes, M., Haffty, B. G., Amos, R. A., Bradley, J. A., Chen, P. Y., Ding, X., Carr, A. M., Taylor, L. M., Pankuch, M., Vega, R. B. M., Ho, A. Y., Nyström, P. W., McGee, L. A., Urbanic, J. J., Cahlon, O., ... MacDonald, S. M. (2021). Proton Therapy for Breast Cancer: A Consensus Statement From the Particle Therapy Cooperative Group Breast Cancer Subcommittee. *International Journal of Radiation Oncology\*Biophysics*, *111*(2), 337–359
- Newhauser, W. D., & Zhang, R. (2015). The physics of proton therapy. *Physics in Medicine and Biology*, *60*(8), R155–R209
- Obwieszczenie Ministra Zdrowia z dnia 3 kwietnia 2017 r. w sprawie ogłoszenia jednolitego tekstu rozporządzenia Ministra Zdrowia w sprawie warunków bezpiecznego stosowania promieniowania jonizującego dla wszystkich ekspozycji medycznej (2017).
- Ödén, J., Toma-Dasu, I., Eriksson, K., Flejmer, A. M., & Dasu, A. (2017). The influence of breathing motion and a variable relative biological effectiveness in proton therapy of left-sided breast cancer. *Acta Oncologica*, *56*(11), 1428–1436
- OMA, Project Number: 675265 (2017). Deliverable Report. D2.7 First software version ready for test (WP2: Beam imaging and diagnostics, IBA)
- Otto, K. (2007). Volumetric modulated arc therapy: IMRT in a single gantry arc: Single arc radiation therapy. *Medical Physics*, *35*(1), 310–317
- Paganetti, H. (2012). Proton Therapy Physics (CRC Press Taylor & Francis Group)

- Paganetti, H. (2018). Proton Therapy Physics 2nd Edition (CRC Press Taylor & Francis Group)
- Patel, S. A., Lu, H.-M., Nyamwanda, J. A., Jimenez, R. B., Taghian, A. G., MacDonald, S. M., & Depauw, N. (2017). Postmastectomy radiation therapy technique and cardiopulmonary sparing: A dosimetric comparative analysis between photons and protons with free breathing versus deep inspiration breath hold. *Practical Radiation Oncology*, 7(6), e377–e384
- Pedroni, E., Scheib, S., Böhringer, T., Coray, A., Grossmann, M., Lin, S., & Lomax, A. (2005). Experimental characterization and physical modelling of the dose distribution of scanned proton pencil beams. *Physics in Medicine and Biology*, 50(3), 541–561
- Podgorsak, E. (2005). Radiation Oncology Physics: A Handbook for Teachers and Students (International Atomic Energy Agency, Vienna, 2005)
- PTW 2019 RW3 Slab Phantom User's Manual. Radiation Medicine QA: Solutions
- Purdy, J. (2004). Current ICRU definitions of volumes: Limitations and future directions. *Seminars in Radiation Oncology*, 14(1), 27–40
- Raptis, A., Ödén, J., Ardenfors, O., Flejmer, A. M., Toma-Dasu, I., & Dasu, A. (2020). Cancer risk after breast proton therapy considering physiological and radiobiological uncertainties. *Physica Medica*, 76, 1–6
- Register, S. P., Zhang, X., Mohan, R., & Chang, J. Y. (2011). Proton Stereotactic Body Radiation Therapy for Clinically Challenging Cases of Centrally and Superiorly Located Stage I Non-Small-Cell Lung Cancer. *International Journal of Radiation Oncology\*Biography\*Physics*, 80(4), 1015–1022
- Rochet, N., Drake, J. I., Harrington, K., Wolfgang, J. A., Napolitano, B., Sadek, B. T., Shenouda, M. N., Keruakous, A. R., Niemierko, A., & Taghian, A. G. (2015). Deep inspiration breath-hold technique in left-sided breast cancer radiation therapy: Evaluating cardiac contact distance as a predictor of cardiac exposure for patient selection. *Practical Radiation Oncology*, 5(3), e127–e134
- Rozporządzenie Ministra Zdrowia z 6 czerwca 2016 r. zmieniające rozporządzenie w sprawie świadczeń gwarantowanych z zakresu leczenia szpitalnego (2016).
- Schlegel, W., Bortfeld, T., & Grosu, A. (Eds.). (2006). *New technologies in radiation oncology*. Springer.
- Schneider, U., Pedroni, E., & Lomax, A. (1996). The calibration of CT Hounsfield units for radiotherapy treatment planning. *Physics in Medicine and Biology*, 41(1), 111–124
- Shen, J., Liu, W., Anand, A., Stoker, J. B., Ding, X., Fatyga, M., Herman, M. G., & Bues, M. (2015). Impact of range shifter material on proton pencil beam spot characteristics: Range shifter material for proton pencil beam. *Medical Physics*, 42(3), 1335–1340
- Shimizu, S., Miyamoto, N., Matsuura, T., Fujii, Y., Umezawa, M., Umegaki, K., Hiramoto, K., & Shirato, H. (2014). A Proton Beam Therapy System Dedicated to Spot-Scanning Increases Accuracy with Moving Tumors by Real-Time Imaging and Gating and Reduces Equipment Size. *PLoS ONE*, 9(4), e94971
- Simone, C. B. (2017). Thoracic Radiation Normal Tissue Injury. *Seminars in Radiation Oncology*, 27(4), 370–377
- Skowronek, J. (2017). Current status of brachytherapy in cancer treatment – short overview. *Journal of Contemporary Brachytherapy*, 9(6), 581–589

- Smyth, L. M., Knight, K. A., Aarons, Y. K., & Wasiak, J. (2015). The cardiac dose-sparing benefits of deep inspiration breath-hold in left breast irradiation: A systematic review. *Journal of Medical Radiation Sciences*, 62(1), 66–73
- Stick, L. B., Yu, J., Maraldo, M. V., Aznar, M. C., Pedersen, A. N., Bentzen, S. M., & Vogelius, I. R. (2017). Joint Estimation of Cardiac Toxicity and Recurrence Risks After Comprehensive Nodal Photon Versus Proton Therapy for Breast Cancer. *International Journal of Radiation Oncology\*Biography\*Physics*, 97(4), 754–761
- Sung, H., Ferlay, J., Siegel, R. L., Laversanne, M., Soerjomataram, I., Jemal, A., & Bray, F. (2021). Global Cancer Statistics 2020: GLOBOCAN Estimates of Incidence and Mortality Worldwide for 36 Cancers in 185 Countries. *CA: A Cancer Journal for Clinicians*, 71(3), 209–249
- Tambas, M., Steenbakkens, R. J. H. M., van der Laan, H. P., Wolters, A. M., Kierkels, R. G. J., Scandurra, D., Korevaar, E. W., Oldehinkel, E., van Zon-Meijer, T. W. H., Both, S., van den Hoek, J. G. M., & Langendijk, J. A. (2020). First experience with model-based selection of head and neck cancer patients for proton therapy. *Radiotherapy and Oncology*, 151, 206–213
- Taylor, C. W., & Kirby, A. M. (2015). Cardiac Side-effects From Breast Cancer Radiotherapy. *Clinical Oncology*, 27(11), 621–629
- Timmerman, R., & Xing, L. (2010). *Image-guided and adaptive radiation therapy*. Lippincott Williams & Wilkins - Wolters Kluwer health.
- Trnková, P., Knäusl, B., Actis, O., Bert, C., Biegun, A. K., Boehlen, T. T., Furtado, H., McClelland, J., Mori, S., Rinaldi, I., Rucinski, A., & Knopf, A. C. (2018). Clinical implementations of 4D pencil beam scanned particle therapy: Report on the 4D treatment planning workshop 2016 and 2017. *Physica Medica*, 54, 121–130
- Trofimov, A., & Bortfeld, T. (2003). Optimization of Beam Parameters and Treatment Planning for Intensity Modulated Proton Therapy. *Technology in Cancer Research & Treatment*, 2(5), 437–444
- van den Bogaard, V. A. B., Spoor, D. S., van der Schaaf, A., van Dijk, L. V., Schuit, E., Sijtsema, N. M., Langendijk, J. A., Maduro, J. H., & Crijs, A. P. G. (2021). The Importance of Radiation Dose to the Atherosclerotic Plaque in the Left Anterior Descending Coronary Artery for Radiation-Induced Cardiac Toxicity of Breast Cancer Patients? *International Journal of Radiation Oncology\*Biography\*Physics*, 110(5), 1350–1359
- van Herk, M., Remeijer, P., Rasch, C., & Lebesque, J. V. (2000). The probability of correct target dosage: Dose-population histograms for deriving treatment margins in radiotherapy. *International Journal of Radiation Oncology\*Biography\*Physics*, 47(4), 1121–1135
- Varian Medical Systems (2013). Eclipse Proton Algorithm Reference Guide 1-177
- VisionRT Product Guide (2015). Materials provided by VisionRT company (VisionRT Ltd, London, United Kingdom)
- Widder, J., van der Schaaf, A., Lambin, P., Marijnen, C. A. M., Pignol, J.-P., Rasch, C. R., Slotman, B. J., Verheij, M., & Langendijk, J. A. (2016). The Quest for Evidence for Proton Therapy: Model-Based Approach and Precision Medicine. *International Journal of Radiation Oncology\*Biography\*Physics*, 95(1), 30–36
- Wilson, R. R. (1946). Radiological Use of Fast Protons. *Radiology*, 47(5), 487–491
- Wolthaus, J. W. H., Schneider, C., Sonke, J.-J., van Herk, M., Belderbos, J. S. A., Rossi, M. M. G., Lebesque, J. V., & Damen, E. M. F. (2006). Mid-ventilation CT scan construction from

- four-dimensional respiration-correlated CT scans for radiotherapy planning of lung cancer patients. *International Journal of Radiation Oncology\*Biophysics*, 65(5), 1560–1571
- Woodard, H. Q., & White, D. R. (1986). The composition of body tissues. *The British Journal of Radiology*, 59(708), 1209–1218
- World Health Organization. (2020). *WHO report on cancer: Setting priorities, investing wisely and providing care for all*. World Health Organization
- Zenklusen, S. M., Pedroni, E., & Meer, D. (2010). A study on repainting strategies for treating moderately moving targets with proton pencil beam scanning at the new Gantry 2 at PSI. *Physics in Medicine and Biology*, 55(17), 5103–5121
- Zhang, Q., Liu, J., Ao, N., Yu, H., Peng, Y., Ou, L., & Zhang, S. (2020). Secondary cancer risk after radiation therapy for breast cancer with different radiotherapy techniques. *Scientific Reports*, 10(1), 1220
- Zhang, Y., Huth, I., Wegner, M., Weber, D. C., & Lomax, A. J. (2016). An evaluation of rescanning technique for liver tumour treatments using a commercial PBS proton therapy system. *Radiotherapy and Oncology*, 121(2), 281–287

In total, 140 reference items.

## List of Tables

Table 1 The summary of used tissue equivalent plugs and water-fillable vial for the CT calibration curve, their physical densities and measured both, HU and std values .....	59
Table 2 Imaging protocol details used for data collection .....	66
Table 3 Dosimetric comparison of heart and left lung doses obtained in photon and proton plans w/ the DIBH technique; $D_{\text{mean}}$ - mean dose, $V_{20}$ - volume receiving 20 Gy or Gy(RBE) for photons and protons, respectively.....	72
Table 4 Dosimetric comparison of LAD doses obtained in photon and proton plans w/ the DIBH technique; $D_{\text{mean}}$ - mean dose, $D_{\text{max}}$ - maximum dose, $D_{0.2\text{cm}^3}$ - dose received by the 0.2 cm <sup>3</sup> volume of the LAD, $V_{45}$ - volume receiving 45 Gy or Gy(RBE) for photons or protons, respectively .....	73
Table 5 Review of treatment planning approaches; NA- not applicable, WB - whole breast, CW - chest wall, PMC - post mastectomy, LPC - lumpectomy, LM - lymph nodes, IMN - internal mammary nodes, FB - free breathing, BH - breath hold, DIBH - deep inspiration BH, BHI - BH at inhalation, BHE - BH at exhalation, SFUD - single field uniform dose, IMPT - intensity modulated proton therapy, RBE - relative biological effectiveness .....	79
Table 6 Chosen beam arrangements in Study III .....	81
Table 7 Dosimetric results (mean±one standard deviation) for CTV coverage ( $V_{98\%}$ , $V_{95\%}$ ), homogeneity index (HI) and integral body dose with regard to selected beam arrangement .....	84
Table 8 Dosimetric results (mean±one standard deviation) for left lung, heart and LAD, with regard to selected beam arrangement; $D_{\text{mean}}$ - mean dose, $D_{0.2\text{cm}^3}$ - dose received by the 0.2 cm <sup>3</sup> volume of the LAD, $D_{\text{max}}$ - maximum dose, $V_{20}/V_{10}/V_5$ - volumes receiving 20/10/5 Gy(RBE), respectively and $D_{10\%}/D_{5\%}$ - doses received by 10%/5% of the volume, respectively .....	88
Table 9 Dosimetric results (mean±one standard deviation) for CTV with regard to selected beam arrangement; $D_{98\%}$ - dose received by 98% of the CTV volume .....	89
Table 10 Dosimetric results (mean±one standard deviation) for CTV with regard to selected beam arrangement; $D_{5\%}/D_{2\%}$ - dose received by 5%/2% of the CTV volume .....	90
Table 11 Dosimetric results (mean±one standard deviation) for left lung, heart and LAD, with regard to selected beam arrangement; $D_{10\%}/D_{5\%}$ - doses received by 10%/5% of the volume, respectively .....	92
Table 12 CIRS materials properties reproduced from CIRS Dynamic Motion Thorax Brochure (CIRS Dynamic Motion Thorax Brochure) .....	94
Table 13 Imaging protocol details used for 4DCT data collection .....	98
Table 14 Dosimetric results for the ITV-optimized plans (including nominal and perturbed scenarios) for various motion amplitudes and different optimization algorithms w/ the robust 3D optimization .....	101
Table 15 Details of <i>pld</i> plans prepared for the measurements of single spots .....	107
Table 16 Details of <i>pld</i> plans prepared for the measurements of 15x15 cm <sup>2</sup> homogeneous fields .....	107
Table 17 The results of measured spot sizes ( $\sigma_x$ , $\sigma_y$ ) and symmetry ( $S$ ) for proton beams of 70, 150 and 225 MeV energy (meas) with the reference (ref); $x_{\text{diff}}$ and $y_{\text{diff}}$ are the percentage differences of spot sizes in $x$ and $y$ directions .....	111
Table 18 The results of measured spot sizes ( $\sigma_x$ , $\sigma_y$ ) and symmetry ( $S$ ) for proton beams of 70, 150 and 225 MeV energy and various delivery modes including <i>no repainting</i> or $2x/3x$ rescanning; $x_{\text{diff}}$ and $y_{\text{diff}}$ are the percentage differences of spot sizes with regard to the <i>no repainting</i> delivery mode .....	111

Table 19 The results of measured field size ( $x$ , $y$ ), flatness ( $F$ ) and symmetry ( $S_x$ , $S_y$ ) for proton beams of 70, 150 and 225 MeV energy and various delivery modes including <i>no repainting</i> or $2x/3x$ rescanning; $x_{diff}$ and $y_{diff}$ , $F_{diff}$ , $S_{x-diff}$ and $S_{y-diff}$ are the percentage differences of field sizes, flatness and symmetry with regard to the <i>no repainting</i> delivery mode, respectively .....	113
Table 20 The results of measured left/right (L/R) penumbra in $x$ ( $x_{PL}$ , $x_{PR}$ ) and $y$ ( $y_{PL}$ , $y_{PR}$ ) directions for proton beams of 70, 150 and 225 MeV energy and various delivery modes including <i>no repainting</i> or $2x/3x$ rescanning; $x_{PL/PR-diff}$ and $y_{PL/PR-diff}$ are the percentage differences in penumbra with regard to the <i>no repainting</i> mode delivery .....	114
Table 21 The GI(3%/2mm) results for isocenter and +1mm plane for ITV1_P and ITV1_N plans, optimized with the PCS and NUPO algorithm, respectively and (1) motion scenario .....	120
Table 22 The GI(3%/2mm) results for isocenter and -1mm plane for ITV2_P and ITV2_N plans, optimized with the PCS and NUPO algorithm, respectively and (2) motion scenario .....	124

## List of Figures

Figure 1 IBA C-230 cyclotron at CCB (IFJ PAN) in Krakow, Poland ( <a href="https://ccb.ifj.edu.pl/pl.cyklotron_proteus_c_235.html">https://ccb.ifj.edu.pl/pl.cyklotron_proteus_c_235.html</a> ) .....	15
Figure 2 Schematic outline of the CCB IFJ PAN facility: the IBA Proteus 235 therapy system consisting of a cyclotron with highlighted energy selection system and beam line shared by four rooms: experimental hall, eye treatment room and two gantry rooms with dedicated pencil beam scanning nozzles (reproduced from Kłodowska, 2018) .....	16
Figure 3 The principle of PBS technique: two scanning magnets located in the nozzle ( $X_g$ - horizontal and $Y_g$ - vertical) deflect the narrow proton pencil beam to irradiate the predefined spot positions over the 3D tumor volume (reproduced from Mojżeszek, 2018) .....	17
Figure 4 A schematic drawing of a scanning technique: pencil beam is scanned across the 3D target volume, i.e. layer by layer and spot by spot, starting from the 2D X-Y plane of highest energy. Different spots, represented as black circles, depicts various spots intensity (a principle of intensity modulated proton therapy, IMPT) (Trofimov & Bortfeld, 2003) .....	18
Figure 5 The Patient Positioning and Verification System (PPVS) at CCB IFJ PAN includes two orthogonal X-ray tubes (one located in the nozzle and one located in the rolling floor) and two flat panels (retracted at the image) to record the X-ray image .....	19
Figure 6 VisionRT system 3D cameras mounted in the gantry treatment room at CCB IFJ PAN ( <a href="https://ccb.ifj.edu.pl/pl.dwa_nowoczesne_stanowiska_gantry.html">https://ccb.ifj.edu.pl/pl.dwa_nowoczesne_stanowiska_gantry.html</a> ) .....	20
Figure 7 AlignRT software: an example of real time deltas (RTDs) calculation (reproduced from AlignRT User Guide, 2015) .....	21
Figure 8 Comparison of photon (top) and proton (bottom) dose distributions in two patients with liver cancer: a) 3D-CRT, b) VMAT, c) and d) intensity modulated proton therapy (IMPT) (Mondlane et al., 2017) .....	30
Figure 9 Predominant interactions of photons with matter as a function of the atomic number and photon energy (Podgorsak, 2005) .....	31
Figure 10 Percentage depth dose distributions for photon beams of energies ranging from 4 to 25 MV (solid lines) and Co-60 $\gamma$ rays (dotted line) (Podgorsak, 2005) .....	32
Figure 11 Percentage depth dose distribution for a proton beam of 140 MeV energy (dotted - single proton beam, full curve - qualitative estimation of a monoenergetic beam of that energy) (Wilson, 1946).....	34
Figure 12 The proton mass stopping power $S/\rho$ and the corresponding $R_{CSDA}$ range as a function of energy in water (Newhauser & Zhang, 2015).....	35
Figure 13 Multiple Coulomb Scattering through a thin slab material. $\theta_0$ - characteristic angle, a width of the angular spread, $x_0$ - displacement, L - distance to the scattering material (Paganetti, 2018) .....	36
Figure 14 Beam width broadening in water due to the Multiple Coulomb Scattering as a function of proton range (Pedroni et al., 2005) .....	38
Figure 15 The motion aspect as a function of time: a) the density changes in the head & case occurring during the whole course of treatment, b) the interfractional changes in the femoral heads position in the prostate case, c) the intrafractional changes in the lung tumor position (Paganetti, 2012) .....	40
Figure 16 An example of Dutch model-based for head and neck cases. Based on the photon and proton plans comparison, the dosimetric differences result in the delta NTCP, which plays the key role in the further patient assignment to the selected type of treatment (Tambas et al., 2020) .....	41

Figure 17 Presentation of an interplay effect for a lung cancer case: a) reference (nominal) plan and b) perturbed dose distribution (reproduced from Engwall et al., 2018) .....	43
Figure 18 The idea of layer repainting: each layer is delivered several times (here: three) to smooth out the deterioration of dose distribution resulting from the interplay effect (Mori et al., 2018) .....	44
Figure 19 The 4DCT of a breathing phantom 4D XCAT with inserted lung tumor, reconstructed to ten breathing phases and presenting the changes in tumor position over the whole breathing cycle (Cai et al., 2014) .....	46
Figure 20 The idea and evolution of the target definitions according to the a) ICRU 29, b) ICRU 50 and c) ICRU 50 reports (ICRU 29, 1978; ICRU 50, 1993; ICRU 62, 1999); reproduced from (Purdy, 2004).....	48
Figure 21 The principle of 4DRO including the beam delivery and motion aspect in the optimization process (Knopf, Czerska et al., 2022) .....	50
Figure 22 The difference between free and breath hold anatomy presenting the increased gap between target and cardiac structures; blue arrow marks the distance in FB anatomy and red in BH .....	53
Figure 23 The CIRS Electron Density Phantom Model 062M (CIRS Electron Density Phantom: Data Sheet) .....	58
Figure 24 The CT image of the CIRS Electron Density Phantom Model 062M with 16 tissue equivalent plugs and water-fillable vial; annotations: 1 & 12 - Solid Dense Bone (800 mg/cc HA), 2 & 14 - Lung (Inhale), 3 & 16 - Breast (50% Gland / 50% Adipose), 4 & 9 - Liver, 5 & 15 - Solid Trabecular Bone (200 mg/cc HA), 6 & 10 - Lung (Exhale), 7 & 11 - Adipose, 8 & 13 - Muscle, 17 - water .....	61
Figure 25 The new CT calibration curve implemented into the TPS for reference facility .....	62
Figure 26 The comparison of the CT calibration curves for the reference facility and CCB IFJ PAN .....	63
Figure 27 The comparison of free (FB) and breath hold (BH) anatomies with measured mean distance indicating the increased gap between heart and target due to breath intake .....	67
Figure 28 Comparison of 50% (top) and 95% (bottom) isodoses of the prescribed dose for a breath hold photon plan (a and b) and proton free breathing plan (c and d) .....	70
Figure 29 The dosimetric difference between photon and proton plan; the most significant increase in radiation burden due to the higher dose deposition of a photon plans is seen in the left lung area .....	76
Figure 30 Visualization of chosen beam arrangements for the study purposes .....	80
Figure 31 Dose distributions (10% isodose of the prescribed dose) for all beam arrangements used in the study; abbreviations: 1B (an en face beam), 3B (three oblique beams: 20°, 60° and 340°), 2AP (0° and en face beam), 2PP (two oblique beams), 2LAT (an en face beam and 90°) .....	85
Figure 32 The CIRS Dynamic Thorax Motion Phantom (a) and the CIRS Dynamic Platform (b) (CIRS Dynamic Thorax Phantom: Brochure, CIRS Dynamic Platform: Brochure) .....	93
Figure 33 The cut away view of the CIRS Dynamic Thorax Motion Phantom depicting the soft tissue target inside the phantom (CIRS Dynamic Thorax Motion Phantom Brochure) .....	94
Figure 34 The breathing phantom setup prepared for time-resolved imaging .....	95
Figure 35 The breathing phantom with inserted imaging rod .....	96
Figure 36 Cut view and internal structure of the imaging rod (CIRS Dynamic Thorax Motion Phantom Brochure) .....	96
Figure 37 The CIRS Motion Control Software presenting the details for the third motion scenario including S-I, A-P and LAT target movement directions .....	98

Figure 38 An example of tumor displacement due to breathing (0% and 50% of the breathing cycle blended).....	99
Figure 39 Comparison of dose distributions (95% isodose of the prescribed dose) for (A) PCS and (B) NUPO algorithms and second motion scenario (S-I, 5.0 mm amplitude); red contour represents the CTV structure.....	102
Figure 40 Comparison of dose distributions (95% isodose of the prescribed dose) for (A) PCS and (B) NUPO algorithms and second motion scenario (S-I, 10.0 mm amplitude); red contour represents the CTV structure.....	102
Figure 41 The dose-volume histograms for the CTV structure and plans optimized with PCS (A) and NUPO (B) algorithms for motion scenario (1) and with included plan uncertainty scenarios.....	103
Figure 42 Lynx® PT detector (IBA Dosimetry, Germany) .....	106
Figure 43 Standard coordinate systems used at the gantry room, i.e. FRS and GCS .....	108
Figure 44 The comparison of single spots distribution of 70 MeV energy for (a) no repainting and (b) 2x repainting delivery mode; the chart presents comparison of profiles going through the center of spots in y direction.....	112
Figure 45 The comparison of single spots distribution of 150 MeV energy for (a) no repainting and (b) 2x repainting delivery mode; the chart presents comparison of profiles going through the center of spots in y direction.....	112
Figure 46 The comparison of single spots distribution of 225 MeV energy for (a) no repainting and (b) 2x repainting delivery mode; the chart presents comparison of profiles going through the center of spots in y direction.....	112
Figure 47 The comparison of homogeneous 15x15 cm <sup>2</sup> fields distribution of 70 MeV energy for (a) no repainting and (b) 2x repainting delivery mode; the chart presents comparison of profiles going through the center of fields in y direction .....	114
Figure 48 The comparison of homogeneous 15x15 cm <sup>2</sup> fields distribution of 150 MeV energy for (a) no repainting and (b) 2x repainting delivery mode; the chart presents comparison of profiles going through the center of fields in y direction.....	115
Figure 49 The comparison of homogeneous 15x15 cm <sup>2</sup> fields distribution of 225 MeV energy for (a) no repainting and (b) 2x repainting delivery mode; the chart presents comparison of profiles going through the center of fields in y direction .....	115
Figure 50 Setup prepared for measurements: CIRS Dynamic Platform, MatriXX detector and RW3 slab phantom positioned at the treatment couch and aligned with lasers .....	116
Figure 51 The PTW absolute dosimetry phantoms with chamber adaptation plates; the RW3 Slab Phantom is presented on the right (PTW Radiation Medicine QA Catalog, Germany) .....	116
Figure 52 The MatriXX detector (MatriXX PT User’s Guide, IBA Dosimetry, Germany) .....	118
Figure 53 Comparison of dose distributions, profiles and GI(3%/2mm) results for the isocenter plane of ITV1_P plan, Field 1 for different delivery modes: static (left), S-I (no repainting) (middle) and 2x repainting (right); red curves present the measurements, green curves present the planes exported from TPS (plan was recalculated in a water tank with an isocenter set to 4.14 cm, corresponding to 4.04 cm of RW3 slabs and MatriXX effective point of measurement) .....	122
Figure 54 Comparison of dose distributions, profiles and GI(3%/2mm) results for the isocenter plane of ITV1_N plan, Field 1 for different delivery modes: static (left), S-I (no repainting) (middle) and 2x	

repainting (right); red curves present the measurements, green curves present the planes exported from TPS (plan was recalculated in a water tank with an isocenter set to 4.14 cm, corresponding to 4.04 cm of RW3 slabs and MatriXX effective point of measurement) .....123

Figure 55 Comparison of dose distributions, profiles and GI(3%/2mm) results for the isocenter plane of ITV2\_P plan, Field 1 for different delivery modes: static (left), S-I (no repainting) (middle) and 2x repainting (right); red curves present the measurements, green curves present the planes exported from TPS (plan was recalculated in a water tank with an isocenter set to 4.14 cm, corresponding to 4.04 cm of RW3 slabs and MatriXX effective point of measurement) .....126

Figure 56 Comparison of dose distributions, profiles and GI(3%/2mm) results for the isocenter plane of ITV2\_N plan, Field 1 for different delivery modes: static (left), S-I (no repainting) (middle) and 2x repainting (right); red curves present the measurements, green curves present the planes exported from TPS (plan was recalculated in a water tank with an isocenter set to 4.14 cm, corresponding to 4.04 cm of RW3 slabs and MatriXX effective point of measurement) .....127